

Master's thesis

NTNU
Norwegian University of Science and Technology
Faculty of Natural Sciences
Department of Chemical Engineering

Albert Miró i Rovira

Synthesis and design strategies of CuCr-layered double hydroxides for improved photocatalytic nitrogen fixation under visible light

Master's thesis in Chemical Engineering

Supervisor: Magnus Rønning

Co-supervisor: Jibin Antony

July 2021



Norwegian University of
Science and Technology

Albert Miró i Rovira

Synthesis and design strategies of CuCr-layered double hydroxides for improved photocatalytic nitrogen fixation under visible light

Master's thesis in Chemical Engineering
Supervisor: Magnus Rønning
Co-supervisor: Jibin Antony
July 2021

Norwegian University of Science and Technology
Faculty of Natural Sciences
Department of Chemical Engineering



Norwegian University of
Science and Technology

Preface

This master thesis is the final work of my two-year Master's Degree in Chemical Engineering at the Norwegian University of Science and Technology (NTNU) and was written at the Catalysis Group (KINCAT) of the Department of Chemical Engineering.

This thesis is the continuation of my Specialization Project, done during the autumn semester of 2020. Therefore, some of the materials presented in this thesis were previously used in the specialization project. Moreover, the structure of this writing, mainly the Theory and Materials and Methods chapter, is inspired by the one presented in the before-mentioned project.

This project is dedicated to my family and friends. Without them, I would not be where I am today.

I want to thank Prof. Magnus Rønning, my supervisor, and Jibin Antony, my co-supervisor. For the time, effort, and patience they have put into me and, by consequence, this project. Their advice has been highly beneficial for me and has allowed me to better understand the worlds of photocatalysis and experimental research.

Finally, I also want to thank Estelle Marie M. Vanhaecke, Karin Wiggen Dragsten, Anne Hoff, Jens Norrman, Samuel K. Regli, Maria Tsoutsouva, and all Nanolab personnel for the training and assistance with the instrumentation, and Jithin Gopakumar, Kishore Rajendran, and Mario Ernesto Casalegno for their help during this project.

In accordance with the exam regulations of the Norwegian University of Science and Technology, I solemnly promise that the thesis I present in this document is an independent work.

15th of July of 2021. Trondheim, Norway

A handwritten signature in black ink, consisting of several loops and a long horizontal stroke at the bottom, positioned above a solid horizontal line.

Albert Miró i Rovira,

Abstract

Ammonia is one of the most important chemical commodities in the world. The synthesis of this substance currently relies on the Haber Bosch process, which is a very energy-intensive process. Due to its importance and magnitude, this chemical sector has a large carbon footprint and is a significant emitter of greenhouse gases, contributing to global warming. A sustainable alternative to conventional ammonia synthesis is therefore encouraged. One of the present-day studied alternatives is photocatalysis. Several materials are being investigated to make photocatalysis an economically viable option. One way to achieve this objective is to develop photocatalysts that only require visible light to function, with a bandgap energy less than 3,1 eV. In this project, CuCr layered double hydroxides (LDH) were studied as a possible photocatalyst for the nitrogen fixation to produce ammonia. The metal loading of Cu and Cr in the LDH was tuned to obtain different materials and test their photocatalytic performance to find the optimum ratio. The materials were synthesized through coprecipitation and hydrothermal synthesis.

Additionally, other lines of improvement of the photocatalysts were pursued. Firstly, etching was performed on these photocatalysts, and the effect on their morphology and performance was studied. Secondly, the addition of a third metal species, Co, Ni, and Fe, in the LDH structure was also analyzed. Both Co, Ni were successfully integrated while Fe was not. The successful ternary LDH were further characterized and tested to study their performance.

These materials were characterized by means of X-ray diffraction (XRD), scanning electron microscopy (SEM), energy-dispersive X-ray spectroscopy (EDX), diffuse reflectance spectroscopy (UV-Vis DRS), fluorescence spectroscopy, Fourier-transform infrared spectroscopy (FT-IR), and electron paramagnetic resonance spectroscopy (EPR) to outline their crystallinity, phase purity, morphology, elemental composition, bandgap energy, absorbance spectrum, photoluminescence, and bonding structure. Almost all investigated materials have bandgap energy less than 3,1 eV allowing these photocatalysts to work under visible light. Finally, the highest product yield obtained is 23,9 $\mu\text{mol NH}_4^+$ per gram of catalyst, compared to the original 13,0 $\mu\text{mol NH}_4^+$ per gram of catalyst, acquired in the previous specialization project.

Table of Contents

1	Introduction.....	15
1.1	Scope of the thesis	17
2	Theory.....	19
2.1	Background in NH ₃ synthesis.....	19
2.2	Band theory.....	19
2.3	Photocatalysis	21
2.3.1	Photocatalysis for ammonia synthesis	22
2.4	Layered Double Hydroxide	23
2.4.1	Ternary Layered Double Hydroxides	24
2.4.2	Copper-chromium layered double hydroxide.....	25
2.5	Catalyst preparation.....	25
2.5.1	Coprecipitation.....	26
2.5.2	Hydrothermal synthesis	26
2.5.3	Defect engineering.....	27
2.6	Characterization.....	27
2.6.1	X-ray diffraction	27
2.6.2	Scanning electron microscopy	28
2.6.3	Energy-dispersive X-ray spectroscopy	29
2.6.4	Ultraviolet-visible spectrophotometry	30
2.6.5	Ultraviolet-visible diffuse reflectance spectroscopy.....	31
2.6.6	Fluorescence spectroscopy	31
2.6.7	Fourier-transform infrared spectroscopy	33
2.6.8	Electron paramagnetic resonance spectroscopy	34
3	Materials and methods	37
3.1	Chemicals	37
3.2	Preparation of CuCr-LDH	37
3.2.1	Dropwise addition.....	37
3.2.2	Instant addition	39
3.2.3	Ternary LDH synthesis.....	39

3.2.4	Alkali etching.....	39
3.2.5	Nomenclature and classification.....	40
3.3	Characterization.....	42
3.3.1	XRD.....	42
3.3.2	SEM and EDX.....	42
3.3.3	UV-Vis DRS.....	43
3.3.4	Fluorescence spectroscopy.....	44
3.3.5	FT-IR spectroscopy.....	44
3.3.6	EPR spectroscopy.....	44
3.4	Photocatalytic set-up.....	45
3.5	Photocatalytic reaction experiment.....	46
3.6	Photocatalytic activity measurement.....	47
4	Results and discussion.....	49
4.1	Characterization of the CuCr-LDH species.....	49
4.1.1	Crystallinity and phase purity.....	49
4.1.2	Absorbance and bandgap energy.....	54
4.1.3	Morphology.....	57
4.1.4	Element detection.....	60
4.1.5	FT-IR of ternary LDH.....	61
4.1.6	Photoluminescence of ternary LDH.....	63
4.1.7	Determination of V_O proliferation in etched LDH.....	64
4.2	Photocatalytic results.....	65
4.3	Challenges.....	69
5	Conclusions.....	73
6	Further work.....	75
	Appendix A – Tauc plots.....	83
	Appendix B - EDX mapping.....	85
	Appendix C – Pictures of samples.....	87
	Appendix D – Risk Assessment.....	89

List of figures

Figure 1.1 Annual ammonia production worldwide	15
Figure 1.2 Scheme of nitrogenase ammonia synthesis mechanism [6]	16
Figure 2.1 Scheme of the mechanism of photocatalytic ammonia synthesis [8]	22
Figure 2.2 Bandgap energy of a series of semiconductors compared to water and nitrogen reduction/oxidation potentials [9]	23
Figure 2.3 Three dimensional scheme of the structure of a LDH [11]	24
Figure 2.4 Diagram of two lattice planes diffractin a beam [14]	28
Figure 2.5 Diagram of the principal of EDX	30
Figure 2.6 Scheme showing the difference between specular and diffuse reflection [17].....	31
Figure 2.7 Jablonski diagram	32
Figure 2.8 Diagram of a fluorometer	32
Figure 2.9 Diagram of a FT-IR instrument and interferometer.....	33
Figure 2.10 Splitting of electron spin states	34
Figure 3.1 Picture of the dropwise additon synthesis setup	38
Figure 3.2 Picture of the Avantes AvaLight-DH-S spectrophotometer	43
Figure 3.3 Scheme of integrating sphere (white sphere collector) of a DRS apparatus [17]...	44
Figure 3.4 Diagram of the photocatalytic set-up used for this project.....	46
Figure 4.1 XRD results for CuCr-LDH:1-D-40-a, CuCr-LDH:2-D-40-a, CuCr-LDH:3-D-40-a, and CuCr-LDH:5-D-40-a.	49
Figure 4.2 XRD results of CuCr-LDH:2-D-30-a and CuCrFe-LDH:2-D-30-a	51
Figure 4.3 XRD results of CuCr-LDH:2-D-30-b and CuCrFe-LDH:2-D-30-b.....	51
Figure 4.4 XRD patterns of CuCr-LDH:2-D-30-a, CoCuCr-LDH:2-D-30-a, and CuNiCr-LDH:2-D-30-a.....	53

Figure 4.5 Absorbance spectra of CuCr-LDH:1-D-40-a, CuCr-LDH:2-D-40-a, CuCr-LDH:2-I-40-a, CuCr-LDH:3-D-40-a, and CuCr-LDH:5-D-40-a	54
Figure 4.6 Absorbance spectra of CuCr-LDH:2-D-40-a, 0,5E- CuCr-LDH:2-D-40-a, 1,0E- CuCr-LDH:2-D-40-a, 2,0E- CuCr-LDH:2-D-40-a, and 3,0E-CuCr-LDH:2-D-40-a.....	55
Figure 4.7 Absorbance spectra of CuCr-LDH:2-D-30-a, CuCr-LDH:2-D-30-b, CuCrFe-LDH:2-D-30-a, CuCrFe-LDH:2-D-30-b, CoCuCr-LDH:2-D-30-a, and CuNiCr-LDH:2-D-30-a	55
Figure 4.8 a (left) and b (right) SEM images of CuCr-LDH:2-D-40-a.....	57
Figure 4.9 a (left) and b (right) SEM images of 0,5E-CuCr-LDH:2-D-40-a.....	58
Figure 4.10 a (left) and b (right) SEM images of 1,0E-CuCr-LDH:2-D-40-a.....	58
Figure 4.11 a (left) and b (right) SEM images of 2,0E-CuCr-LDH:2-D-40-a.....	58
Figure 4.12 SEM image of 3,0E-CuCr-LDH:2-D-40-a	59
Figure 4.13 a (left) and b (right) SEM images of CuCr-LDH:2-D-30-a.....	59
Figure 4.14 a (left) and b (right) SEM images of CoCuCr-LDH:2-D-30-a.....	60
Figure 4.15 FT-IR spectra of samples CuCr-LDH:2-D-30-a, CoCuCr-LDH:2-D-30-a, and CuNiCr-LDH:2-D-30-a.....	62
Figure 4.16 FT-IR baseline measurements with both the anvil open and closed.....	62
Figure 4.17 Fluorescence spectra of CuCr-LDH:2-D-30-a, CoCuCr-LDH:2-D-30-a, and CuNiCr-LDH:2-D-30-a.....	64
Figure 4.18 Photocatalytic activity results of the CuCr-LDH catalysts with different metal ratio	66
Figure 4.19 Photocatalytic activity results of the etched CuCr-LDH catalysts	67
Figure 4.20 Photocatalytic activity results of the ternary CuCr-LDH catalysts.....	69
Figure 4.21 Photocatalytic activity results of CuCr-LDH:2-D-30-a under normal experimental conditions, with no light (n.l.), with Ar, and with Ar and no light	70

List of tables

Table 3.1 All synthesized materials names and characteristic properties	41
Table 4.1 CuCr-LDH samples with their $\text{Cu}^{2+}/\text{Cr}^{3+}$ ratio and x value	50
Table 4.2 Bandgap energy of all CuCr-LDH species.....	56
Table 4.3 Elemental composition obtained by EDX of several LDH samples	60
Table 4.4 Obtained mass of catalyst after etching treatment	68

Abbreviations

2D / 3D	= two dimensional / three dimensional.
a.u.	= arbitrary units.
BSE	= back-scattered electrons.
CB	= conduction band.
DI	= deionized.
DRS	= diffuse reflectance spectroscopy.
EDX	= Energy-dispersive X-ray spectroscopy.
EPR	= electron paramagnetic resonance spectroscopy.
FT-IR	= Fourier-transform infrared spectroscopy.
GHG	= greenhouse gases.
IR	= infrared.
LDH	= layered double hydroxide.
M	= metal cation.
MFC	= mass flow controller.
MMCT	= metal-to-metal charge-transfer.
NHE	= normal hydrogen electrode.
O	= oxygen atom.
SE	= secondary electrons.
SEM	= scanning electron microscopy.
USA	= Unites States of America.
UV-Vis	= ultraviolet-visible spectroscopy.
VB	= valence band.
V _o	= oxygen vacancy.
XRD	= X-ray diffraction.

1 Introduction

The human population has grown every time a tremendous technological advancement has been achieved. During the 19th and 20th centuries, the industrial revolution and the associated technological advances have resulted in a steady increase in the world population. After the 1950s, the population growth has kept rising even further [1]. To sustain this continuous growth, it has been required that critical sectors, like agriculture, match this expansion. During the industrial revolution, the implementation of mineral fertilizers in agriculture allowed for increased food production. Still, these substances were scarce and only produced by few countries, mainly Chile [2]. It was not until the beginning of the 20th century, with the industrial development of artificial fertilizers, that agriculture allowed a much faster population growth [3]. However, from that moment onwards, modern agriculture has heavily relied on synthetic fertilizers [3].

Most of these fertilizers used today are nitrogen-based [3]. This type of material requires ammonia as a primary source to be manufactured. Therefore, ammonia is one of the most fundamental chemical commodities. Furthermore, ammonia is the second most-produced chemical product worldwide, and the fertilizer industry uses 85% of the world's ammonia [4]. Figure 1.1 depicts the evolution of ammonia production in the past years.

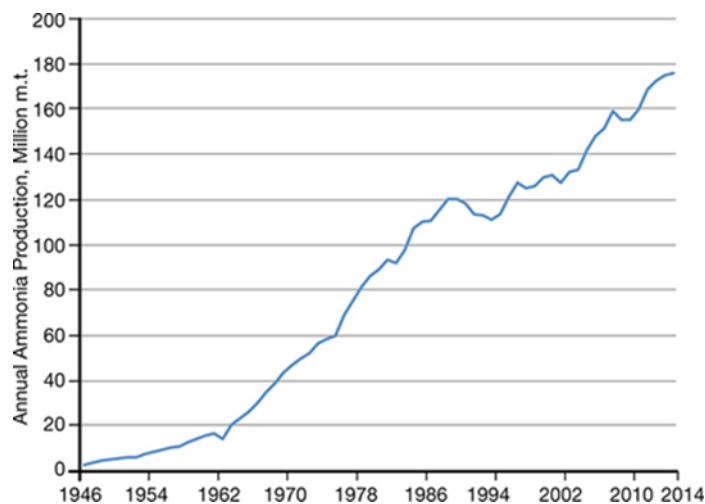


Figure 1.1 Annual ammonia production worldwide from 1946 to 2014 [5]

Ammonia synthesis is achieved by means of the Haber-Bosch process. This process was developed and implemented at the beginning of the 20th century. It requires nitrogen, which is obtained from air, and hydrogen, obtained from fossil resources (mainly natural gas or coal) to

react over a catalyst. The process requires high temperature and pressure to synthesize ammonia, making the Haber-Bosch process very energy-intensive.

Since ammonia is the second most-produced chemical commodity worldwide [3], it makes the Haber-Bosch process, due to its high fossil dependence, one of the most significant contributors to global greenhouse gas (GHG) emissions. GHG emissions must be reduced to palliate global warming in the current climate situation, so more sustainable alternatives for the Haber-Bosch process need to be developed to produce ammonia.

The main issue in finding an alternative, more sustainable process for ammonia synthesis is that nitrogen, an essential precursor to ammonia, is a highly stable molecule, requiring great energy input for its reduction. Nonetheless, some living microorganisms, like cyanobacteria (present in vegetal organisms), can convert atmospheric nitrogen to ammonia, at ambient conditions, in the presence of nitrogenase, an enzyme [6]. To harness energy to power this chemical process, they require nitrogenase, an enzyme. This enzyme functions as a catalyst for the synthesis of ammonia and is constituted of two main proteins. The first one, the Fe-based protein, obtains electrons from a reducing agent to power the reaction. The second one, the MoFe-based protein, is responsible for reducing N_2 to NH_3 , as seen in Figure 1.2 [7].

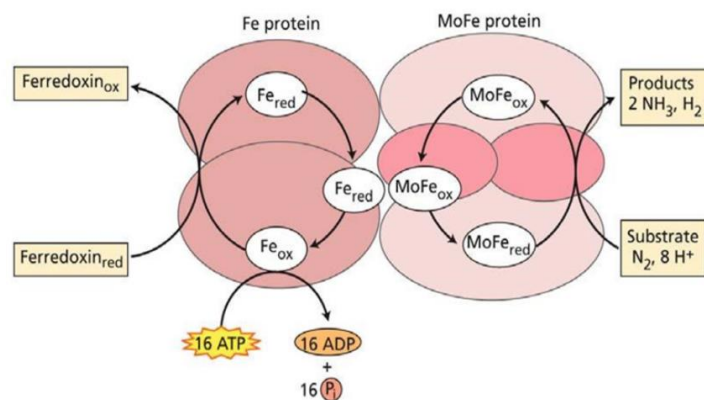


Figure 1.2 Scheme of nitrogenase ammonia synthesis mechanism [7]

From this low-energy system, alternative processes to Haber-Bosch have been conceptualized. In particular, the photocatalytic synthesis of ammonia is of interest in this case. A photocatalyst uses photons to generate photoexcited electrons transferred to N_2 molecules to reduce them to NH_3 . If this reaction occurs in a water medium, the photocatalyst can oxidize water molecules and produce the ammonia molecules' protons (H^+) required. However, photocatalytic nitrogen fixation is still in its infancy with low product yields. Hence, further research is necessary to make this a more appealing alternative and close to commercialization.

1.1 Scope of the thesis

This thesis aims to study copper-chromium layered double hydroxide (CuCr-LDH) as a photocatalyst candidate for nitrogen fixation under visible light for ammonia synthesis. The scope of this work is to synthesize, characterize and test the performance of this material in a reaction set-up at the Department of Chemical Engineering at NTNU. Furthermore, different post-synthesis techniques to improve catalyst performance will be studied, implemented, and tested on the material to enhance the conversion of the reaction. These methods are: tuning of the metal ratio on the LDH structures, etching of the LDH materials using an alkali agent, and adding a third metallic species (Co, Ni, and Fe) to the CuCr-LDH.

2 Theory

In this section of the thesis, some concepts will be introduced to grant the reader the necessary knowledge to comprehend the mechanics behind the reaction of interest, the catalyst structure, and the synthesis and characterization methods utilized.

2.1 Background in NH₃ synthesis

As previously introduced, ammonia is the second most-produced chemical commodity globally [2], and the primary way to obtain it is through the Haber-Bosch process. This process was developed by German scientists Fritz Haber and Carl Bosch in 1913 [3]. It consists of the reaction between nitrogen and hydrogen gas over an iron-based catalyst under an environment of high temperature and pressure, with temperatures around 450 to 500 °C and pressures of 200 to 250 bars.

If the thermodynamics of this reaction (shown in Equation 2.1) are considered, it can be observed that an environment of low temperature favors this reaction due to its exothermic nature (the enthalpy of the reaction is negative). Moreover, the reaction is also favored by high pressure because it is a gas-phase reaction, and therefore the high pressure tends to favor the side with the least amount of gas molecules, in this case, the product side.



Another issue with this reaction that can be overlooked by only observing the overall reaction is the dissociation of N₂ molecules, which is the rate-determining step of the process [8]. As stated in the previous chapter, a significant amount of energy is required to dissociate the nitrogen molecule because its high dissociation energy of 940 kJ·mol⁻¹ [8] contributes to its high stability. The most efficient way to introduce energy into the process is to increase the temperature of the operation. However, high temperatures will reduce the yield of ammonia. For this reason, a catalyst was introduced to allow for sufficient product yield under milder conditions.

2.2 Band theory

The band theory, also referred to as band theory of solids or zone theory of solids, is a theory that classifies materials depending on their electronic structure. It establishes that the energy of the electrons in solids can only be within a specific value range [9]. These ranges are named bands, energy ranges outside these bands are called forbidden bands. The acceptable ranges match the energy levels of an atom when it is in an isolated system.

When different particles surround each other to form a solid, these levels are modified due to the influence of quantum mechanical effects [9]. The electrons of an atom fill a particular band of levels, named the valence band (VB). The remaining levels that then stay empty are called the conduction band (CB). In an isolated atom, electrons can move freely from one energy level onto another empty level. In a solid, one electron can move from an energy level in a given band to another, inside the same band (VB) or in a different one (CB). The CB, though, can require the electron to cross through a group of forbidden energy levels.

Depending on how the VB and CB are positioned relative to each other, solids can be divided into three groups: conductors, semiconductors, and insulators [10]. Conductors are materials with no forbidden gap between the CB and VB, and their energy levels overlap so that electrons can move freely between them. On the other hand, insulators are materials where the energetic gap (bandgap) between the CB and VB is too high, so electrons cannot pass. Finally, semiconductors are materials where the energy difference between CB and VB can be overcome if the electron is excited. For example, an electron can transfer through if irradiated with a photon with an equal or greater bandgap energy (E_g) [9].

When an electron reaches the CB in a semiconductor, it leaves an empty energy level in the VB, commonly named hole. This hole generates a net positive charge in the valence band. Meanwhile, the conduction band has a net negative charge because of the additional electron; this phenomenon is named an electron-hole pair [9]. When an excited electron regresses to a more stable state, it will go from the CB to the VB, refilling the hole; this process is called recombination and effectively vanishes the electron-hole pair and, therefore, the available free carriers since there is no longer either a negative or positive charge in any of the bands [9].

Additionally, in the band theory, the Fermi level (E_f) is also described. The Fermi level is defined as a hypothetical energy level that, at thermodynamic equilibrium, has a 50% chance of being occupied by an electron at any given moment [11]. However, this level does not physically exist, as it lies energetically between the valence and conduction bands.

There are two main classes of bandgaps: direct and indirect [12]. In the case of a direct bandgap, both electron states of the VB and CB have the same momentum, which means that only the energy of a photon is required to transfer an electron across. On the other hand, in the case of an indirect bandgap, the momentum of the electron states in the VB and the CB is different; therefore, both a photon and a phonon are required to transfer an electron [12].

2.3 Photocatalysis

Photocatalysis has gained momentum over the last years as a great alternative to conventional catalysis for specific applications. The main application has been in the oxidation processes of organic solvents and other harmful substances, like alkanes or N₂O, developed by several scientific groups over the past decades [13] [14, 15]. Also, in 1972, researchers Akira Fujishima and Kenichi Honda developed the electrochemical photolysis of water [14]. Much of the research lately has been focused on the photolysis of water for hydrogen production, but so far, there has not been any technology that has reached industrial application. The main reason behind it is that photocatalysis is not an energy-intensive process, which means that the product yield is much lower than already established conventional catalytic processes. On the other hand, it is an excellent process for eliminating contaminants since it does not require high energy inputs. Usually, pollutants are diluted and only present in ppm or ppb, so a high yield is unnecessary.

Photocatalysis is the phenomenon of absorption of photons by a semiconductor material that enables a chemical reaction [15]. The main difference between the role of a catalyst used in a photocatalytic process and that of a conventional catalytic process is that it only absorbs photons to transfer this energy onto reactants and does not modify the reaction's kinetic barrier [16]. Equation 2.2 allows estimating the amount of energy striking the photocatalyst when irradiated with photons,

$$E = \frac{h \cdot c}{\lambda} \quad (2.2)$$

where E is the available energy [eV], h is the Planck constant (4.136×10^{-15} eV·s), c is the speed of light (2.99×10^8 m·s⁻¹) and λ is the wavelength [nm] of the irradiated photon [12]. Equation 2.2 determines that the energy output will be dependent on the photon's wavelength. The primary two sources of photons used for exciting the electrons in a photocatalyst originate from the visible light spectra, with a range of 400 to 700 nm, and ultraviolet light spectra (UV), ranging from 10 to 400 nm. These wavelength ranges applied to Equation 2.2 allows for an estimate for the maximum bandgap energy that a photoexcited electron can cross by only using visible light photons. If the bandgap energy is higher than 3.0 eV, the photocatalyst will require UV light to facilitate a photocatalytic reaction. Furthermore, the bandgap energy is also an essential factor when it comes to the recombination of electron-hole pairs, which can effectively reduce the photocatalytic efficiency [17]. A lower bandgap would lead to faster recombination phenomena.

2.3.1 Photocatalysis for ammonia synthesis

For the photocatalytic synthesis of ammonia, it is necessary to oxidize water molecules (water-splitting), obtain protons (H^+) for nitrogen fixation to ammonia. So, the reaction can be divided into the reduction of nitrogen and oxidation of water. Both the oxidation and reduction are represented in equations 2.4 and 2.3 respectfully and equation 3.5 describes the overall reaction [18]:



The water-splitting reaction (Equation 2.3) occurs in the photoanode of the photocatalyst (the valence band). For the oxidation to happen, the VB must have a positive net charge higher than the redox potential of O_2/H_2O at 1.23 V versus normal hydrogen electrode (NHE) [18]. The nitrogen fixation (Equation 2.4), which takes place in the photocathode (the conduction band), must split nitrogen molecules (N_2) with the electrons that originate in the CB. The nitrogen atoms need to react with the available protons from the water-splitting to obtain ammonia in a second step. For this reaction to happen, the net charge of the CB must be more negative than the redox potential of 1.17 V versus NHE [19]. The mechanism for this reaction is shown in Figure 2.1.

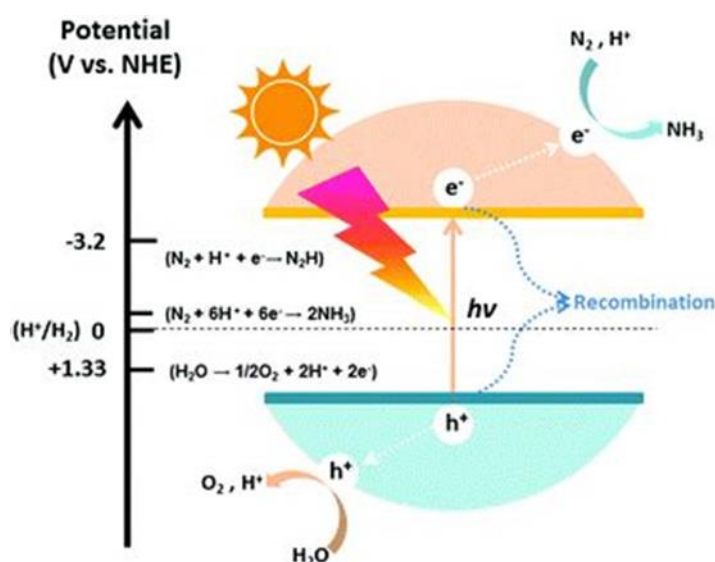


Figure 2.1 Scheme of the mechanism of photocatalytic ammonia synthesis [20]

As previously discussed, to produce ammonia through photocatalysis, both the oxidation and reduction potentials for the water splitting and the nitrogen fixation reaction must

be within the bandgap energy of the photocatalyst. Additionally, the bandgap energy must be less than 3.1 eV to power this process only with visible light. In Figure 2.2, the bandgap energies of several photocatalysts investigated to be used in this reaction are compared to the redox potentials for the photosynthesis of ammonia.

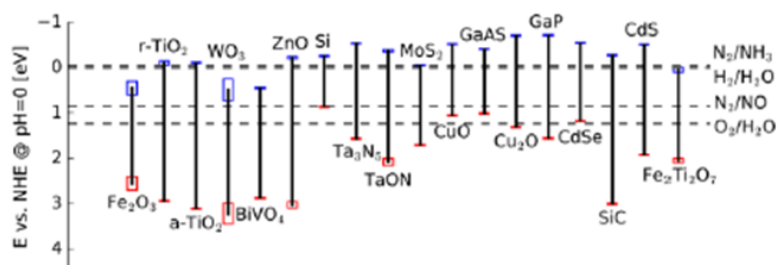
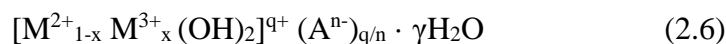


Figure 2.2 Bandgap energy of a series of semiconductors compared to water and nitrogen reduction/oxidation potentials [19]

2.4 Layered Double Hydroxide

Layered Double Hydroxides (LDH) are a type of ionic solids discovered approximately 150 years ago with the discovery of the mineral hydrotalcite. Manasse first described the structure of the hydrotalcite mineral in 1915, and the following chemical formula was proposed $[\text{Mg}_6\text{Al}_2(\text{OH})_{16}]\text{CO}_3 \cdot 4\text{H}_2\text{O}$. In the 1960s, Allmann and Taylor [21], utilizing X-ray diffraction, established a generic crystal structure for the hydrotalcite. The developed model was a generic layer sequence that described all LDHs, $[\text{A}c\text{B}Z\text{AcB}]_n$ where A and B are layers of hydroxide anions (OH^-), c are layers of metal cations, and Z are layers of other anions and water [22]. More accurate formulas have been developed since, as shown in Equation 2.6 [21]. In this case, the hydroxide layer was described as being composed of both divalent and trivalent metallic cations. Moreover, the layer of anions (A) was said to be formed by counterions (anions) and water to neutralize the net charge of the overall material and are only weakly bonded to the interlayers of metallic hydroxides. This phenomenon allows these anions to be exchangeable depending on the conditions in which this material is formed or synthesized [23].



The metallic hydroxide layers of these materials have a brucite-like structure [23], and through the presence of trivalent cations on these layers, there is a positive net charge. This occurrence makes it necessary to have the anion layers as part of these materials, as they help to neutralize the overall charge of the material [22].

In nature, the most usual anionic groups found in LDH structures are halogens (Cl^- , Br^-) or oxyanions (NO_3^- , CO_3^{2-} , SO_4^{2-}). For the metal cations the most common divalent actions

are: Ca^{2+} , Mg^{2+} , Mn^{2+} , Fe^{2+} , Co^{2+} , Ni^{2+} , Cu^{2+} or Zn^{2+} and for the trivalent cations: Al^{3+} , Fe^{3+} or Cr^{3+} [23]. A schematic of the layer sequence of an LDH can be seen in Figure 2.3.

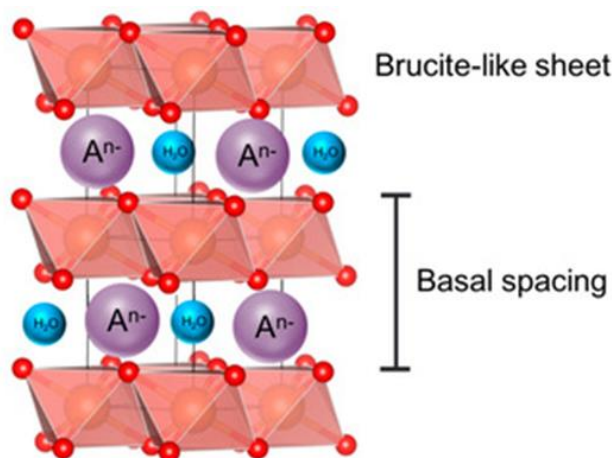


Figure 2.3 Three dimensional scheme of the structure of a LDH [24]

Since two different cations are in the hydroxide layer, it is necessary to achieve a certain stoichiometric ratio to allow the layered structure to be stable [24]. It is considered that to have a stable phase, x , which in Equation 2.6 represents the stoichiometric value of the trivalent cation, has to be between 0.2 and 0.33. However, in some LDH materials, this value can go up to 0.5 [24].

Layered double hydroxides have gained renown in recent years as an excellent material for photocatalysis in the visible-light range. LDH are semiconductors with fascinating properties. For example, LDH have a high concentration of surface defects, like oxygen vacancies, that expose unsaturated metal sites in the brucite-like layers [25]. Furthermore, according to a recent publication by Zhang et al. [25], oxobridged heterobinuclear units present in LDH have proven to contain metal-to-metal charge-transfer (MMCT) absorption bands. These bands act as deep visible-light absorbing chromophores for photocatalysis [25]. Thanks to LDH's easily controllable metal cation composition, it is possible to fine-tune some of its properties, like bandgap tuning and defect engineering, making them a very promising material for photocatalysis [25].

2.4.1 Ternary Layered Double Hydroxides

Ternary layered double hydroxides, as the name suggests, are a type of LDH material where a third metallic cation species is added to the structure. This cation still must have an oxidation state that will permit its incorporation. However, some cations with oxidation state

+4 have been successfully integrated into ternary LDH [26]. Its presence, though, has to maintain the stoichiometric ratio of cations still to have a stable LDH structure.

These materials have gained increasing prominence in the photo/electrochemical field, as they have very promising properties. The addition of a third cation has proven to allow greater tuning of electronic properties of the material, for example, lowering the bandgap energy, improving its conductivity, and photocatalytic properties [26]. Furthermore, these materials offer the possibility of wide tunability, which may contribute to better ion diffusion and a greater interlayer spacing [27].

2.4.2 Copper-chromium layered double hydroxide

Several layered double hydroxides with different metal cations have been investigated for the photocatalytic synthesis of ammonia, and some great results have been reported [7]. The main reason for these promising results is due to the presence of oxygen vacancies (V_o) in the LDH ultrathin layers. These V_o form gaps inside the LDH structure promote nitrogen gas adsorption and photoinduced charge transfer from the LDH to the adsorbed species [7].

From all the studied materials, the copper-chromium layered double hydroxide (CuCr-LDH) has been reported to be the most efficient for ammonia photosynthesis [7] because of the unique properties that this species acquires from the copper and chromium cations. It had been previously reported by Mock et al. [28] that complexes that incorporate molybdenum, tungsten, or chromium have shown activity for N_2 fixation. However, neither molybdenum nor tungsten can be incorporated into an LDH structure. Trivalent chromium cations (Cr^{3+}) show good light absorbance in the visible light range. Divalent copper cations (Cu^{2+}) in LDH materials have been reported to cause a strong Jahn-Teller effect compared to other divalent cations. This effect allows for more defects in the LDH structure through higher repulsion in the metallic hydroxide layer [25, 29].

2.5 Catalyst preparation

The catalyst preparation is comprised of the different techniques that are utilized to produce a catalyst. The various methods used can modify the essential properties of the final product. For preparing photocatalysts, the most utilized techniques are impregnation, coprecipitation, sol-gel, and hydrothermal synthesis.

2.5.1 Coprecipitation

Coprecipitation is a method that allows precipitating a solute, which is dissolved in a solution by adding another chemical called carrier. This carrier chemically reacts with the solute and forms a new insoluble substance in the solution forcing precipitation [30].

Like other chemical processes, modification of the parameters of this reaction can modify the result of the coprecipitation, for example, the equilibrium concentration of the substances in solution, the pH, the presence of ions that can interact both with the solute or the carrier, and the properties of the carrier, e.g., surface area, type of solid and surface charge [30].

For the formation of layered double hydroxides, coprecipitation allows the transfer of metal cations from ionic soluble salts to a precursor of the LDH that will precipitate and then can be recovered. The coprecipitation technique is often used because it allows higher metal loading onto the resulting material [30, 31].

2.5.2 Hydrothermal synthesis

Hydrothermal synthesis is a heterogeneous reaction that develops in the presence of water at specific conditions of temperature and pressure [32]. If instead of water, another solvent is utilized, this method is referred to as solvothermal synthesis. This technique aims for a precursor material to dissolve and recrystallize into a new substance under controlled conditions.

This method is typically used at relatively low temperatures, between 60 to 400 °C, and pressures from 1 to 200 bars. These conditions permit certain materials to solubilize at lower temperatures than usual where they can undergo this process. Otherwise, the necessary temperatures to carry these changes at atmospheric conditions would be futile as the material will be unstable.

The final product achieved with this method is of high purity and crystallinity. Also, this technic reduces the particle size distribution of the material [32]. The properties of the new species obtained through this process can be modified by adjusting critical parameters during the synthesis step, like temperature, pH, reaction time, and concentration of the precursors.

To procure the necessary conditions for the hydrothermal synthesis, the water solution with the precursor material is placed inside a sealed autoclave liner, which is placed into a furnace. When the temperature rises inside the autoclave, it will cause an increase in pressure.

This phenomenon will carry the solution to a supercritical fluid state. When these conditions are reached, the material's nucleation will be affected by supersaturation [33].

2.5.3 Defect engineering

Layered double hydroxides are materials with abundant surface defects like oxygen vacancies and coordinately unsaturated metal sites [34]. Despite this, a recurring issue with the use of these materials in photocatalysis is the difficulties in precisely controlling the presence and concertation of such defects. Therefore, defect engineering, a series of strategies and techniques, have been developed to assist during the synthesis or as a post-synthesis treatment for catalysts to adjust and tune their defects.

In recent years, defect engineering has been successfully implemented to enhance the photocatalytic activity of 2D-layered semiconductors, like LDH. Defect engineering allows for the tuning of surface defects in the crystalline structure of these materials. Defect engineering includes the introduction of vacancies of both cations and anions to create new active sites for the adsorption of the reactant species; inhibiting recombination process of electron-hole pairs by selective trapping of holes or photoexcited electrons; and modification of the VB and CB levels to alter the bandgap energy, and to lower the activation energy for surface redox reactions [34].

2.6 Characterization

Several techniques allow the determination and analysis of the structure and properties of a catalyst. Some of the methods that are used for this purpose are X-ray diffraction (XRD), Scanning electron microscopy (SEM), Ultraviolet-visible spectrophotometry (UV-Vis), Diffuse reflectance spectroscopy (DRS), and fluorescence spectrophotometry.

2.6.1 X-ray diffraction

X-ray diffraction (XRD) is a characterization technique used to analyze a solid material's crystalline structure. XRD uses a monochromatic X-ray beam that is pointed towards the sample. The instrument then collects the returning beam and examines how it has been altered by interacting with the sample. If two atoms are in the same crystal lattice, the diffracted X-ray in phase with this lattice will create a constructive interference, intensifying the returning beam [8]. This interference then can be transformed into the physical properties of the crystalline structure through Bragg's equation (Equation 2.8).

$$n \cdot \lambda = 2d \cdot \sin(\theta) \quad (2.8)$$

where λ is the X-ray wavelength, d the distance between lattice planes, and θ the angle between the normal and the diffracting plane, as shown in Figure 2.4.

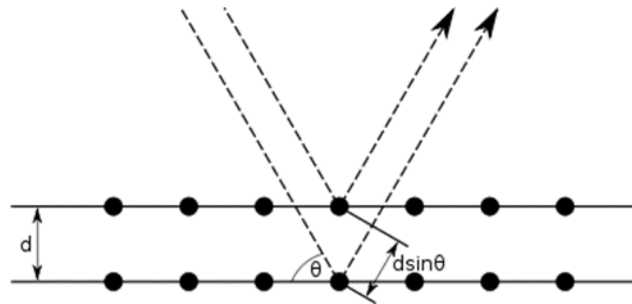


Figure 2.4 Diagram of two lattice planes diffracting a beam [8]

The signal of an XRD measurement correlates the received beam intensity with the 2θ angle. On specific values of the 2θ angle, a peak will appear. This peak relates to one of the crystal lattices of the sample, and by using Scherrer's equation (equation 2.9), the size of the crystal lattice can be obtained [8]:

$$L = \frac{K \cdot \lambda}{\beta \cdot \cos(\theta)} \quad (2.9)$$

where L is the crystal lattice size in the perpendicular plane of the diffraction plane, λ is the beam wavelength, K is a constant related to the crystalline structure, β is the width of the peak, and θ the angle between the normal and the diffracting plane.

2.6.2 Scanning electron microscopy

Scanning electron microscopy (SEM) is a characterization technique that produces images of a material sample by scanning the sample's surface with a focused beam of electrons. The imaging of the sample is achieved by an Everhart-Thornley detector that processes information about the position of the beam and the intensity of the incoming signal caused by the secondary electrons emitted by the surface atoms when they are excited by the electron beam [8].

As mentioned previously, the signals used for a SEM instrument to obtain an image are the results of the interaction of the electron beam with the atoms in the sample, as the secondary electrons. However, SEM can gather signals from other sources different from the secondary electrons (SE): back-scattered electrons (BSE), characteristic X-rays from the sample species, cathodoluminescence, and transmitted electrons. It is important to note that each signal it is required a different type of detector.

Secondary electrons have a very limited mean free path into solid material due to having very low energy. They can only provide images from the sample's surface and the top few nanometers after it. An advantage of using secondary electrons is that since the point of impact of the electron beam is highly localized, it allows for very high-resolution images from the surface sample. On the other hand, back-scattered electrons are the electrons reflected from the sample with much more energy than SE because of elastic scattering. Also, because of having higher power, the BSE can provide data from deeper layers of the sample.

Furthermore, BSE images provide information on the distribution of different elements in the sample [8]. Finally, characteristic X-rays can be emitted when the electron beam can excite an inner shell electron and consequently emit a distinct energy, from the atoms in the sample. The energy of the released X-ray can then be used to identify the specific elements present in the sample through energy-dispersive X-ray spectroscopy.

2.6.3 Energy-dispersive X-ray spectroscopy

Energy-dispersive X-ray spectroscopy (EDS, EDX, or EDXS) is a characterization technique used to analyze the presence of atomic elements in a sample through the excitation of the inner-shell electrons of an atom that will release a characteristic X-ray energy allowing its identification [35].

The ability to characterize the different elements present in a sample is based on the fundamental principle of Moseley's law [35]. This law states that each atomic element has a unique electronic structure that can only emit energy of a unique set of wavelengths on the electromagnetic spectrum.

To achieve the emission of these characteristic X-rays, a focus electron beam is applied to a sample. The sample, when the beam does not irradiate it contains atoms that have ground-state electrons. These electrons are located in discrete energy levels bound to the nuclei of the particle. A ground-state electron is ejected from the shell when the beam impacts these atoms, leaving behind an electron-hole. A higher-energy level electron then fills this hole, that due to this transfer, emits the excess energy by releasing an X-ray [35], as seen in Figure 2.5. The energy difference between the lower and higher energy (bandgap energy) level will dictate the wavelength of this X-ray.

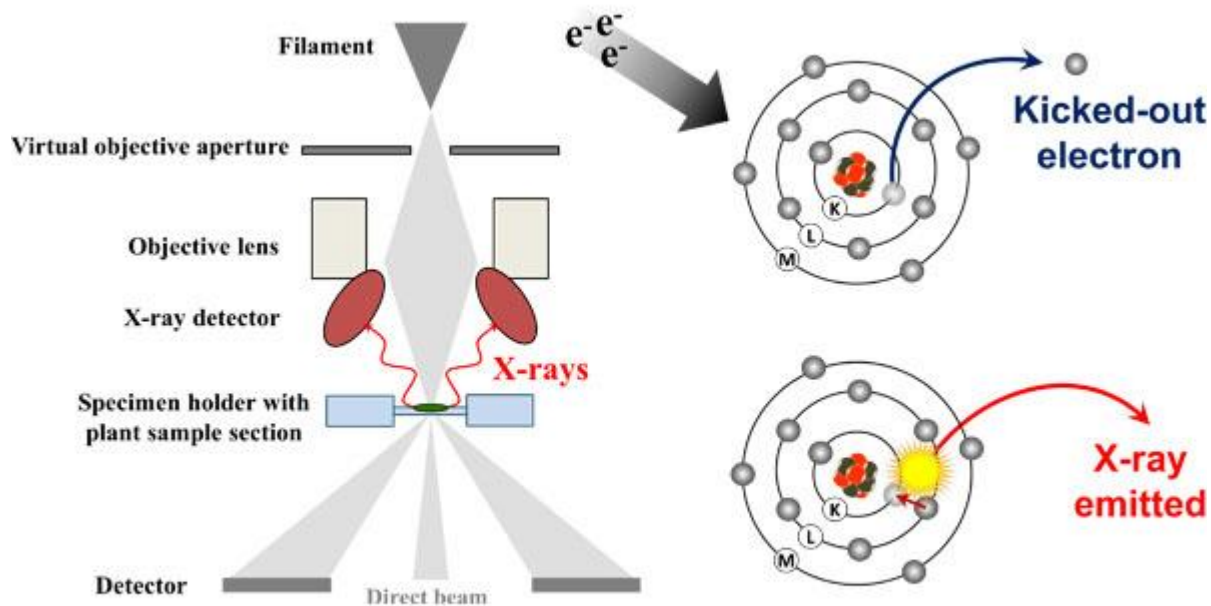


Figure 2.5 Diagram of an EDX instrument and its basic principal [36]

2.6.4 Ultraviolet-visible spectrophotometry

Ultraviolet-visible spectrophotometry (UV–Vis) is used to measure the absorption or reflectance of a liquid sample’s ultraviolet and visible spectra. This technique uses the principle that molecules absorb energy from incident light (photons) and excite their electrons to higher energy levels [37]. Depending on the sample, only specific photons with a unique wavelength will excite electrons to higher energy levels. The higher the energy level is, the shorter the wavelength must be to excite one electron to that level successfully [37].

By comparing the spectra emitted from a sample with absorbing species and one of a blank sample (which only contains the solvent), the concentration of the species can be determined. The Beer-Lambert law (equation 2.10) can quantify the concentration of the species [37].

$$A = \log_{10}(I_0/I) = \varepsilon \cdot c \cdot L \quad (2.10)$$

where A is the absorbance, I_0 is the intensity of incident light for a wavelength, I is the transmitted intensity through the sample, L is the path length through the sample, c the concentration of the absorbing species in the sample, and ε is the molar absorptivity or extinction coefficient, a constant.

2.6.5 Ultraviolet-visible diffuse reflectance spectroscopy

Ultraviolet-visible diffuse reflectance spectroscopy (UV-Vis DRS) is a characterization method similar to the previously described UV-Vis spectroscopy. Still, in this case, instead of measuring the absorption through transmission, remission is used. Remission is the reflected light, or back-scattered light, emitted by an opaque material when it is irradiated. Therefore, UV-Vis DRS is commonly used to evaluate the light absorbance spectra of solid materials, optically rough films, and powder samples [38].

When using UV-Vis spectrophotometry, the transmission spectrum is analyzed because the reflection of the light is specular, meaning that the studied samples, typically liquids, have a low light dispersion. When powders or other materials have a high surface roughness, meaning that the reflection is not specular, the transmission spectrum is too weak to measure the absorbance of the sample, and it is necessary to capture the full diffused range [39], as seen in Figure 2.6.

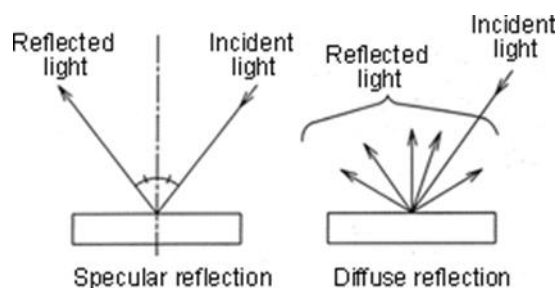


Figure 2.6 Scheme showing the difference between specular and diffuse reflection [39]

2.6.6 Fluorescence spectroscopy

Fluorescence spectroscopy is a characterization technique complementary to UV-Vis spectroscopy. It is used in the same wavelength range, but in this case, the obtained results from an excited state photon released from the sample have lower energy than when it was absorbed.

This phenomenon is explained by the Jablonski diagram, Figure 2.7. When studying the fluorescence of a sample, both the ground state and the excited state have their orbital levels with their vibrational sublevels. When a molecule absorbs a photon, an electron will go from a ground state to the excited level. The electron then can reach the excited state in its ground vibrational level or the excited state at a vibrationally excited level. This electron then can drop from an excited vibrational sublevel to a ground state sublevel through vibrational relaxation (due to collisions with other molecules causing the loss of vibrational energy), which emits energy non-radiatively (without emitting a photon) [40]. When the electron returns to the ground state level, it will emit a photon with lower energy (and longer wavelength) than the

initially absorbed photon. However, not all materials electronically excited fluoresce; in some cases, the electrons will decay to the ground state with only heat emission.

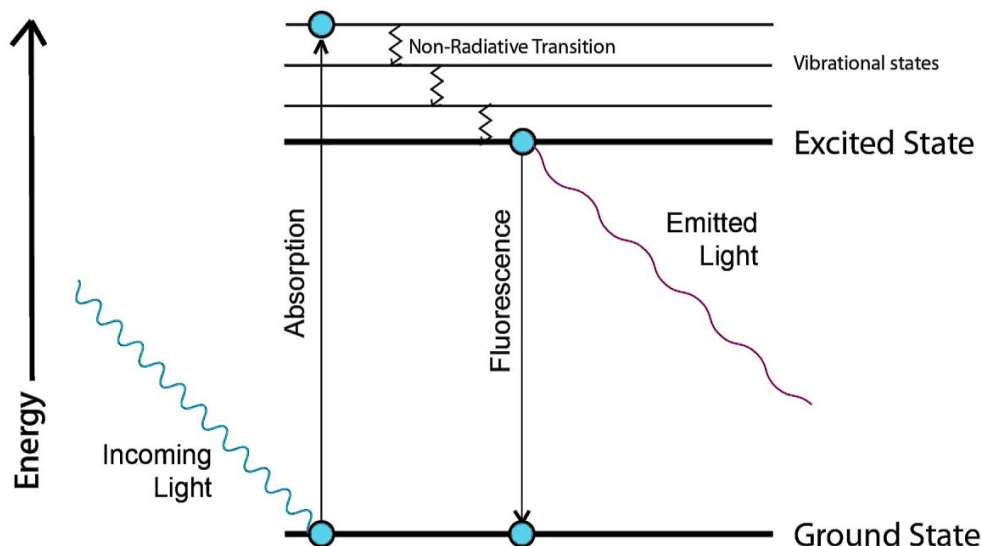


Figure 2.7 Jablonski diagram [40]

The instrument used is the fluorometer, and there are two types: filter fluorometers and spectrofluorometers. However, both follow the same principal design. In a fluorometer, light coming emitted from an excitation source (xenon arc lamp) passes through a filter or monochromator and impacts the sample. The sample absorbs the light and may fluoresce. Part of this fluorescent light will pass through a filter or monochromator and reach the detector. This detector is usually placed at 90° to the incident light beam to reduce the risk of transmitted or reflected incident light reaching the sensor [41], as depicted in Figure 2.8. Additionally, the fluorescent light can be measured from the front, which is done for opaque samples (e.g., solid materials).

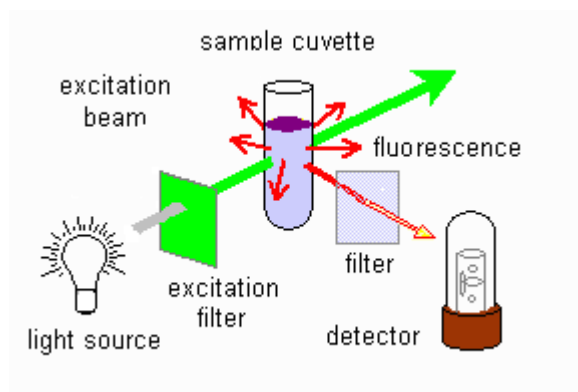


Figure 2.8 Diagram of a fluorometer [41]

This technique allows for the evaluation of the photoluminescence of a material. It is essential to evaluate this phenomenon for direct-gap semiconductors because high photoluminescence signifies high electron-hole pair recombination, which is directly affecting their efficiency as photocatalysts.

2.6.7 Fourier-transform infrared spectroscopy

Fourier-transform infrared spectroscopy (FT-IR) is a characterization technique that utilizes the molecular vibrations that occur when a molecule absorbs infrared radiation (IR). These vibrations have a unique frequency determined by the mass of the bonded atoms and the strength of the chemical bond [42].

For the FT-IR instrument to calculate these frequencies, an IR beam containing several frequencies of light is passed through the sample at once. The sample will absorb a particular part of this beam. Then another beam with a different set of frequencies will be used, and the absorption of the sample will also be measured. This process will be repeated many times over, and the data collected will determine the frequency of the vibration of the sample.

To collect this data, FT-IR uses an interferometer, depicted in Figure 2.9. This apparatus is formed by two mirrors, one fixed and one mobile, and a beam splitter. The IR beam coming from the source hits the beam splitter, and it is separated. One of the beams goes to the fixed mirror, and the other goes to the moving mirror. These two beams then are reflected to the beam splitter again and created an interference pattern (interferogram). This interferogram is then projected towards the sample and is collected by the detector. The interferogram is then transformed into an absorbance spectrum through the Fourier transform algorithm [42].

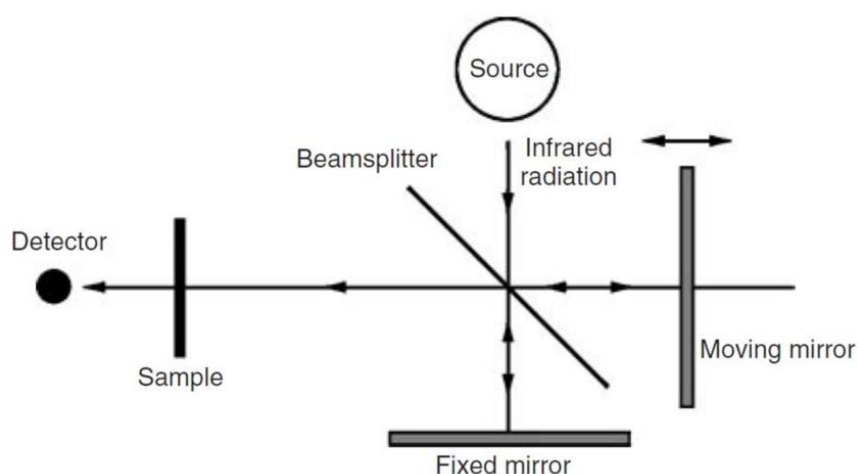


Figure 2.9 Diagram of an FT-IR instrument and interferometer [43]

2.6.8 Electron paramagnetic resonance spectroscopy

Electron paramagnetic resonance spectroscopy (EPR) is a characterization method utilized to analyze materials that have unpaired electrons in their structure. The working principle of this technique is the excitation of the spins of the electrons.

If an electron is exposed to an external magnetic field, it will develop a magnetic momentum and a spin quantum number ($m_s = +1/2$ or $m_s = -1/2$). The electron magnetic momentum will align itself to the magnetic field in an antiparallel or parallel manner, splitting the electron spin states (Figure 2.10).

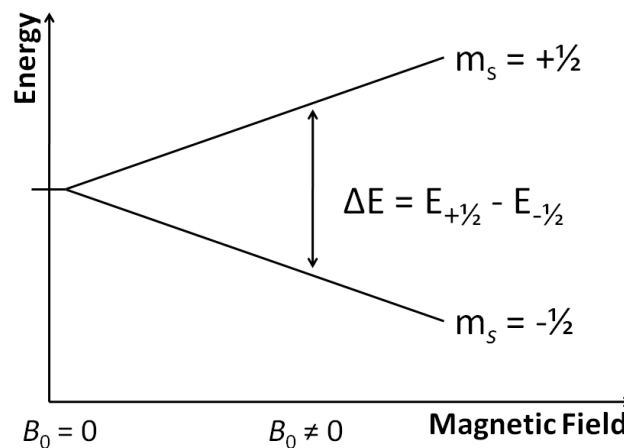


Figure 2.10 Splitting of electron spin states [44]

Unpaired electrons have the capacity of modifying their spin states by the absorption (from lower to upper state) or emission (from upper to lower) of a photon [45]. Following equation 2.11.

$$\Delta E = h \nu = g_e \mu_B B_0 \quad (2.11)$$

where ΔE is the energy difference between upper and lower spin state (proportional to the magnetic field's strength), h is Planck constant, ν is the wave frequency, g_e is the electron g-factor ($g_e = 2,0023$ for a free electron), μ_B is the Bohr magneton, and B_0 is the strength of the magnetic field. Equation 2.11 is fundamental for the usage of EPR spectroscopy.

When an EPR measurement is taken, a sample is exposed to a fixed microwave frequency and a varying magnetic field. By increasing this external field, the energy gap between the spin states is increased until it matches the microwave frequency energy [45]. At that point, unpaired electrons can, by interacting with photons, cross the energy gap and switch their spin state. Because of the Maxwell-Boltzmann distribution, there are always more electrons in the lower spin state, meaning that when the electrons can modify their spin, there will be a net absorption of photons. This absorption is then measured and converted to an

absorption spectrum. By obtaining the first derivative of this spectrum, we can get a reading whose intensity matches the number of unpaired electrons modifying their spin state. This technique then permits the retrieval of a quantitative measurement of unpaired electrons present in a material.

Unpaired electrons allow for the quantification of defects, like oxygen vacancies. By comparing different EPR measurements of different samples under the same conditions, it is possible to evaluate the number of defects present in different samples [46].

3 Materials and methods

3.1 Chemicals

The chemicals used on this project are listed below: Most of the chemicals were stored in chemical cabinets, but one required to be stored in a refrigerator (Sodium hypochlorite solution) :

- Copper nitrate trihydrate ($\text{Cu}(\text{NO}_3)_2 \cdot 3\text{H}_2\text{O}$): Sigma-Aldrich (Spain) p.a. 99.0 %
- Chromium nitrate nonahydrate ($\text{Cr}(\text{NO}_3)_3 \cdot 9\text{H}_2\text{O}$): Sigma-Aldrich (Spain) p.a. 99.0 %
- Cobalt nitrate hexahydrate ($\text{Co}(\text{NO}_3)_2 \cdot 6\text{H}_2\text{O}$): Sigma-Aldrich (Spain) p.a. 98.0 %
- Nickel nitrate hexahydrate ($\text{Ni}(\text{NO}_3)_2 \cdot 6\text{H}_2\text{O}$): Honeywell (Germany) p.a. 97.0 %
- Iron nitrate nonahydrate ($\text{Fe}(\text{NO}_3)_3 \cdot 9\text{H}_2\text{O}$): Sigma-Aldrich (USA) p.a. ≥ 99 %
- Sodium Hydroxide (NaOH): AnalaR NORMAPUR (Belgium) p.a. 99 %
- Phenol ($\text{C}_6\text{H}_6\text{O}$): Sigma-Aldrich (USA) p.a. ≥ 99 %
- Sodium citrate dihydrate ($\text{C}_6\text{H}_5\text{NaO}_7 \cdot 2\text{H}_2\text{O}$): Merck (Germany)
- Sodium hypochlorite solution (NaClO): Carl Roth (Germany), 12 % Cl technical
- Sodium nitroprusside ($\text{Na}_2\text{FeC}_5\text{N}_6\text{O}$): ACS (India) p.a. 99 %
- Deionized water (DI Water): VWR (Sweden)

3.2 Preparation of CuCr-LDH

3.2.1 Dropwise addition

For obtaining the copper-chromium layered double hydroxide, it is necessary to carry out a coprecipitation reaction followed by a hydrothermal synthesis step.

The coprecipitation reaction needs two solutions, one solution containing metallic nitrates, added to DI water, solution A, and another solution of 3M sodium hydroxide (NaOH), solution B. The added amounts of metallic nitrates can be seen in Table 3.1. These amounts are specific to maintain a certain molar ratio between the two samples, so a specific atomic ratio of metal cations in the layered double hydroxide structure can be obtained.

Solution A was put into a round bottom flask of 250 mL. This flask had a rotor spinning at 350 rpm. Solution B was introduced into a syringe. This syringe was later put onto a syringe pump. This apparatus was connected through a needle to one of the necks of the before

mentioned flask and is set to a syringe pump at a flow rate of 2 mL/min (see Figure 3.1). After 20 min, solution B was added entirely into the flask.



Figure 3.1 Picture of the dropwise addition synthesis setup

The mixing of both solutions had formed a blue suspension. This suspension was then transferred into a 90 mL Teflon-lined stainless-steel autoclave. This autoclave was sealed and placed into a furnace (Nabertherm calcination furnace) and was set to 120 °C and kept in for 12 hours.

Once the 12 hours had passed, the autoclave was let to cool down back at room temperature. Inside the autoclave, the suspension had separated into a slurry and liquid phase. The slurry phase was transferred into 50 mL centrifuge tubes and mixed with DI water. These tubes were later put into a centrifuge (Eppendorf Centrifuge 5810) for 8 min at 11000 rpm for four cycles. After each cycle, the supernatant was extracted from the tubes and replaced with DI water.

After the centrifugation step was completed, the tubes with the remaining solid were put into a furnace (Nabertherm calcination furnace) at 60 °C for 24 hours. Finally, the solid was taken out of the tubes and crushed into a fine powder with the help of a ceramic mortar.

Another synthesis was carried out using only 30 mL of each solution to reduce the total volume inside the autoclave and evaluate the effect of the condensation processes during the hydrothermal step.

3.2.2 Instant addition

The instant addition method is an alternative route for obtaining CuCr-LDH. It is still done by coprecipitation followed by hydrothermal synthesis. The main difference is that during the coprecipitation step, instead of adding solution B dropwise, it is added in the round bottom flask with solution A immediately.

Both solutions were prepared following the same procedure for the dropwise addition method. 40 mL of solution A is initially added into the round bottom flask, and the rotor is set at 350 rpm. Afterward, 40 mL of solution B were added to the flask. The stirring speed was increased to 700 rpm, and the solutions were left mixing for 5 minutes.

The suspension was transferred into a 90 mL Teflon-lined stainless-steel autoclave, and an identical hydrothermal step from the previous procedure was carried out (12 hours at 120 °C). The solid obtained was then centrifuged four times and was finally left drying in a furnace for 24 hours at 60 °C.

3.2.3 Ternary LDH synthesis

The synthesis of ternary LDH was carried out identically to the dropwise addition process described earlier in this chapter. The main differences from this procedure and the dropwise one were that: solution A was composed of three metallic nitrates, instead of two; and since some of these new metallic nitrates had a higher water content than the previous two used, only 30 mL of solution A and B were added initially, to avoid filling the autoclave liner completely. For this project, three ternary CuCr-LDH were synthesized: with iron, cobalt, and nickel.

Additionally, for the CuCrFe-LDH, two samples were prepared. Initially, the LDH was prepared as all the others following the standard dropwise addition. Still, it was reported that iron-containing LDH has issues being synthesized unless the environment has basic conditions (high pH). Therefore, a second sample was synthesized, where solution B was added initially to the round bottom flask, and solution A was added dropwise utilizing the syringe pump. The values for preparing solution A were not modified.

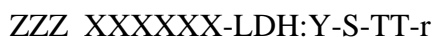
3.2.4 Alkali etching

In order to synthesis the etched layer double hydroxide, 300 mg of catalyst were dissolved in 40 mL of a water solution containing NaOH, which was used as the etching agent. The concentrations used were 0,5 M, 1 M, 2 M, and 3 M, respectively. The 40 mL of NaOH

solution was poured into a beaker, and then it was placed onto a stirring plate. The rotation speed was set to 500 rpm, and finally, 300 mg of catalyst were added. The catalyst was left in the solution stirring for 4 hours. Once the time had passed, the solutions were put into centrifuge tubes. The tubes were then put into the centrifuge (Eppendorf Centrifuge 5810) at 11000 rpm for 10 min. Afterward, the supernatant was removed from the tubes, and DI water was added instead. The centrifugation step was repeated three more times. Finally, the tubes with the remaining solid were placed into a furnace (Nabertherm calcination furnace) for 24 hours at 60 °C to dry.

3.2.5 Nomenclature and classification

Since up to 16 different catalysts have been synthesized during this thesis, a standard terminology was established to quickly identify the catalyst properties and the methods used on that specific material.



ZZZ indicates if the catalyst has been treated with alkali etching (0,5E means etching treatment was used with a 0,5 M concentration of etching agent). *XXXXXX* indicates the different metal cations present in the material (e.g., CuCoCr), while LDH stands for layered double hydroxide. *Y* refers to the value of the stoichiometric ratio between the divalent and trivalent cations ($M^{2+}:M^{3+} = Y$). *S* stands for which addition method was used for the catalyst synthesis. It can either be *D* (dropwise addition method) or *I* (instant addition method). *TT* refers to the initial volume of solution used for the coprecipitation process, and it can be 30 or 40, depending on if 30 mL or 40 mL were used. Finally, *r* indicates the order in which the solutions for the coprecipitation step were mixed (a: solution B was added to answer A and b: solution A was added to solution B).

Table 3.1 All synthesized materials names and characteristic properties

Catalyst	Metals present	M²⁺:M³⁺ ratio	Addition method	Initial volume solution [mL]	Coprecipitation addition order	Etching treatment [M of NaOH]
CuCr-LDH:1-D-40-a	Copper, Chromium	1	Dropwise	40	Solution B to A	-
CuCr-LDH:2-D-40-a	Copper, Chromium	2	Dropwise	40	Solution B to A	-
CuCr-LDH:2-I-40-a	Copper, Chromium	2	Instant	40	Solution B to A	-
CuCr-LDH:3-D-40-a	Copper, Chromium	3	Dropwise	40	Solution B to A	-
CuCr-LDH:5-D-40-a	Copper, Chromium	5	Dropwise	40	Solution B to A	-
CuCr-LDH:2-D-30-a	Copper, Chromium	2	Dropwise	35	Solution B to A	-
CuCr-LDH:2-D-30-b	Copper, Chromium	2	Dropwise	35	Solution B to A	-
CuCrFe-LDH:2-D-30-a	Copper, Chromium, Iron	2	Dropwise	35	Solution B to A	-
CuCrFe-LDH:2-D-30-b	Copper, Chromium, Iron	2	Dropwise	35	Solution A to B	-
CoCuCr-LDH:2-D-30-a	Cobalt, Copper, Chromium	2	Dropwise	35	Solution B to A	-
CuNiCr-LDH:2-D-30-a	Copper, Nickel, Chromium	2	Dropwise	35	Solution B to A	-
0,5E-CuCr-LDH:2-D-40-a	Copper, Chromium	2	Dropwise	35	Solution B to A	0,5
1,0E-CuCr-LDH:2-D-40-a	Copper, Chromium	2	Dropwise	35	Solution B to A	1
2,0E-CuCr-LDH:2-D-40-a	Copper, Chromium	2	Dropwise	35	Solution B to A	2
3,0E-CuCr-LDH:2-D-40-a	Copper, Chromium	2	Dropwise	35	Solution B to A	3

3.3 Characterization

In this next section, the instruments, their specifications, and the necessary procedures used in this project to characterize the catalysts will be presented.

3.3.1 XRD

To use the XRD to analyze the LDH based catalysts was necessary to use Kapton foil over the holder containing the samples. This procedure was taken to reduce and prevent the risk of a fine powder present in the sample from becoming airborne and being inhaled by the people working in the XRD lab. The preparation of the holder with the sample was carried inside a fume hood. The Kapton foil was subjected to the holder using a plastic ring that is inserted around the sample.

The instrument used for the XRD measurements was a Bruker D8 A25 DaVinci X-ray diffractometer with $\text{CuK}\alpha$ radiation of wavelength $\lambda=1.54060 \text{ \AA}$ with an electric current of 40 mA and a voltage of 40 kV. The duration of each measurement was of 60 minutes, with a 2θ range between 5 to 75° . Initially, the measurements were done using a variable divergence slit, but to improve the results obtained, a fixed slit was used.

Finally, the raw data spectra obtained were processed with the Bruker AXS DIFFRAC.EVA (v5.2) software.

3.3.2 SEM and EDX

Images of the catalyst's samples were obtained using the Hitachi High-Tech SU9000 in-lens cold field emission electron microscope. The detectors used were the secondary and low- and high-angle back-scattered electrons. This instrument's acceleration current ranges between 0,1 to 30 kV, and the maximum beam current is 20 μA . All the samples were imaged with an acceleration current of 10 kV and a beam current of 10 μA . The samples for SEM were prepared over a Silicon wafer. The sample was initially diluted in ethanol, then the resulting solution was sonicated, and with a pipette, one droplet was added on top of the wafer. Afterward, the wafer was left until all the ethanol evaporated.

Additionally, to the SEM images procured with this instrument, EDX mapping was also obtained. This microscope has an Oxford Ultim Extreme 120 mm^2 EDS system optimized to function with the SU9000, this allows for the measurement of elemental maps in a very short time, just some minutes are needed instead of hours as required on other systems. Furthermore, the SU9000 is placed in an electromagnetic field-free room on vibration isolated ground.

3.3.3 UV-Vis DRS

To carry the UV-Vis DRS measurements, the Avantes AvaLight-DH-S (see Figure 3.2) was utilized. This instrument has both deuterium and halogen sources to cover the full UV-Vis range, and it is necessary to switch them on 20 minutes before taking any measurement. It is required to establish a baseline; therefore, a blank measurement was taken first. This measurement should be carried with a completely white material to obtain a very low absorption baseline to allow the complete evaluation of a solid diffusion spectrum. For this calibration, BaSO₄ was selected. All the experiments were carried out by analyzing the spectra from 400 to 800 nm, since the main objective is to evaluate the behavior of the samples under the visible range.

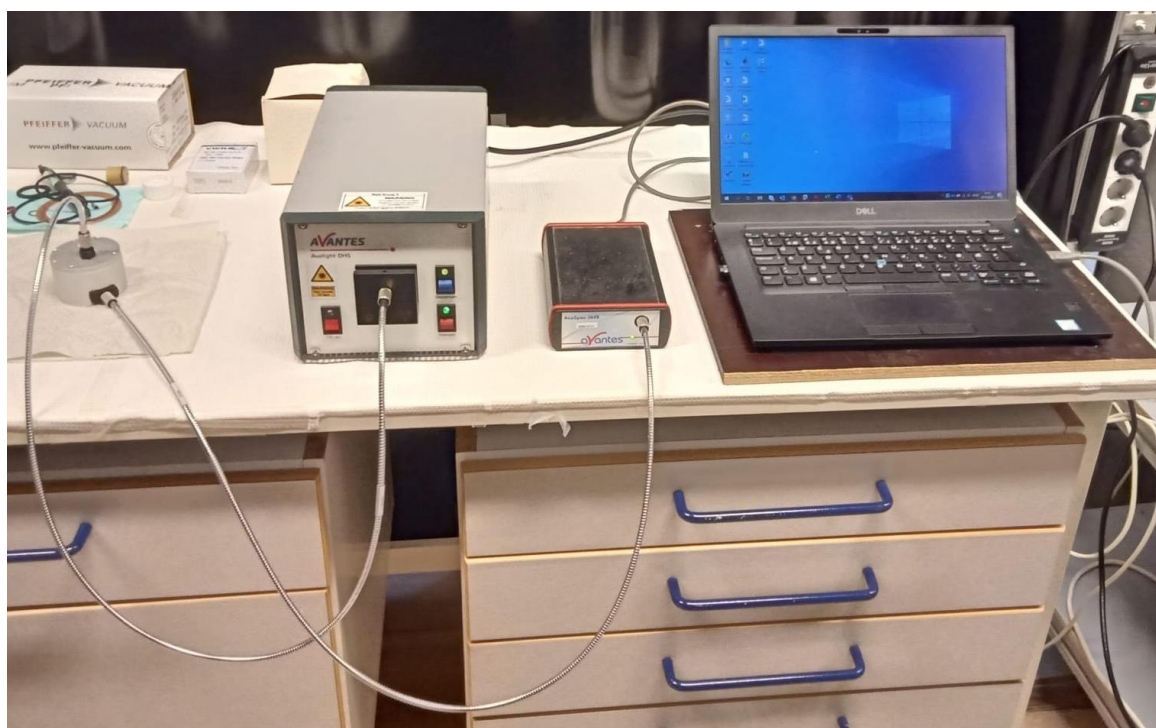


Figure 3.2 Picture of the Avantes AvaLight-DH-S spectrophotometer

At the left side of Figure 3.2, the integrating sphere of the UV-Vis DRS instrument can be observed. This object allows capturing the full diffuse spectrum coming from a sample. As shown in Figure 3.3, inside it, a completely white surface allows for all the diffuse light to be collected by the instrument.

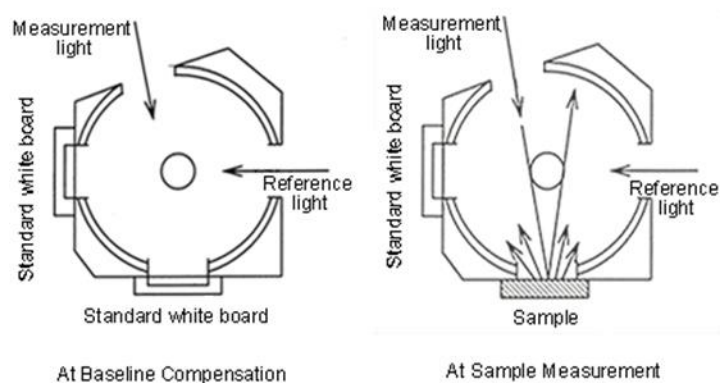


Figure 3.3 Scheme of integrating sphere (white sphere collector) of a DRS apparatus [39].

3.3.4 Fluorescence spectroscopy

For the fluorescence spectroscopy measurements, the Fluorolog-3 HORIBA Jobin Yvon apparatus was used. This instrument was equipped with a Xenon Short Arc lamp as the light source, SPEX DM302, PC ACQ model as the detector, and used the FluorEssence software for data processing.

The xenon lamp was switch on 20 minutes beforehand when taking a measurement. Since the analyzed samples were solids, the FF (forward-facing) detector was utilized. The starting wavelength was set to 365 nm (15 nm higher than the excitation wavelength), and the measurements were taken until 700 nm.

3.3.5 FT-IR spectroscopy

FT-IR measurements were carried out using a Bruker Tensor 27 FT-IR spectrometer equipped with a single reflection ATR cell diamond crystal (MKII Golden Gate™, Specac). The software used for the instrument was the Opus 4.2 software. All the readings were done with the same parameters: the resolution of 4 cm^{-1} and 64 scans per measurement. Additionally, the range was set from 500 to 4000 cm^{-1} .

For the baseline measurements, they were taken both with the anvil open, and the anvil closed. This was done to evaluate the possible presence of artifacts due to the state of the instrument. For the sample measurements, enough sample mass was put on top of the device's crystal until it was entirely covered by it. Afterward, the anvil was closed and tighten on top.

3.3.6 EPR spectroscopy

For EPR measurements, the samples must be pretreated, and a vacuum is required. For each sample, 50 mg of catalyst were introduced into a high purity silica capillary. This capillary (Figure 3.4) was then connected to a pumping set-up.



Figure 3.4 Picture of an EPR silica capillary

This set-up (Figure 3.5) had a Leybold Trivac D1 6B oil pump connected to a liquid nitrogen trap (LNT 25S) and a Leybold turbomolecular pump system PT 50. Up to three capillaries could be connected at once. The capillaries were left for three days connected into the system until the pressure reached 10^{-4} mbar (10^{-5} mbar is preferred, but this set-up could not achieve that). After the vacuum is completed is necessary to melt and seal the capillaries to prevent the loss of the vacuum.

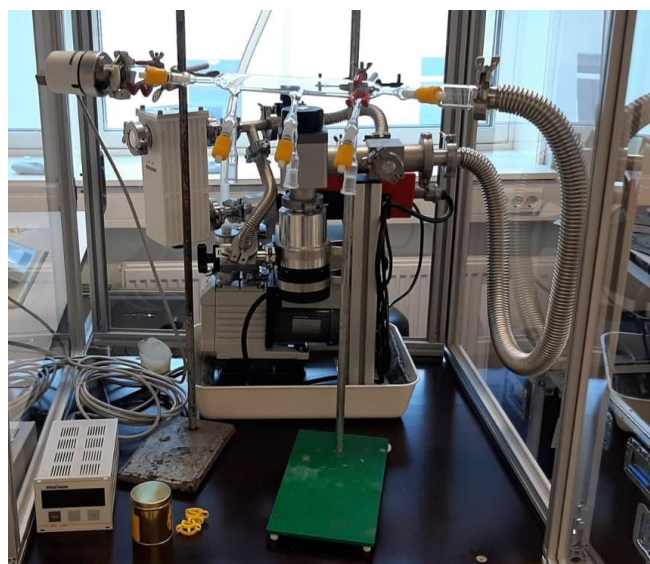


Figure 3.5 Picture of pumping set-up

EPR measurements were done with a Bruker 300 spectrometer at room temperature. It is essential to check that the diode current is set to 200 μ A. Initially, for the project samples, the calibration of the apparatus was carried out with a Strong Pitch Calibration Sample (ER-213-SPS). Once the sample was put into the spectrometer, the modulation amplitude was set to 0,100, and the receiver gain to 23 dB.

3.4 Photocatalytic set-up

The set-up used in this project to carry out the photocatalytic reaction experiment, seen in Figure 3.6, consists of 4 key components. Firstly, a nitrogen tank that supplies the reactor with the necessary reactant, secondly a mass flow controller (MFC), thirdly a black box, where

the reactor is placed in darkness while the experiment is set up. Once the experiment starts, the box allows for a focused light beam to be projected onto the reactor. Additionally, inside the black box, there is a stirring plate to allow for the solubilization of N_2 into the water inside the reactor. Finally, a bubble trap enables the reactor to be kept at a stable pressure and ensures that nitrogen flows through the reactor.

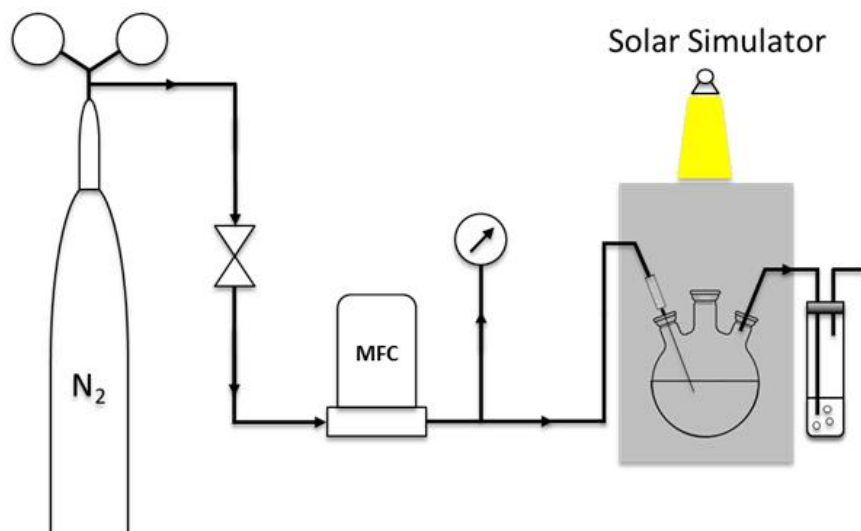


Figure 3.6 Diagram of the photocatalytic set-up used for this project

3.5 Photocatalytic reaction experiment

The reactions experiments were carried out in a 150 mL quartz round bottom flask with three necks. In each experiment, 10 mg of catalyst were weighted and added into the flask, after that, 100 mL of DI water was also added. Afterward, the flask containing the diluted catalyst was sonicated for 10 minutes. Immediately after, the flask was then placed inside the black box. Once set, a stirring magnet was put into the flask, and the stirring plate was switched on. One of the necks of the flask was connected to the bubble trap, while on another one, a septum was placed. A needle connected to a tube attached to the mass flow controller was introduced on the septum, and both the MFC and the valve of the nitrogen canister were switched on. The MFC was set to 50 mL/min. At the same time, the lamp was switched on and was set to the right intensity, but without opening the lamp's lit. After 30 min of letting N_2 flowing into the flask, the needle was taken out, and all necks were disconnected and closed with stoppers. The flask was then let for 10 min in complete darkness to allow the nitrogen gas inside to homogenize into the DI water. After the time passed, the lamp was placed at 13 cm from the flask (measuring from the light source of the lamp to the center of the flask), and the lamp's lit was removed. The flask was let illuminated for one hour.

Once one hour has passed, with the help of a syringe, 6 mL of the reaction medium were taken out and placed in Eppendorf tubes. These tubes were then placed in a mini centrifuge (Eppendorf MiniSpin Plus), which was set at 14.500 rpm for 10 min. After centrifuging, the supernatant is rapidly taken out of the Eppendorfs and was placed into a vial. From this vial, 3 mL were taken and put into another vial with a pipette. Into this vial, it was also added 0.12 mL of phenol solution, 0.12 mL of sodium nitroprusside solution, and 0.3 mL of an oxidizing solution. Immediately after, the vial was closed and covered in aluminum foil to avoid light exposure, as the reaction that was taking place between the reactor aliquot and the added chemicals is light sensitive.

After two hours had passed since adding the substances in the vial, a sample of the vial solution is placed into a UV-Vis spectrophotometer, and measurement (or reading) was taken.

The solutions mixed in the vial with the aliquot are necessary to obtain indophenol blue, which is the substance measured by the UV-Vis spectrophotometer. These solutions were prepared beforehand. For the phenol solution, 20 g of crystalline phenol were dissolved into 100 mL of ethanol (p.a. 95 %) and was kept in a brown-glass bottle in darkness. The sodium nitroprusside solution was prepared by dissolving 0.5 g of sodium nitroprusside in 100 mL of DI water, and it was also kept in the same conditions as the phenol solution. Finally, the oxidizing solution was prepared moments before adding it to the vial (as it should not be stored). It was made by mixing 0.5 mL of sodium hypochlorite solution (12% concentration, and needs to be kept in a refrigerator) with 2 mL of alkaline solution (the alkaline solution was prepared by dissolving 40g sodium citrate and 2g of NaOH into 200 mL of DI water).

3.6 Photocatalytic activity measurement

The direct measurement of ammonia in solution is not feasible by UV-Vis spectrophotometry alone. Previously, the Nessler reagent method was extensively used to determine the concentration of diluted ammonia. Recently though, it was reported by Sun et al. [38] that the Nessler technique indicates a higher concentration of ammonia due to the interference of sacrificial agents used during the reaction.

To measure the reaction activity then another method was necessary. In this project, an aliquot of the reaction medium was taken, then it was mixed with phenol and hypochlorite in an alkaline medium, as explained previously, to obtain indophenol blue. Indophenol blue is an intensely blue-colored amino-derivative of phenylquinone-monoamine. Its presence allows for the coulometric measure of ammonia present in the solution, as the obtained color is

proportional to the ammonia concentration. Sodium nitroprusside is added to intensify the coloration at room temperature further to facilitate the measurement.

A Shimadzu UV-2401PC UV-visible spectrophotometer performed the UV-Vis spectroscopy. The light source had to be switched on for 20 minutes before using it. Before taken a measurement, a baseline correction was established by taking a blank measurement using only the solvent used in the reaction (DI water). All readings were taken at room temperature, and the scanning range was from 400 to 800 nm since the indophenol blue peak is set around 640 nm.

4 Results and discussion

Firstly, the different properties of the various catalysts will be discussed in this subchapter, with the results obtained with XRD, UV-Vis DRS, SEM, EDX, FT-IR, and Fluorescence and EPR spectroscopy. The information obtained from the catalysts' characterization, includes the synthesized materials' crystallinity, phase purity, absorbance, bandgap energy, particle size, elemental composition, bonding structure, and photoluminescence, is presented. Secondly, the performance of the synthesized catalyst in the ammonia photosynthesis reaction are reported and briefly discussed.

4.1 Characterization of the CuCr-LDH species

In this section, the different catalyst properties of interest are discussed from the data obtained during the realization of this work.

4.1.1 Crystallinity and phase purity

The XRD results in this subsection are divided into two parts. Firstly, the CuCr-LDH species with a different ratio of metal cations are discussed. This project concluded that the best cation ratio to work with CuCr-LDH was 2; all results presented after for other improved LDH-type materials are built upon this assumption. Secondly, the newly synthesized CuCr ternary LDH materials, which lack available literature, are also discussed.

The XRD results of CuCr-LDH:1-D-40-a, CuCr-LDH:2-D-40-a, CuCr-LDH:3-D-40-a, and CuCr-LDH:5-D-40-a are presented in Figure 4.1.

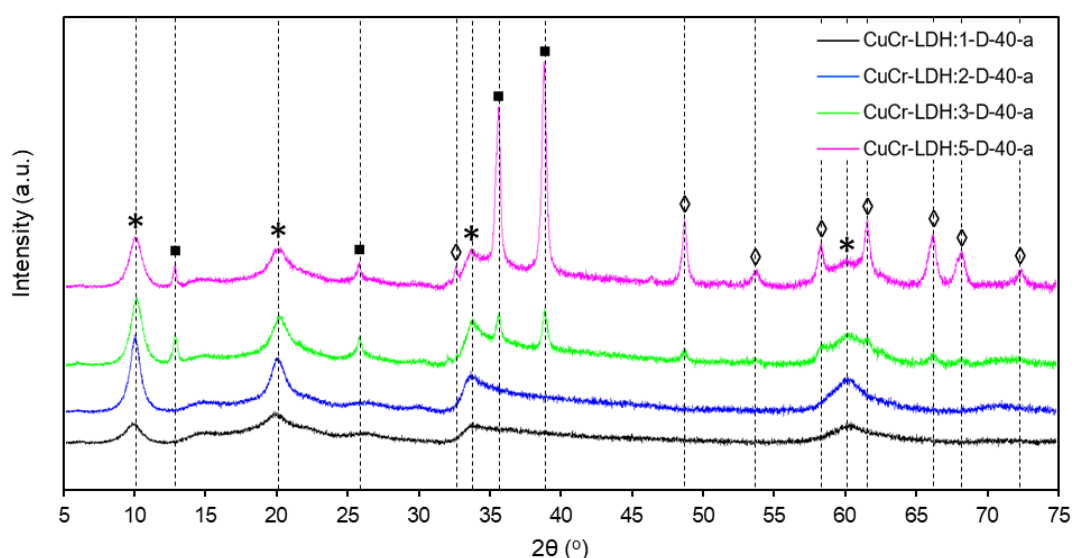


Figure 4.1 XRD results for CuCr-LDH:1-D-40-a, CuCr-LDH:2-D-40-a, CuCr-LDH:3-D-40-a, and CuCr-LDH:5-D-40-a.

All species exhibit three clear Bragg's reflections, at $2\theta = 10,1^\circ$ (003), $20,4^\circ$ (006), and $34,3^\circ$ (009). These reflections demonstrate that these materials have a layered hexagonal structure with an R-3m rhombohedral symmetry [47]. Therein, the previous literature supports the successful synthesis of a layered double hydroxide structure. Additionally, all four samples show a broad Bragg reflection at $2\theta = 60,4^\circ$, this reflection peak (110) is associated with an in-plane hexagonal turbostatic structure incorporated within the general LDH structure, indicated both with black asterisks (*). However, a part from the LDH related reflection peaks, additional peaks can be observed in both CuCr-LDH:3-D-40-a and CuCr-LDH:5-D-40-a samples. Firstly, a set of reflection peaks identified the presence of a Cu(OH)(NO₃) species [48] are designated with black squares (▪). Secondly, the reflection peaks corresponding to the existence of Cu(OH)₂ [49] are indicated with white diamonds (◇).

These two additional phases that are not part of the intended layered double hydroxide structure can be attributed to the excess of copper nitrate during the synthesis step. As mentioned in the Theory chapter 2.4, LDH structures require a stoichiometric ratio of divalent and trivalent cations. Usually, this ratio can be assessed by the hydrotalcite chemical formula (equation 2.6). If the stoichiometric value of the trivalent cation (denoted as x in equation 2.6) is between 0.2 and 0.33, It should form the LDH structure. Although recently it was discovered that certain trivalent cations, chromium included, allow for further accommodation of ions in the LDH structure, and in some cases, x could be upwards of 0,5 [50]. This phenomenon permits greater tuning of these materials in applications like photocatalysis. An inconvenience to this capability is that it only works when the trivalent cation is increased. If decreasing the presence of the trivalent cation, in favor of the divalent cation is intended. The actual threshold of $x > 0,2$ remains, which elucidates the precipitation of additional phases out of the LDH structure in the samples of CuCr-LDH:3-D-40-a and CuCr-LDH:5-D-40-a, with the highest Cu presence. Table 4.1 presents the value of x for each species. Unfortunately, in this project, precipitation of additional phases was observed for a value of $x = 0,25$ in CuCr-LDH:3-D-40-a, which contradicts the state of the art of LDH preparation.

Table 4.1 CuCr-LDH samples with their Cu²⁺/Cr³⁺ ratio and x value

Sample	Cu ²⁺ /Cr ³⁺ ratio	x
CuCr-LDH:1-D-40-a	1	0,500
CuCr-LDH:2-D-40-a	2	0,333
CuCr-LDH:3-D-40-a	3	0,250
CuCr-LDH:5-D-40-a	5	0,167

The presence of additional phases in the CuCr-LDH causes an apparent change in coloration shown in Annex C.

In Figures 4.2 and 4.3, a comparison between XRD patterns of CuCr-LDH:2-D-30-a and CuCrFe-LDH:2-D-30-a ternary-LDH and the patterns of CuCr-LDH:2-D-30-b and CuCrFe-LDH:2-D-30-b ternary-LDH are shown, respectively.

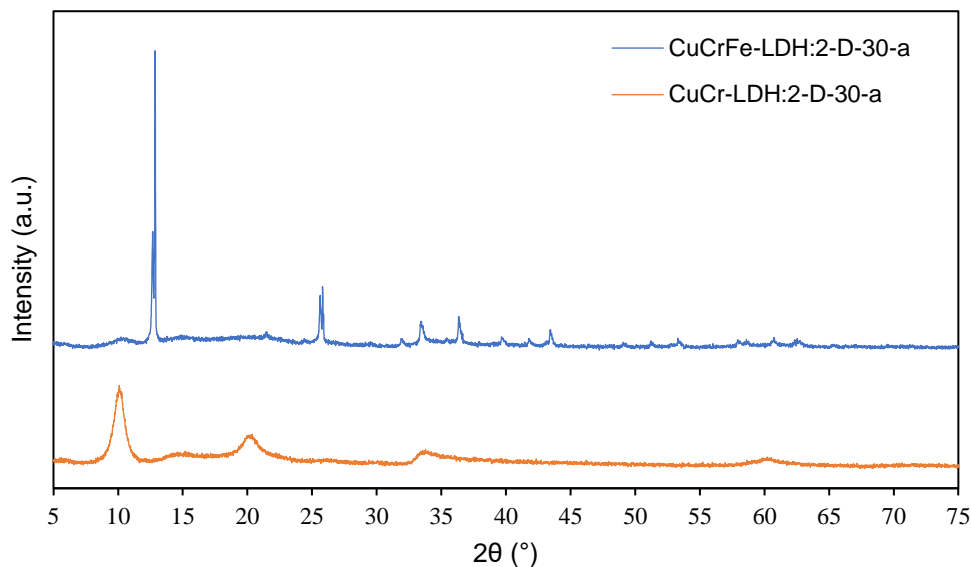


Figure 4.2 XRD results of CuCr-LDH:2-D-30-a and CuCrFe-LDH:2-D-30-a

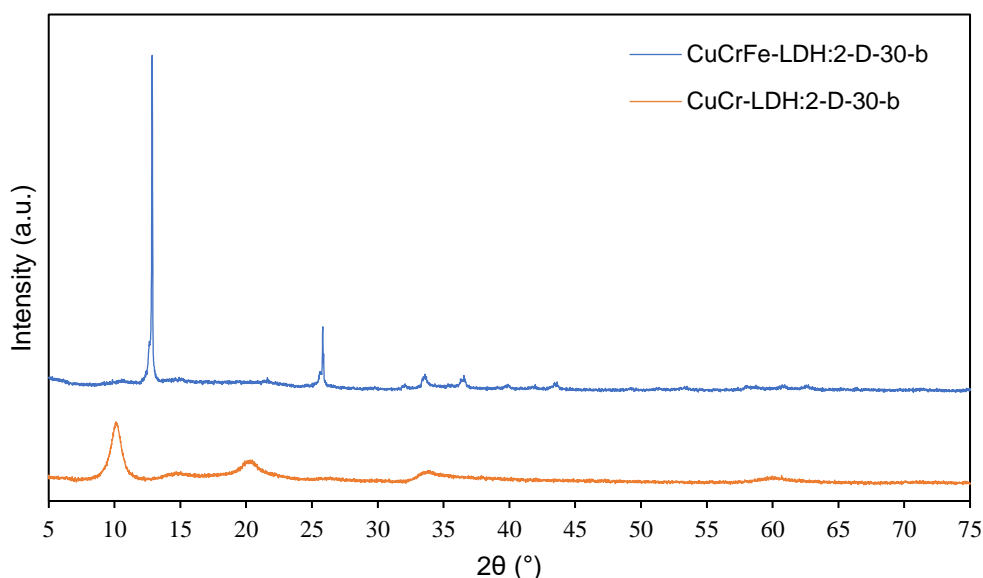


Figure 4.3 XRD results of CuCr-LDH:2-D-30-b and CuCrFe-LDH:2-D-30-b

The CuCrFe species display neither the (00x) reflections belonging to the layered hexagonal rhombohedral crystalline structure nor the (110) reflection affiliated to the in-plane

hexagonal turbostatic structure, characteristic from LDH materials. Instead, two peaks are observed at $2\theta = 12,8^\circ$ and $25,8^\circ$. Additionally, to these peaks, several other peaks are observed at higher 2θ value ($2\theta = 33,6^\circ$, $36,4^\circ$, and $43,4^\circ$) and additional minor ones around 30° , 40° , 50° , and 60° . This is the first time to report this material in the literature. Therefore, this project has not successfully identified a crystalline phase that would fit them. However, the reflection peaks at 30° , $36,4^\circ$, and 60° might be related to the presence of a $\text{Fe}(\text{OH})_3$ phase [51].

The literature reports that synthesizing LDH containing Fe can be difficult due to the complex chemistry, resulting in the formation of Fe impurities like oxy-hydroxides (amorphous to X-ray diffraction) and crystalline spinel phase [48]. It is reported in several sources that the formation of Fe containing LDH at low or moderate pH can cause the appearance of a $\text{Fe}(\text{OH})_3$ phase. Nonetheless, a high pH setting (high supersaturation conditions) is reported to suppress the formation of Fe impurities during the LDH synthesis [48].

All catalysts, except CuCr-LDH:2-D-30-b and CuCrFe-LDH:2-D-30-b, have been synthesized by adding the NaOH solution dropwise to the metallic nitrates solution during the coprecipitation step, to keep the pH constant as reported in the Methods chapter for the Fe containing LDH. For both CuCr-LDH:2-D-30-b and CuCrFe-LDH:2-D-30-b, the solution of the metallic nitrates was added dropwise to the NaOH solution. As shown in Figure 4.2 and Figure 4.3, the material with the inverse addition has much lower reflection peaks corresponding to the possible impurities, $2\theta = 30^\circ$, $36,4^\circ$, and 60° , (meaning the impurities were not able to form crystalline cells as large as in the synthesis at lower pH). In comparison, the Bragg reflections of the CuCr-LDH samples remain unchanged. However, the LDH-type structure was still not successfully achieved.

In Figure 4.4, X-ray diffraction patterns corresponding to CuCr-LDH:2-D-30-a, CoCuCr-LDH:2-D-30-a, and CuNiCr-LDH:2-D-30-a are presented.

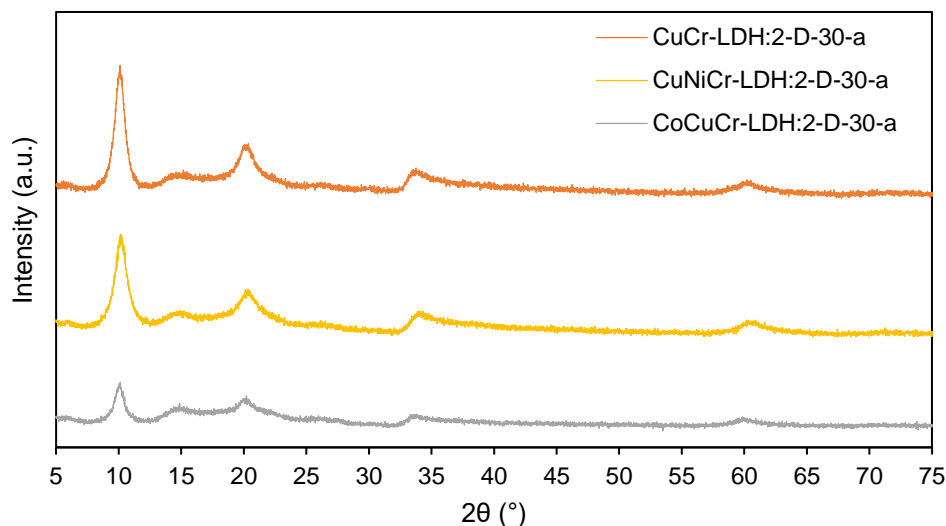


Figure 4.4 XRD patterns of CuCr-LDH:2-D-30-a, CoCuCr-LDH:2-D-30-a, and CuNiCr-LDH:2-D-30-a

The obtention of the ternary CuCr-LDH by addition of Co and Ni was successfully performed. As observed in Figure 4.4, both species have the expected Bragg reflections corresponding to an LDH-like material (following the hexagonal rhombohedral crystalline and the in-plane hexagonal turbostatic structures). Furthermore, a decrease in crystallinity is observed compared with the CuCr species synthesized under the same conditions. A reduction in crystallinity can have positive and negative repercussions for a photocatalyst. On the one hand, defects, as explained in the Theory section 2.4.2, can be advantageous for photocatalysts as they increase the amount of V_O available. On the other hand, the decrease of crystallinity can cause crystal defects that could act as luminescence centers, increasing undesired nonradiative recombination [52].

UV-Vis fluorescence measurements were taken to better understand the effect of recombination by measuring the luminescence on these ternary LDH materials. These results will be discussed later in this chapter.

Finally, it is essential to remark that both CoCuCr-LDH:2-D-30-a and CuNiCr-LDH:2-D-30-a are completely new materials never previously reported on the literature (at the time of the delivery of this Mater Thesis), and they could function as interesting new materials for photocatalysis or other applications since they have perfectly replicated the characteristics of LDH-type compound.

4.1.2 Absorbance and bandgap energy

The UV-Vis DRS characterization technique was used to obtain data referring to all synthesized materials' absorbance patterns under the visible spectrum, ranging from 400 to 800 nm. It will also enable the estimation of the bandgap energy of these substances.

Figures 4.5, 4.6, and 4.7 present the absorbance spectra under the visible light for all the samples with different stoichiometric ratios of Cu and Cr, all the CuCr-LDH etched samples, and all ternary CuCr-LDH, respectively.

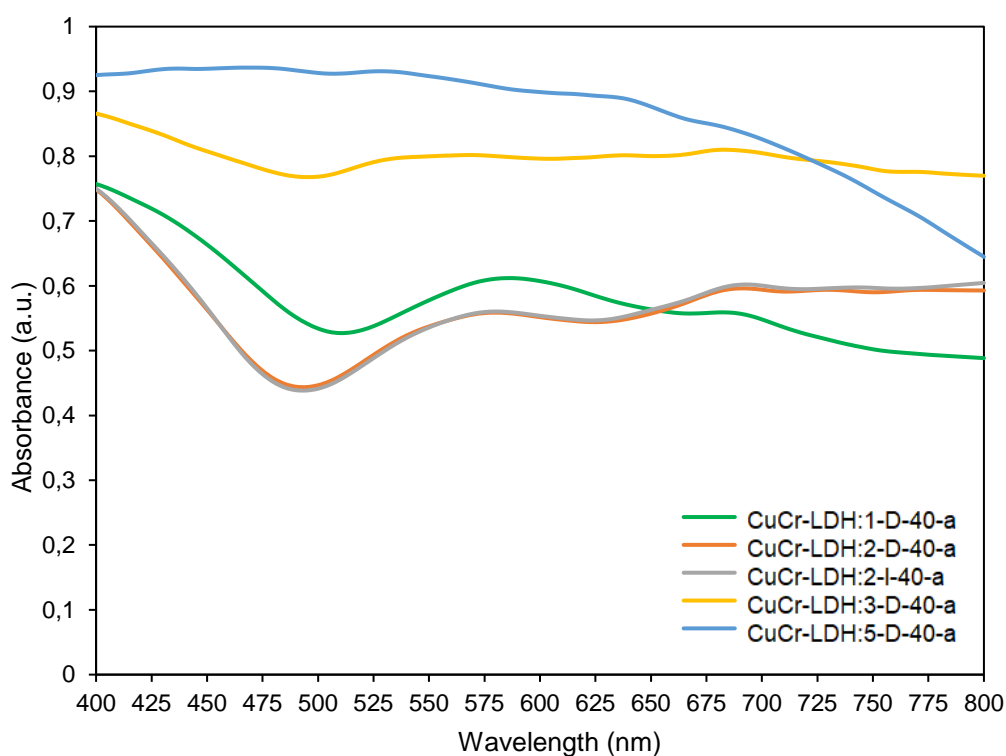


Figure 4.5 Absorbance spectra of CuCr-LDH:1-D-40-a, CuCr-LDH:2-D-40-a, CuCr-LDH:2-I-40-a, CuCr-LDH:3-D-40-a, and CuCr-LDH:5-D-40-a

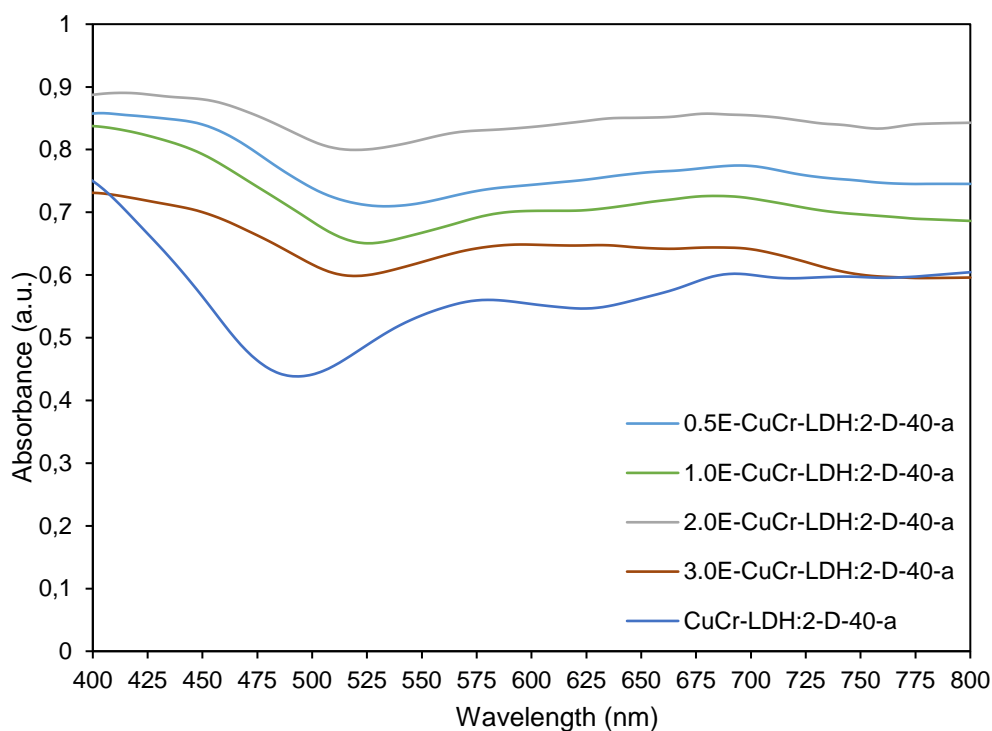


Figure 4.6 Absorbance spectra of CuCr-LDH:2-D-40-a, 0,5E- CuCr-LDH:2-D-40-a, 1,0E- CuCr-LDH:2-D-40-a, 2,0E- CuCr-LDH:2-D-40-a, and 3,0E-CuCr-LDH:2-D-40-a

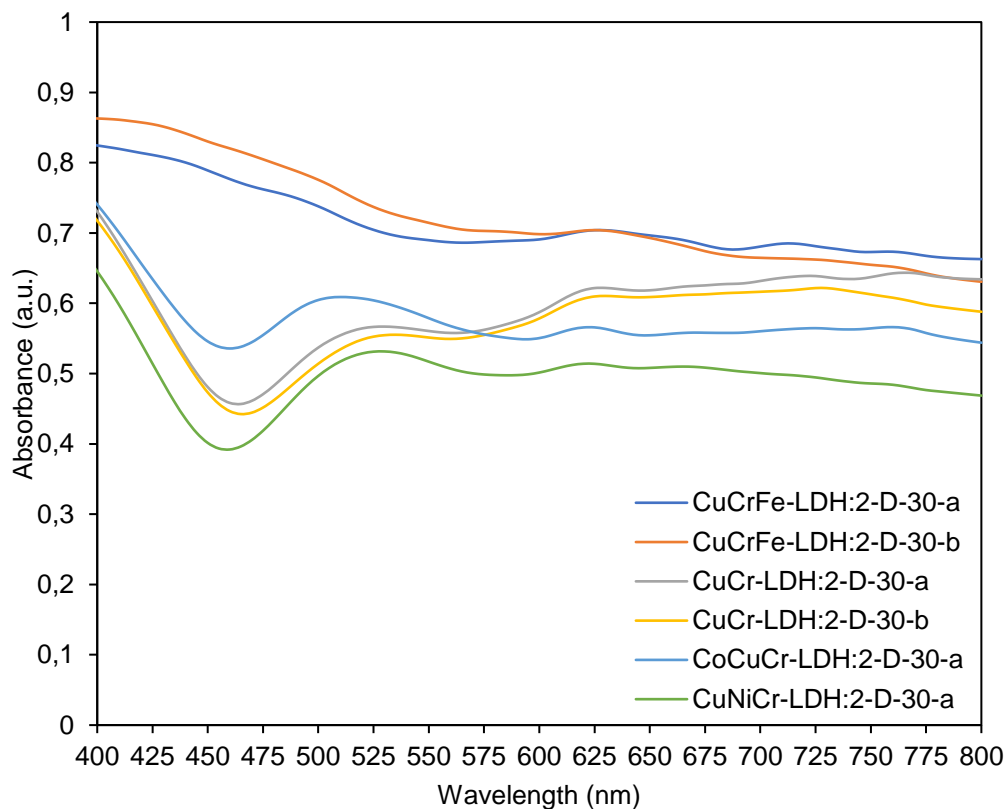


Figure 4.7 Absorbance spectra of CuCr-LDH:2-D-30-a, CuCr-LDH:2-D-30-b, CuCrFe-LDH:2-D-30-a, CuCrFe-LDH:2-D-30-b, CoCuCr-LDH:2-D-30-a, and CuNiCr-LDH:2-D-30-a

From the previous Figures, it can be observed that all samples have a primary peak below the 400 nm threshold and a second one between 500-600 nm, except CuCr-LDH:5-D-40-a, CuCrFe-LDH:2-D-30-a, and CuCrFe-LDH:2-D-30-a. These three samples lack the necessary peaks in the absorbance spectrum to have bandgap energy of interest, rendering them unfit to function as photocatalysts. The experimental results portray that all the etched samples have a higher absorbance than the unetched LDH samples. The difference between the peaks (the concave area where the bandgap energy can be estimated) is much less prominent, indicating a considerable reduction of the bandgap energy compared to the unetched samples. In contrast, the unetched CuCr-LDH:3-D-40-a sample has a similar spectrum; in this case, the reason might be the presence of additional phases since CuCr-LDH:5-D-40-a, with a higher content of impurities, has an entirely flat spectrum, in the range of interest.

It is possible to estimate the bandgap energy with the absorbance spectrum of a compound and the Tauc plot (check Annex A for all Tauc plots used). In Table 4.2, all the obtained bandgap energy is presented.

Table 4.2 Bandgap energy of all CuCr-LDH species

Sample	Bandgap energy (eV)
CuCr-LDH:1-D-40-a	1,97
CuCr-LDH:2-D-40-a	2,21
CuCr-LDH:2-I-40-a	2,21
CuCr-LDH:3-D-40-a	1,79
CuCr-LDH:5-D-40-a	-
0,5E-CuCr-LDH:2-D-40-a	1,72
1,0E-CuCr-LDH:2-D-40-a	1,81
2,0E-CuCr-LDH:2-D-40-a	1,60
3,0E-CuCr-LDH:2-D-40-a	1,75
CuCr-LDH:2-D-30-a	2,20
CuCr-LDH:2-D-30-b	2,21
CuCrFe-LDH:2-D-30-a	-
CuCrFe-LDH:2-D-30-a	-
CoCuCr-LDH:2-D-30-a	2,12
CuNiCr-LDH:2-D-30-a	2,24

These bandgap energies obtained successfully demonstrate the potential of the synthesized catalysts in photocatalysis for nitrogen fixation and ammonia synthesis under

visible light. CuCr-LDH:5-D-40-a, CuCrFe-LDH:2-D-30-a, and CuCrFe-LDH:2-D-30-b will be no longer characterized since they are not viable catalysts for the reaction of interest. Additionally, the photocatalytic performance of all pure CuCr-LDH materials (CuCr-LDH:1-D-40-a, CuCr-LDH:2-D-40-a, CuCr-LDH:2-I-40-a, and CuCr-LDH:3-D-40-a) was carried out during the same time of the absorbance measurements in the project, and those results are presented at the end of this chapter section. These results concluded unequivocally that the best performance was of the CuCr-LDH:2-D-40-a, all new characterization techniques utilized from this point onwards focus on the species with a Cu:Cr ratio of 2.

4.1.3 Morphology

SEM images were taken to characterize all the materials synthesized from the CuCr-LDH to analyze differences in the morphology of pure LDH samples and the etched and ternary LDH. In this section, images of CuCr-LDH:2-D-40-a, 0,5E-CuCr-LDH:2-D-40-a, 1,0E-CuCr-LDH:2-D-40-a, 2,0E-CuCr-LDH:2-D-40-a, 3,0E-CuCr-LDH:2-D-40-a, CuCr-LDH:2-D-30-a, and CoCuCr-LDH:2-D-30-a will be reported and comment.

In Figures 4.8 a and 4.8 b, SEM images of CuCr-LDH:2-D-40-a are shown. It can be observed the presence of broad particles across the sample. Additionally, in Figure 4.8 b, a magnified image of the surface of one agglomerate can be observed. The texture is rough, and no regular frameworks can be discerned.

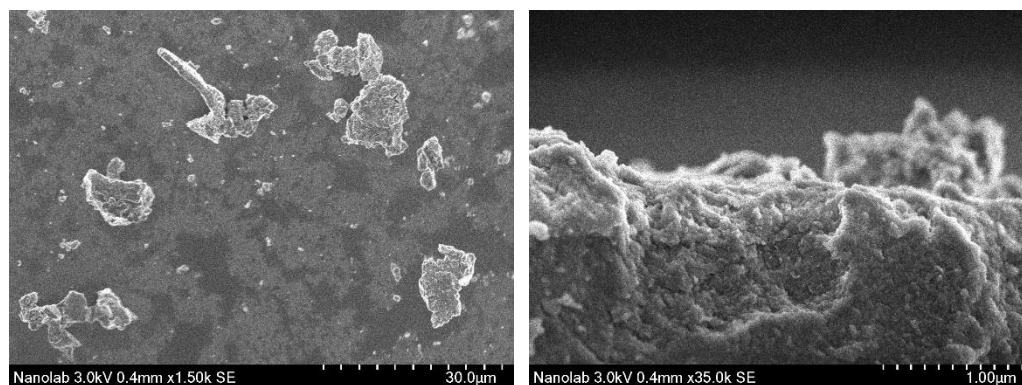


Figure 4.8 a (left) and b (right) SEM images of CuCr-LDH:2-D-40-a

Another characteristic observed is that the particles are voluminous. It does not have a layered material appearance, with a more sheet-like shape, which would be expected. This phenomenon was previously reported by Zhang et al. [25]: during the synthesis of LDH-type materials, two different structures can be obtained, bulk or nanosheets. Nanosheets LDH has a wrinkled sheet structure, with a disordered arrangement of the various sheets that provide boundaries with plenty of surface defect sites (Vo). In contrast, bulk structures have a much lower number of surface defects since they have a larger size and crystalline domain length

(reducing the number of boundaries) and trapping many active sites inside the bulk of the particles. Moreover, variations in the coordination around the Cr atoms between the nanosheet and bulk were also reported. It was highlighted that an increase in coordination site disorder is persistent with the formation of abundant V_O [25].

In Figures 4.9, 4.10, 4.11, and 4.12, SEM images of different etched CuCr-LDH samples are presented.

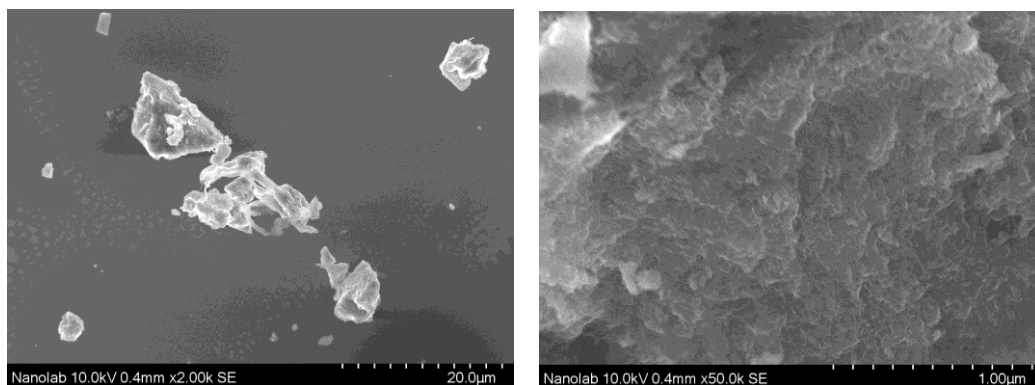


Figure 4.9 a (left) and b (right) SEM images of 0,5E-CuCr-LDH:2-D-40-a

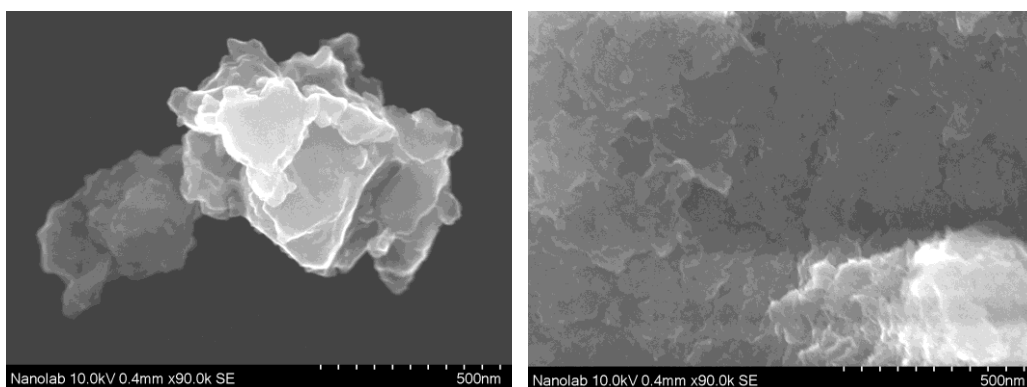


Figure 4.10 a (left) and b (right) SEM images of 1,0E-CuCr-LDH:2-D-40-a

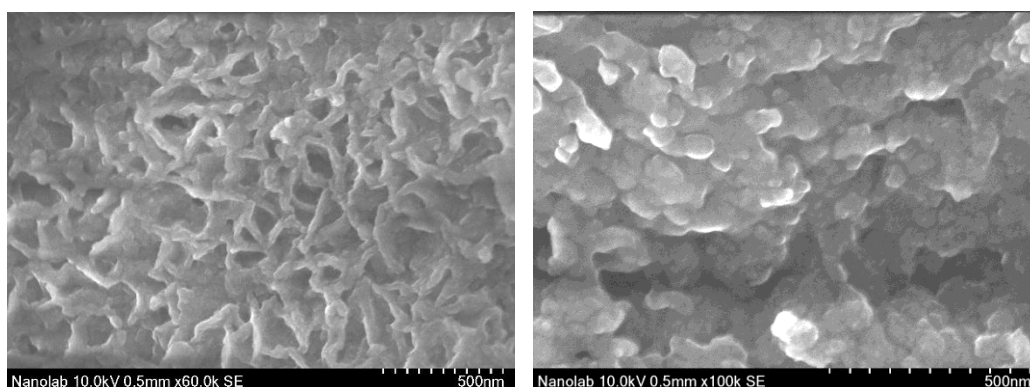


Figure 4.11 a (left) and b (right) SEM images of 2,0E-CuCr-LDH:2-D-40-a

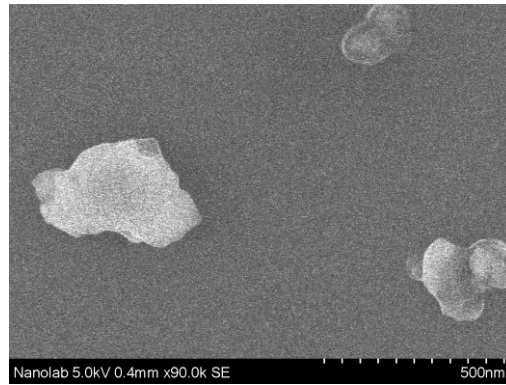


Figure 4.12 SEM image of 3,0E-CuCr-LDH:2-D-40-a

As it can be observed, the surface of the particles in all etched samples is much rougher, except for 0,5E-CuCr-LDH:2-D-40-a (Figure 4.9 a and b), which still has a similar texture to CuCr-LDH:2-D-40-a (Figure 4.10 a and b). In 2,0E-CuCr-LDH:2-D-40-a (Figure 4.11 a and b), the most interesting morphologies were observed. In some aggregates, the extended particles from the surface are smoothed completely (Figure 4.11 b), while in others, the surface resembled a disordered net-like structure (Figure 4.11 a). The etched particles were similar to the three-dimensional bulk structured of CuCr-LDH:2-D-40-a. However, the average size of the particles was slightly reduced, except in 0,5E-CuCr-LDH:2-D-40-a (Figure 4.9 a and b).

In Figures 4.13 and 4.14, SEM images from CuCr-LDH:2-D-30-a and CoCuCr-LDH:2-D-30-a are shown, respectively. Unfortunately, CuNiCr-LDH:2-D-30-a particles, when impregnated on the Si wafer for SEM characterization, will form a cluster that could be perceived with the naked eye. Therefore, no SEM images were taken of the last sample.

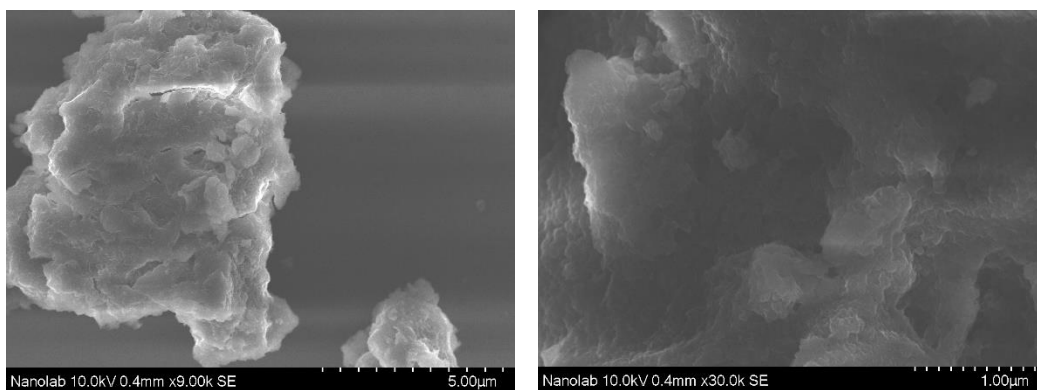


Figure 4.13 a (left) and b (right) SEM images of CuCr-LDH:2-D-30-a

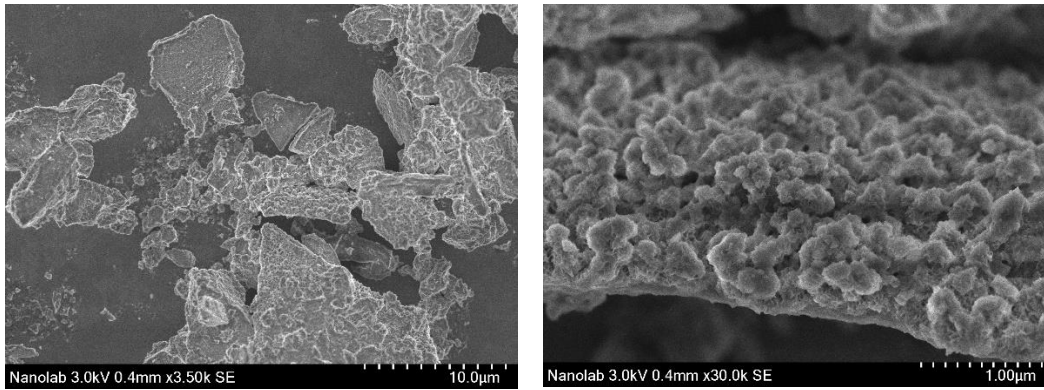


Figure 4.14 a (left) and b (right) SEM images of CoCuCr-LDH:2-D-30-a

In CoCuCr-LDH:2-D-30-a, it was observed more accumulation of the particles in small clusters. This phenomenon could be related to the preparation of the sample on the Si wafer, or it could be associated with the addition of a third cation in the LDH structure. Not much information was available in the literature. The surface morphology of CoCuCr-LDH:2-D-30-a was peculiar relative to other catalysts, as shown in Figure 4.14 b, a sprout-like characteristic shape was observed relative to CuCr-LDH:2-D-30-a (Figure 4.13 b).

The particles sizes in all materials developed during this project are large compared to other studied materials in the same field in the literature [25] [47] [48] [53]. An explanation for this difference is higher agitation speeds (around 2000 to 3000 rpm) were used in other literature sources [25] during the coprecipitation step, instead of the 350 rpm used. This limitation was due to the set-up available for the coprecipitation procedure. With the flask and volumes used, if agitation were to be increased, splashing would occur, preventing the solutions from being homogeneously mixed and difficulting the obtention of reproducible batches.

4.1.4 Element detection

In Table 4.3, the weight percentage of the detected elements in EDX of several etched samples and both CuCr-LDH and CoCuCr-LDH are shown. The EDX maps from where the data is taken are presented in Annex B.

Table 4.3 Elemental composition obtained by EDX of several LDH samples

Sample	Cu (%)	Cr (%)	O (%)	C (%)	Co (%)
0,5E-CuCr-LDH:2-D-40-a	25,09	15,45	40,91	18,55	-
1,0E-CuCr-LDH:2-D-40-a	30,18	5,45	56,36	8,00	-
2,0E-CuCr-LDH:2-D-40-a	29,65	4,52	57,29	8,54	-
CuCr-LDH:2-D-30-a	21,26	12,15	44,47	22,13	-
CoCuCr-LDH:2-D-30-a	10,14	11,17	39,52	29,38	9,79

In all samples, the main components of the layered double hydroxide were detected as expected (Cu, Cr, O, and Co). However, in all samples, carbon was also measured. This occurrence is highly unexpected as there is no C source in all the synthesis procedures used in this project. Plausible explanations for this phenomenon could be that the carbon detected belongs to the ethanol used to disperse the sample onto the silicon wafer needed for SEM utilization. Another source could be the carbon contamination present in the vacuum chamber of the SEM instrument. EDX is not the most accurate characterization technique for the quantitative detection of light elements like carbon. Although, for the same reason, the oxygen detected should also be taken with some caution as it is also a light element.

Regarding the metal elements detected, the results are expected the divalent cations (Cu and Co) are present in higher percentages than the trivalent cation (Cr) since all studied species had the divalent:trivalent ratio of 2. Interestingly, the Cr percentage is significantly reduced with respect to Cu in both 1,0E-CuCr-LDH:2-D-40-a and 2,0E-CuCr-LDH:2-D-40-a, which could be the result of etching. The literature suggests [25] that the etching does not exclusively interact with oxygen in the LDH structures but interacts with the cations, generating cation vacancies. Cations can interact differently with the etching agent, justifying a more aggressive removal of certain species. In this case, there were not specific sources regarding the relation of Cu and Cr with NaOH as etching agent, but it could be a feasible explanation. However, in sample 0,5E-CuCr-LDH:2-D-40-a, it does not seem to happen the same phenomenon. Since the particles size is much more prominent in this sample than in the other two, it is also possible that the effect is not as noticeable.

4.1.5 FT-IR of ternary LDH

FT-IR readings were taken to analyze the different bondings present in the upgraded CuCr-LDH materials and compared them to the source material to evaluate all possible changes observed. Both CuCr-LDH:2-D-30-a and the ternary LDH CoCuCr-LDH:2-D-30-a and CuNiCr-LDH:2-D-30-a samples were characterized using this instrument.

In Figure 4.15, the FT-IR spectra of both ternary-LDH, CoCuCr-LDH:2-D-30-a and CuNiCr-LDH:2-D-30-a, are compared to the spectra of their precursor CuCr-LDH:2-D-30-a. In Figure 4.16, the background readings were taken during the FT-IR measurements to demonstrate the presence of artifacts that affected and influenced the actual readings for the studied samples. Each spectrum presented in Figure 4.15.a is made of the single-channel signal corrected using the background with anvil closed.

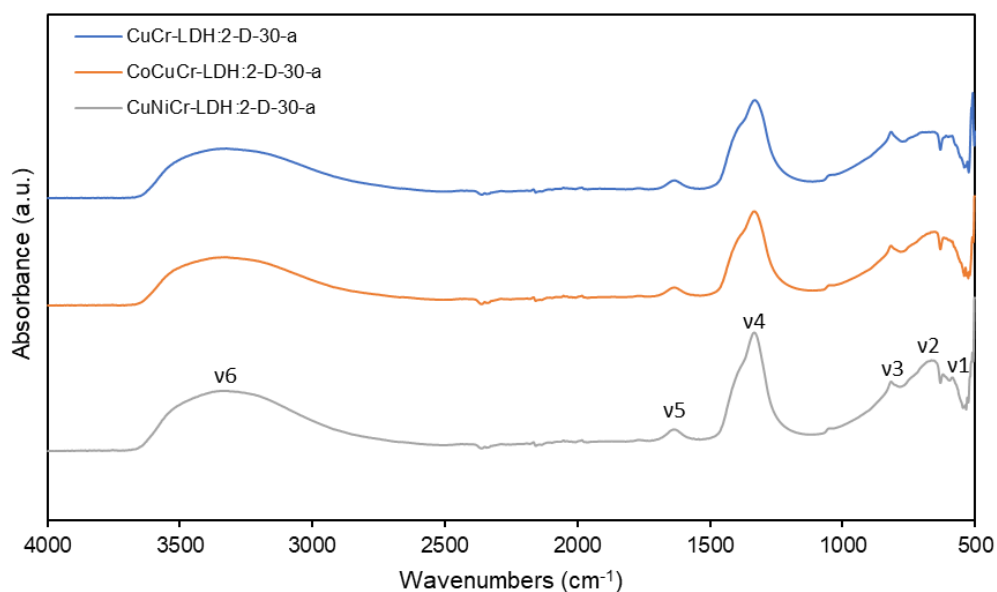


Figure 4.15 FT-IR spectra of samples CuCr-LDH:2-D-30-a, CoCuCr-LDH:2-D-30-a, and CuNiCr-LDH:2-D-30-a

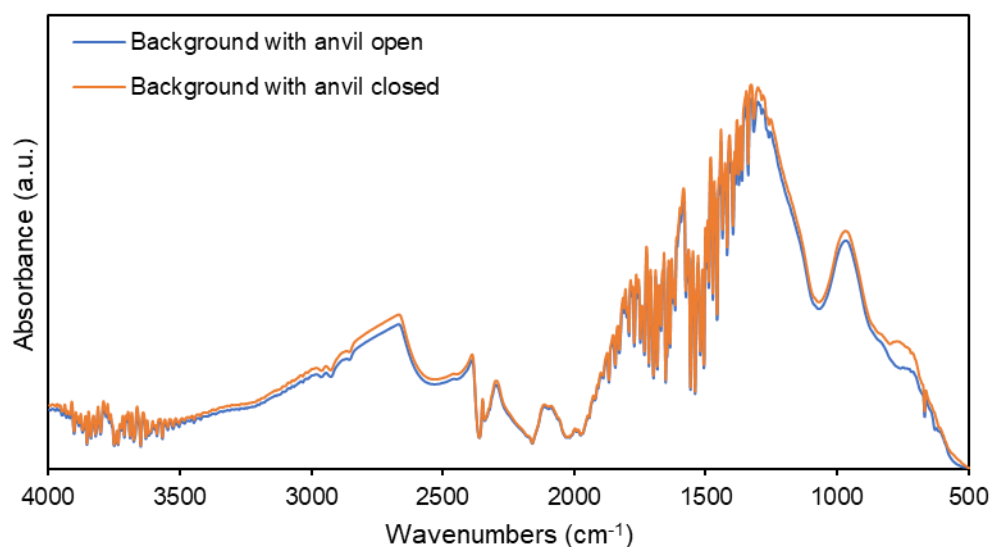


Figure 4.16 FT-IR baseline measurements with both the anvil open and closed

The reason for using the baseline taken when the anvil was closed is because, in the range of 600 to 800 cm^{-1} , an artifact causes an increment on the baseline. Since the sample's readings are done with the anvil closed, it is assumed that this artifact will also be present on the obtained signal and therefore need to be accounted for. In the range of 1800 to 2800 cm^{-1} , additional artifacts also affected the readings in Figure 4.15. These artifacts are attributed to either the anvil or the crystal from the FT-IR instrument and are entirely unrelated to the actual samples studied. However, the first artifact interacts with an area of interest; some of the signals from the sample appear in the same region (range of 600 to 900 cm^{-1}). Finally, the aberrations

in the ranges of 3500 to 4000 cm^{-1} and 1200 to 2000 cm^{-1} are attributed to the CO_2 and H_2O present in the atmosphere.

All three samples exhibit a broad peak (v6), in the range of 2500 to 3600 cm^{-1} , and another less broad and pronounced peak (v5), at 1620 to 1640 cm^{-1} . These peaks correspond to the hydroxyl group vibration and the stretching vibration of the interlayer water molecules, respectively [47] [53]. The three samples also display a prominent peak (v4), at 1200 to 1500 cm^{-1} , corresponding to the bending vibration of the intercalated NO_3^- ions [47] [53]. Finally, the peaks v1, v2, and v3, present in the range of 500 to 800 cm^{-1} , are exemplary of the bending and stretching vibration of M-O-M, O-M-O and M-O (where M = Co, Cu, Cr, and Ni; and O = oxygen atoms) [47]. Overall, these results established the successful integration of Co and Ni into the CuCr-LDH structure to form the ternary-LDH.

4.1.6 Photoluminescence of ternary LDH

As previously stated, Uv-Vis fluorescence spectroscopy was carried out to analyze the photoluminescent in the newly synthesized materials. Only the ternary LDH samples were tested (CoCuCr-LDH:2-D-30-a and CuNiCr-LDH:2-D-30-a) and CuCr-LDH:2-D-30-a, as there was not enough samples mass to study the etched samples.

Photoluminescence is associated with recombination processes in a photocatalyst. This can significantly affect the efficiency of the overall photocatalytic process and therefore is essential to evaluate this phenomenon. The morphology of the LDH-type materials has been reported to influence the luminescence activity to a certain degree [54].

In Figure 4.17, the photoluminescence emission spectrum for CoCuCr-LDH:2-D-30-a and CuNiCr-LDH:2-D-30-a are correlated to the emission spectrum of CuCr-LDH:2-D-30-a

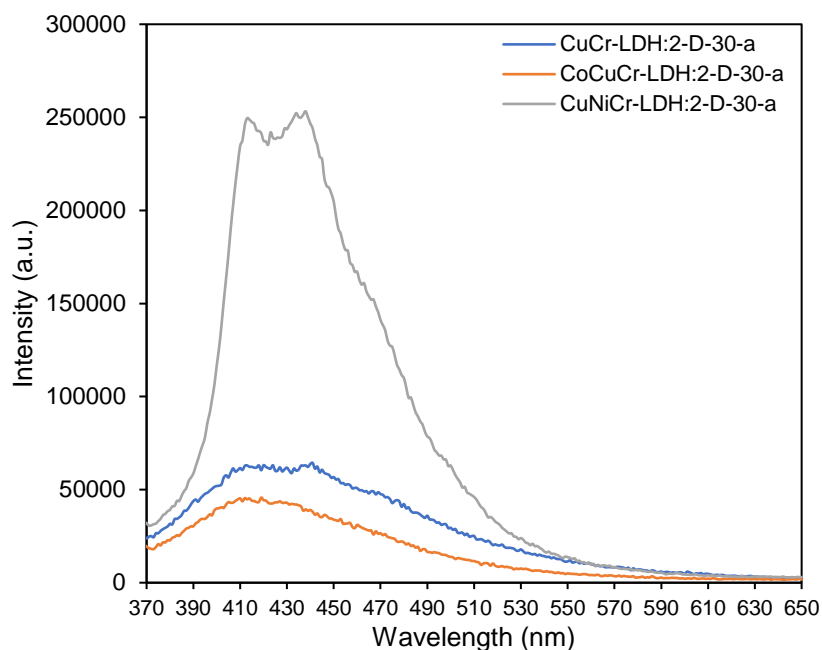


Figure 4.17 Fluorescence spectra of CuCr-LDH:2-D-30-a, CoCuCr-LDH:2-D-30-a, and CuNiCr-LDH:2-D-30-a

The three materials displayed a strong photoluminescence emission peak at 420 nm due to charge carrier capture on the surface [55]. If the two ternary LDH are compared, it is observable that the addition of Co reduces the photoluminescence. In contrast, a significant increase in photoluminescence was observed with the addition of Ni to the CuCr-LDH material. The CoCuCr-LDH:2-D-30-a exhibits the lowest electron-hole pair recombination rate and therefore is the material with the highest electron-hole pair separation efficiency.

4.1.7 Determination of V_o proliferation in etched LDH

EPR spectroscopy measurements were carried out to evaluate if the etching procedure promotes oxygen vacancies in the LDH structures. In this case, CuCr-LDH:2-D-40-a, 0,5E-CuCr-LDH:5-D-40-a, and 3,0E-CuCr-LDH:5-D-40-a were analyzed and compared as they are the most and least etched samples. In Figure 4.18, the EPR spectra are depicted.

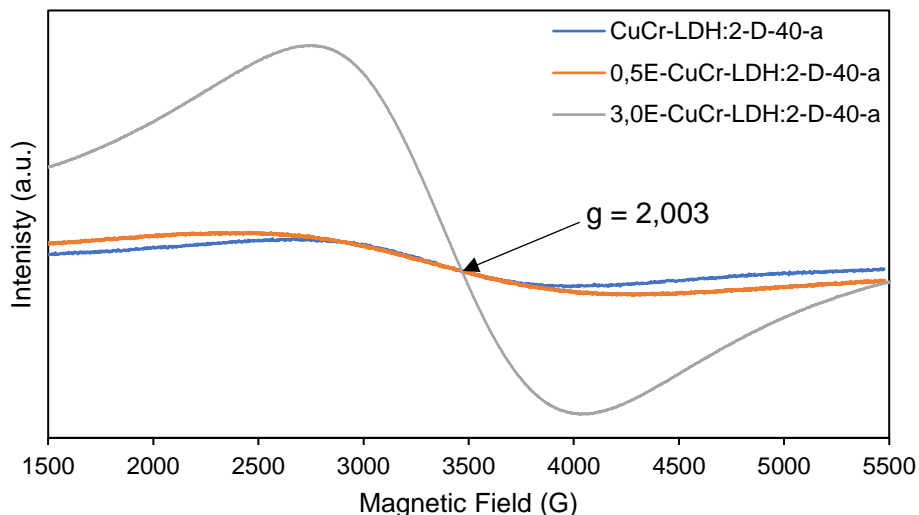


Figure 4.18 EPR spectra of CuCr-LDH:2-D-40-a, 0,5E-CuCr-LDH:5-D-40-a, and 3,0E-CuCr-LDH:5-D-40-a

As previously mentioned, the intensity of the EPR spectra is directly related to the number of free electrons present in a sample. These electrons are also indicative of the amount of V_O . Furthermore, the value of g , the electron g -factor, is equal to 2,003, indicating that this signal is due to the excitation of free electrons.

Figure 4.18 proves a direct correlation between the number of defects present in a material and the strength of the etching treatment. Permitting the establishment of an optimum etching state would maximize the photocatalyst's performance, as excessive etching can irreversibly destroy the LDH structure.

However, if the data is compared to other LDH EPR spectra available in the literature [46], the magnetic field obtained for these samples is much greater than expected for this kind of material. It is known that the presence of oxygen gas significantly alters the field. One possible explanation for these values is that since ideal vacuum conditions could not be reached, the excessive presence of oxygen inside the capillary would have affected the measurement.

4.2 Photocatalytic results

The different CuCr-LDH materials synthesized with varying divalent/trivalent cations ratios were tested to establish the optimum. CuCr-LDH:5-D-40-a was not tested due to the lack of evidence for that material to behave as a semiconductor (no bandgap energy). Similarly, the etched samples were also tested to analyze how the etching influence the performance of the catalysts. Finally, the ternary LDH materials were also tested, and the results obtained are reported.

In Figure 4.19, the results from testing CuCr-LDH:1-D-40a, CuCr-LDH:2-D-40a, CuCr-LDH:2-I-40a, and CuCr-LDH:3-D-40a are shown.

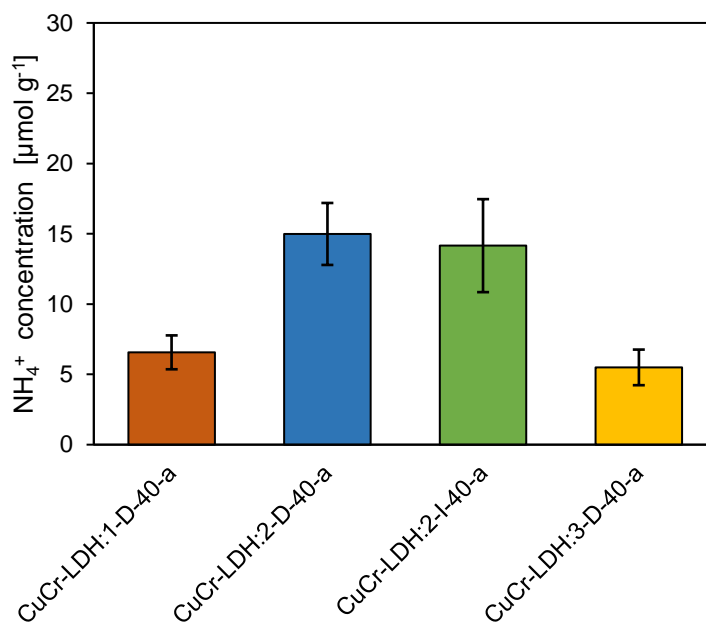


Figure 4.19 Photocatalytic activity results of the CuCr-LDH catalysts with different metal ratio

The best photocatalyst of this batch was the CuCr-LDH:2-D-40a, with an activity of 15,0 $\mu\text{mol g}^{-1}$. CuCr-LDH:2-I-40a results are not much more inferior, 14,2 $\mu\text{mol g}^{-1}$, to the CuCr-LDH:2-D-40a. Similar results were obtained for CuCr-LDH:2-D-40a different repeats of the experiments (up to 5 for each catalyst). In contrast, CuCr-LDH:2-I-40a results show a more significant deviation, meaning that instant addition synthesis causes a more heterogeneous batch. However, this difference can be within the experimental error. Nonetheless, during the instant addition synthesis of CuCr-LDH:2-I-40a, large clumps of solid material (precipitated) were formed when the two solutions were initially mixed. It is not until after stirring inside the flask that these clumps are diffused completely, which means that some of the material is formed at an initial stage (with higher pH), while the rest is formed afterward when the pH is lower, making the batch more heterogeneous.

For CuCr-LDH:1-D-40a, the performance is relatively less than CuCr-LDH:2-D-40a, 6,6 $\mu\text{mol g}^{-1}$. For CuCr-LDH:3-D-40a, a similar result is obtained, 5,5 $\mu\text{mol g}^{-1}$. In this case, it could be because a much lower bandgap can cause more recombination of electron-hole pairs and make these catalysts less efficient. Additionally, for CuCr-LDH:3-D-40a, it is known that there are other phases present that could be completely inactive during the reaction and even block access to actual active sites on the particles.

In Figure 4.19, the results for the photocatalytic testing of the CuCr-LDH etched samples (0,5E- CuCr-LDH:2-D-40-a, 1,0E- CuCr-LDH:2-D-40-a, 2,0E- CuCr-LDH:2-D-40-a, and 3,0E- CuCr-LDH:2-D-40-a) and the original batch, CuCr-LDH:2-D-40-a from which they were synthesized, are presented.

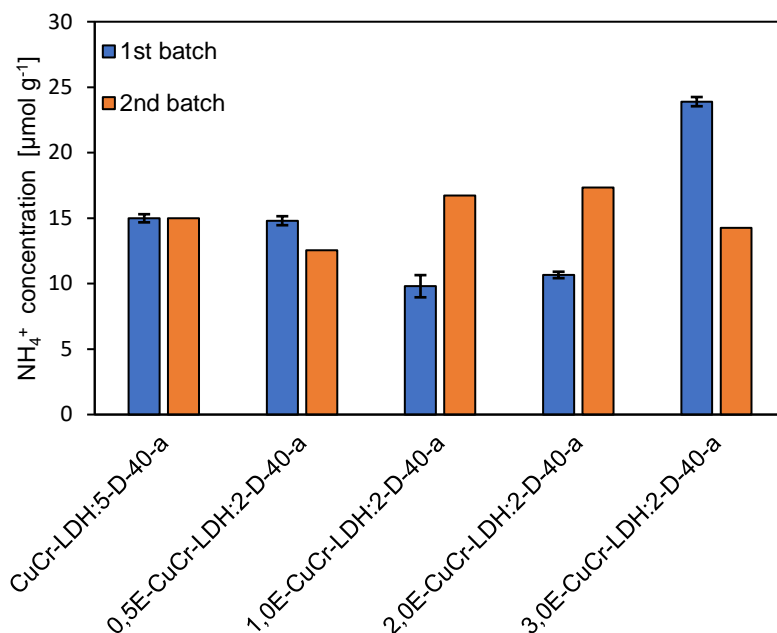


Figure 4.20 Photocatalytic activity results of the etched CuCr-LDH catalysts

From the same batch of CuCr-LDH:2-D-40-a, two sets of etched samples were synthesized. Initially, only one was made, but a second batch was also produced later in the project since the results were not conclusive. ‘It is speculated that having used different glassware and magnetic stirrer, due to availability, might have lead to reproducibility errors between the batches. Additionally, only one experiment was conducted for each sample of the second batch, so standard deviation was not obtained.

For these samples, it is also believed that mainly two factors influence their performance: partcile size and bandgap energy. The bandgap energy of these samples is inferior to the initial CuCr-LDH:2-D-40-a; nonetheless, for 1,0E-CuCr-LDH:2-D-40-a, 2,0E-CuCr-LDH:2-D-40-a, and 3,0E-CuCr-LDH:2-D-40-a, the particle size is smaller than in CuCr-LDH:2-D-40-a. These explain the more significant variations between the three more etched samples and the seeming stability of 0,5E-CuCr-LDH:2-D-40-a results, which has no significant difference in agglomerate size CuCr-LDH:2-D-40-a. Still, those have much lower bandgap energy.

Additionally, the results obtained from the element detection suggest that both 1,0E-CuCr-LDH:2-D-40-a and 2,0E-CuCr-LDH:2-D-40-a have a different metal cation ratio than 2.

In both cases, there is a higher Cu presence. The results of the photocatalytic test with CuCr-LDH species with different ratios indicate that a higher Cu presence negatively affects the photocatalytic activity.

In the best-case scenario, 3,0E-CuCr-LDH:2-D-40-a of the first batch, compared to CuCr-LDH:2-D-40-a, there is a significant 59,3% increase in the photocatalytic activity. Therefore, the fine-tuning of the procedure for LDH etching should be pursued to guarantee a substantial increment in the activity of the different batches.

A downside of the etching procedure is that there is a significant loss of catalyst mass. Although this method is used in the literature as an effective tool to increase the performance of a photocatalyst, this phenomenon has not been previously reported. As an example, in Table 4.4, the change of catalyst mass after etching is shown. For these experiments, the initial mass used was 300 mg.

Table 4.4 Obtained mass of catalyst after etching treatment

Sample	1 st batch (mg)	2 nd batch (mg)
0,5E-CuCr-LDH:2-D-40-a	291,4	293,3
1,0E-CuCr-LDH:2-D-40-a	209,6	203,5
2,0E-CuCr-LDH:2-D-40-a	147,3	150,8
3,0E-CuCr-LDH:2-D-40-a	61,9	94,4

In Figure 4.20, activity results for testing the ternary LDH and the CuCr-LDH equivalent species (CoCuCr-LDH:2-D-30-a, CuNiCr-LDH:2-D-30-a, and CuCr-LDH:2-D-30-a) are presented. CuCrFe-LDH:2-D-30-a and CuCrFe-LDH:2-D-30-b were not tested as they did not show semiconductor behavior, necessarily to work as a photocatalyst.

As mentioned in the Material and Methods Chapter, the amount of solution added was reduced as the autoclave liner should not be loaded entirely. During the coprecipitation step, a higher amount of humidity was absorbed, increasing the total volume since both Co and Ni nitrates are more hydrated than the Cu nitrate.

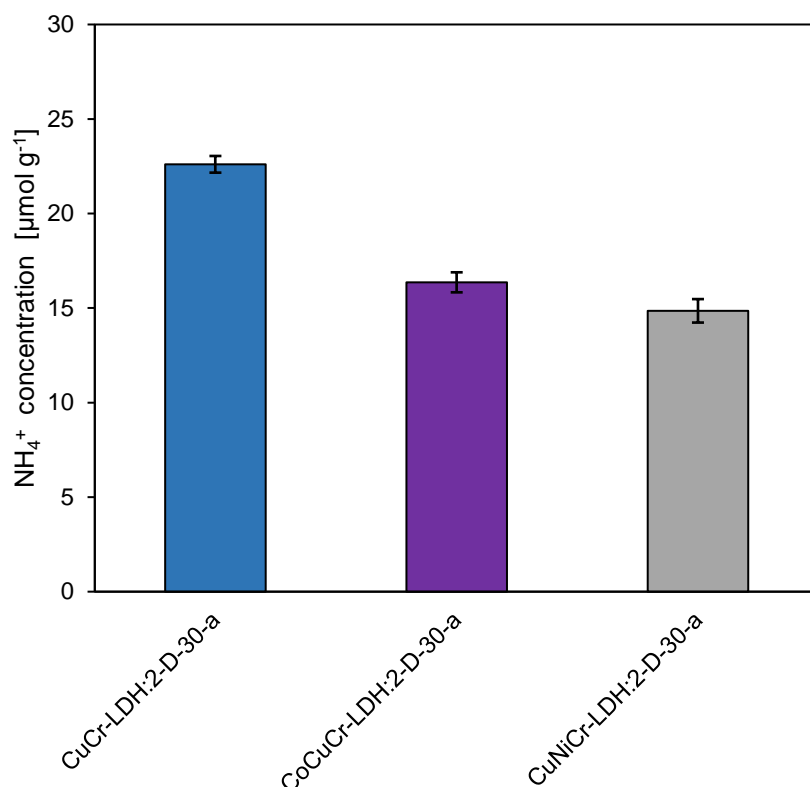


Figure 4.21 Photocatalytic activity results of the ternary CuCr-LDH catalysts

The performance of the ternary LDH is not superior to the CuCr-LDH:2-D-30-a. This was not the expected result. Although, several factors could explain this outcome. Firstly, the ternary-LDH have a larger particle size, and during the SEM imaging, they tend to agglomerate together. Furthermore, the photoluminescence analysis reports that CuNiCr-LDH:2-D-30-a has a much higher recombination rate, making it the less efficient photocatalyst. In the case of CoCuCr-LDH:2-D-30-a, it has less than CuCr-LDH:2-D-30-a. Still, another explanation for both would be replacing Cu cations for Ni or Co reduces the beforementioned Jahn Teller distortions, which contributed to the accessibility of adsorbed species to the photocatalyst.

4.3 Challenges

A relevant question with the photocatalytic tests performed was that by using a colorimetric detection technique, it is not possible to discern if other compounds than ammonia were synthesized or present in the reaction solution.

Furthermore, in Figure 4.21, the results for ammonium ions detection when using the CuCr-LDH:2-D-30-a was compared to experiments with the same catalyst were instead of nitrogen, argon was injected in the reactor, and the lamp was not used either.

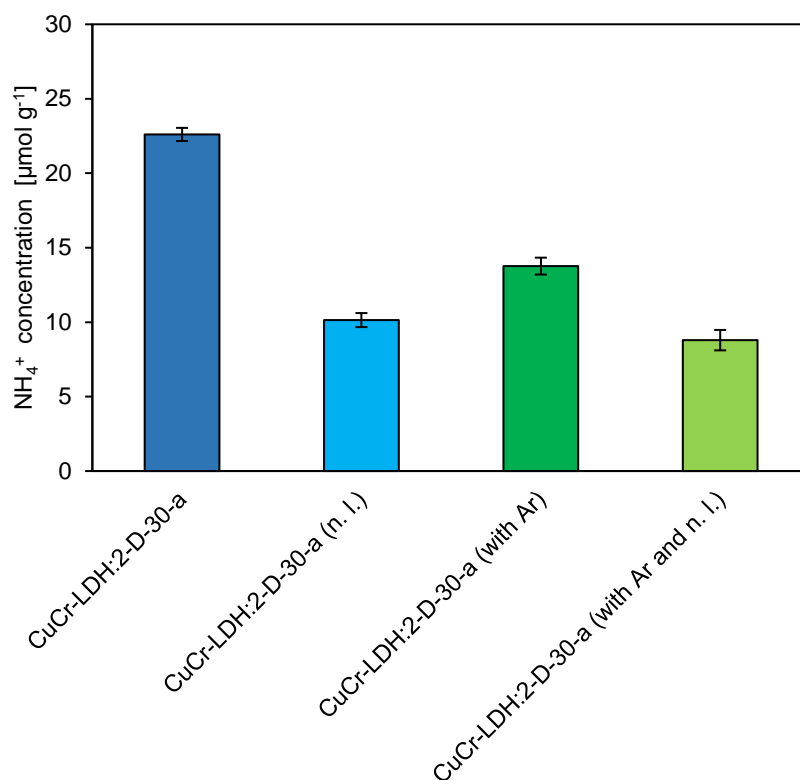


Figure 4.22

Figure 4.23 Photocatalytic activity results of CuCr-LDH:2-D-30-a under normal experimental conditions, with no light (n.l.), with Ar, and with Ar and no light

The experiments without light and without N₂ should, ideally, should give no yield at all. A plausible source for the non-photocatalytic ammonia, which has been reported in the literature, is the DI water itself. It is reported that up to 52 µg L⁻¹ of ammonia which equals to 3,05 µM L⁻¹ can be found in stale DI water [20].

Another issue with these experiments is that is completely impossible to avoid some photocatalytic activity even if Ar is only used during the experiments it is impossible to completely remove all N₂, since both the catalyst and the DI water had been previously exposed to the atmosphere. Similarly, during preparation is impossible to keep the reactor completely in the dark.

All these issues create uncertainty regarding the results obtained and difficult the reproducibility of the results.

Additionally, some of the techniques utilized in this project had not been used before for this topic and application. This meant that a considerable amount of time was spent

obtaining and preparing the necessary equipment to characterize the materials studied in this project.

5 Conclusions

This thesis aimed to synthesize and modify CuCr-LDH based material to improve its photocatalytic performance for the nitrogen fixation to produce ammonia under visible light. The synthesized catalysts were characterized with specific emphasis on their morphology (crystallinity, phase purity, elemental composition, and bonding structure) and photocatalytic properties (absorbance, bandgap energy, and photoluminescence).

The catalysts were synthesized through coprecipitation and hydrothermal synthesis; this method successfully obtained the desired crystalline structure. Furthermore, a broad spectrum of LDH-type materials can be produced due to its tunability and simplicity.

Five CuCr-LDH catalysts with a different Cu:Cr ratio were synthesized, CuCr-LDH:1-D-40-a, CuCr-LDH:2-D-40-a, CuCr-LDH:2-I-40-a, CuCr-LDH:3-D-40-a, and CuCr-LDH:5-D-40-a. The best material was CuCr-LDH:2-D-40-a, which had the highest photocatalytic activity (15,0 $\mu\text{mol NH}_4^+$ per gram of catalyst). From these materials, only CuCr-LDH:3-D-40-a and CuCr-LDH:5-D-40-a are suspected not to be pure LDH and had additional impurity phases, mainly Cu species (CuOHNO_3 and $\text{Cu}(\text{OH})_2$) since the Cu loading was excessive to maintain a stable structure. CuCr-LDH:5-D-40-a was the only species that did not have semiconductor properties (no bandgap energy). Therefore, from these results, the optimum metal ratio was considered to be two.

Alkali etching treatment was implemented to CuCr-LDH:2-D-40-a. In total, four etched samples were synthesized 0,5E-CuCr-LDH:2-D-40-a, 1,0E-CuCr-LDH:2-D-40-a, 2,0E-CuCr-LDH:2-D-40-a, and 3,0E-CuCr-LDH:2-D-40-a. On the one hand, alkali etching maintained the LDH structure and significantly reduced their particle size and bandgap energy. On the other hand, for 1,0E-CuCr-LDH:2-D-40-a and 2,0E-CuCr-LDH:2-D-40-a, it did alter the original material's Cu:Cr ratio. Only 3,0E-CuCr-LDH:2-D-40-a outperformed the original CuCr-LDH:2-D-40-a activity by 59,3% (23,9 $\mu\text{mol NH}_4^+$ per gram of catalyst). It is believed that greater tuning of this technique is necessary to guarantee stable, improved results.

Ternary LDH were synthesized for comparison to study the effect of the addition of a third metal cation on the photocatalytic activity of the LDH. In this work, CoCuCr-LDH, CuNiCr-LDH, and CuCrFe-LDH were synthesized, maintaining a divalent to trivalent cation ratio of two. CoCuCr-LDH:2-D-30-a and CuNiCr-LDH:2-D-30-a were successfully synthesized. However, CuCrFe-LDH was not successfully synthesized; the literature suggests

Fe is a prompt to phase out of the LDH structure unless high supersaturation conditions are achieved. A CuCr-LDH:2-D-30-a batch was also synthesized to evaluate the ternary LDH activity. The best activity was observed in CuCr-LDH:2-D-30-a, 22,6 $\mu\text{mol NH}_4^+$ per gram of catalyst, surpassing both ternary LDH by 37,8% and 54,8%, respectively. Unfortunately, the characterization of these materials contemplates that a larger particle size and not a significant reduction of the bandgap energy might be the cause.

Overall, CuCr-LDH is considered a viable photocatalyst for nitrogen fixation. Furthermore, the optimum metal ratio between divalent and trivalent cations was established to be two. Alkali etching was found to improve the photocatalytic performance of LDH, and it has shown some promising results.

6 Further work

To better understand the properties of the catalysts synthesized in this work, more characterization techniques should be carried out. In this case, techniques like N₂ physisorption and chemisorption could be of great use to determine key properties like metal dispersion and surface area and shed light on how the synthesis may affect the final product's morphology.

Another vital topic for further study is establishing a more reliable procedure for the alkali etching treatment. There were some reproducibility issues between the different batches of etched LDH materials obtain during this project.

Finally, both the specialization project and this Master's thesis have focused on studying, analyzing, and modifying the photocatalysts used for the nitrogen fixation reaction. It would be of great interest to also examine how the reaction conditions affect the photocatalyst performance and could be modified to improve the product yield of the reaction.

References

- [1] W. Steffen *et al.*, "Global Change and the Earth System," 2004.
- [2] J. Arias, "On the Origin of Saltpeter, Northern Chile Coast.," 2003.
- [3] H. Liu, *Ammonia Synthesis Catalysts: Innovation And Practice* (Chemical Industry Press). China: World Scientific - Chemical Industry Press, 2013.
- [4] "U.S. Geological Survey 2017 Mineral Commodity Summary."
<https://minerals.usgs.gov/minerals/pubs/commodity/nitrogen/mcs-2018-nitro.pdf>.
(accessed 18/10/2020).
- [5] J. R. Venkat Pattabathula. "Introduction to Ammonia Production." AIChE. (accessed 19/10/2020).
- [6] Spatzal *et al.*, "Evidence for interstitial carbon in nitrogenase FeMo cofactor," *Science*, vol. 334, 2011.
- [7] E. Zeiger, L. Taiz, *Plant Physiology, 4th Edition*. Wiley, 2008.
- [8] J. W. Niemantsverdriet, I. Chorkendor, *Concepts of modern catalysis and kinetics. Third Edition*. Denmark: Wiley-VCH, 2003.
- [9] J. L. White *et al.*, "Light-Driven Heterogeneous Reduction of Carbon Dioxide: Photocatalysts and Photoelectrodes," *Chemical Reviews*, 2015.
- [10] M. Quirck, J. Serda, *Characteristics of semiconductor materials* (Semiconductor manufacturing technology). New Jersey, USA: Upper Saddle River, 2001.
- [11] C. Kittel, *Introduction to Solid State Physics*. Wiley, 2005.
- [12] S. K. Banerjee, B. G. Streetman, *Solid state electronic devices*. Boston, USA: Pearson, 2016.
- [13] J. M. Coronado *et al.* *Design of Advanced Photocatalytic Materials for Energy and Environmental Applications*. London: Springer, 2013.
- [14] A. Fujishima, K. Honda, "Electrochemical Photolysis of Water at a Semiconductor Electrode," *Nature* no. 238 (5358), pp. 37–38, 1972.
- [15] H. Yu, *Chapter 2: Fundamentals of Sunlight Materials Interactions* (Green Photoactive Nanomaterials: Sustainable Energy and Environmental Remediation). The Royal Society of Chemistry, 2016.
- [16] J. M. N. Herrmann., " Photocatalysis fundamentals revisited to avoid several misconceptions " *Applied Catalysis B: Environmental* no. 99.3-4, pp. 461-468, 2010.

- [17] X. Meng, Z. Zhang, "Bismuth-based photocatalytic semiconductors: Introduction, challenges and possible approaches " *Journal of Molecular Catalysis A: Chemical*, 423, pp. 533-549.
- [18] H. Hirakawa et al., "Photocatalytic Conversion of Nitrogen to Ammonia with Water on Surface Oxygen Vacancies of Titanium Dioxide " *Journal of the American Chemical Society* no. 139.31, pp. 10929-10936, 2017.
- [19] A. J. Medford, M. C. Hatzell, "Photon-Driven Nitrogen Fixation: Current Progress, Thermodynamic Considerations, and Future Outlook " *ACS Catalysis*, no. 7.4 pp. 2624-2643, 2017.
- [20] Zhao et al., "Photocatalytic fixation of nitrogen to ammonia: state-of-the-art advancements and futureprospects," *Materials Horizons*, no. 5, pp. 1-20, 2018.
- [21] M. W. Jing He, Bo Li, Yu Kang, David G Evans, Xue Duan, "Preparation of Layered Double Hydroxides," in *Layered Double Hydroxides*. Berlin, Germany: Springer-Verlag 2005.
- [22] R. C. T. Slade, David G. Evan, "Structural Aspects of Layered Double Hydroxides," *Structure and Bonding* vol. 119, pp. 1-87, 2006.
- [23] R. C. T. Slade, David G. Evan, "Structural Aspects of Layered Double Hydroxides," in *Layered Double Hydroxides*. Berlin, Germany: Springer-Verlag 2005, pp. 1-87.
- [24] M. Ogawa, et al. , "Preparation of Layered Double Hydroxides toward Precisely Designed Hierarchical Organization " *ChemEngineering*, no. 3(3), 68, 2019.
- [25] Zhang et al., "Layered-Double-Hydroxide Nanosheets as Efficient Visible-Light-Driven Photocatalysts for Dinitrogen Fixation," *Advanced Materials*, no. 29, 2017.
- [26] L. Q. Zhiyi Lu, Yang Tian, Yaping Li, Xiaoming Sun and Xue Duan, "Ternary NiFeMn layered double hydroxides as highly-efficient oxygen evolution catalysts," *Chem. Commun.*, vol. 52, p. 908, 2015.
- [27] Z. L. Li Qian , Tianhao Xu , Xiaochao Wu , Yang Tian , Yaping Li , Ziyang Huo , Xiaoming Sun , and Xue Duan, "Trinary Layered Double Hydroxides as High-Performance Bifunctional Materials for Oxygen Electrocatalysis," *Adv. Energy Mater.*, vol. 5, no. 1500245, 2015.
- [28] Mock et al., "Putting chromium on the map for N₂ reduction: production of hydrazine and ammonia. A study of cis-M(N₂)₂ (M = Cr, Mo, W) bis(diphosphine) complexes," *Chemical Communications*, no. 60, 2016.

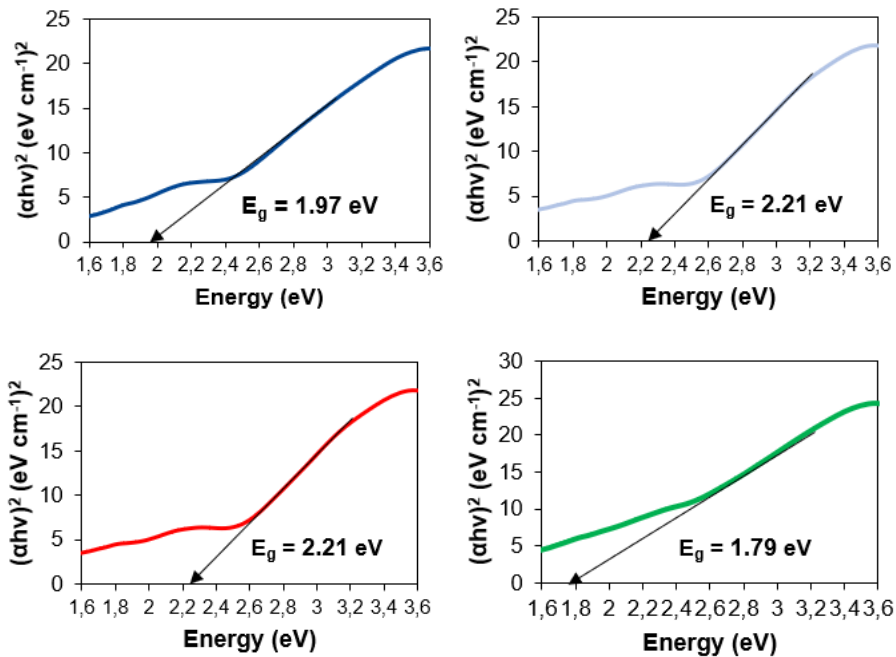
- [29] K. P. de Jong, *Synthesis of Solid Catalysts* Wiley-VCH 2009.
- [30] M. McMahon. "What Is Coprecipitation?" (accessed 17/11/2020).
- [31] J. C. H. Spence, *Experimental high-resolution electron microscopy*. New York, USA: Oxford University Press, 1988.
- [32] Annelise Kopp Alves, Carlos P. Bergmann and Felipe Amorim Berutti., *Hydrothermal Synthesis*, (Novel Synthesis and Characterization of Nanostructured Materials). Berlin: Springer Berlin Heidelberg, 2013.
- [33] J. W. Mullin, *Crystallization (Fourth Edition)*. Oxford, UK: Butterworth-Heinemann 2001.
- [34] L. Z. Yunxuan Zhao, Run Shi, Shuai Zhang, Xuanang Bian, Fan Wu, Xingzhong Cao, Geoffrey I. N. Waterhouse, and Tierui Zhang, "Alkali Etching of Layered Double Hydroxide Nanosheets for Enhanced Photocatalytic N₂ Reduction to NH₃," *Adv. Energy Mater.*, vol. 10, no. 2002199, 2020.
- [35] J. Goldstein, *Scanning Electron Microscopy and X-Ray Microanalysis*. Springer, 2003.
- [36] C. Gillet. "Subcellular localization of metal pools determined by TEM-EDS in embryo Arabidopsis thaliana mutants." <http://emc-proceedings.com/abstract/subcellular-localization-of-metal-pools-determined-by-tem-eds-in-embryo-arabidopsis-thaliana-mutants/> (accessed 12/04/2021).
- [37] D. A. H. Skoog, F. James; Crouch, Stanley R. *Principles of Instrumental Analysis (6th ed.)*. Belmont, CA: Thomson Brooks/Cole, 2007.
- [38] G. Kortüm, *Reflectance spectroscopy Principles, methods, applications*. Berlin Springer, 1969.
- [39] "Diffuse Reflectance Measurement." SHIMADZU. (accessed 17/11/2020).
- [40] The University of Colorado Boulder.
<https://www.orgchemboulder.com/Labs/Handbook/UV-Vis.pdf> (accessed 22/05/2021).
- [41] "Using the Fluorolog™-3 Luminescence Spectroscopy "
<http://faculty.sdmiramar.edu/fgarces/LabMatters/Instruments/FluoroSpex/Fluorimeter-Operations/index.html> (accessed 24/05/2021).
- [42] E. Moore, *Fourier transform infrared spectroscopy (FTIR): Methods, analysis and research insights* 2016, pp. 10-129.

- [43] R. Rahman. "Optical diagram of a Michelson interferometer in FTIR." John Wiley and Sons. https://www.researchgate.net/figure/Optical-diagram-of-a-Michelson-interferometer-in-FTIR-Reprinted-with-permission-from-1_fig3_332411127 (accessed 06/06/2021).
- [44] Krishnavedala, S. o. e. s. states, Ed., ed. Commons, the free media repository, 2015.
- [45] C. E. Chechik V, Murphy D, *Electron Paramagnetic Resonance*. New York, NY: OUP Oxford, 14/07/2016.
- [46] Y. Y. He Wang, Jiali Gu, Zhichao Jia, Zhansheng Lu, Zhengyu Bai, Lin Yang, Xiaoli Yang, "Facile one-pot synthesis of layered double hydroxides nanosheets with oxygen vacancies grown on carbon nanotubes for efficient oxygen evolution reaction," *Journal of Power Sources*, vol. 467, 228354, 2020.
- [47] J. S. Bagi et al., "Nanocrystalline copper-chromium-layered double hydroxide with tunable interlayer anions for electrochemical capacitor application," *Synthetic Metals*, vol. 264, 116371, 2020.
- [48] G. V. Szilveszter Ziegenheim, Márton Szabados, Pál Sipos, and István Pálinkó, "Cu(II)Cr(III)-LDH: synthesis, characterization, intercalation properties and a catalytic application," *Chemical Papers* no. 72 pp. 897–902, 2018.
- [49] M. R. O. Riyanto, "Electrosynthesis and Characterization of Cu(OH)₂ Nanoparticle using Cu and Cu-PVC Electrodes in Alkaline Solution," *Int. J. Electrochem. Sci.*, vol. 10, pp. 4911 - 4921, 2015.
- [50] M. W. Jing He, Bo Li, Yu Kang, David G Evans, Xue Duan "Preparation of Layered Double Hydroxides," in *Layered Double Hydroxides*, (Structure and Bonding: Springer, 2005, pp. 89-119.
- [51] Y. Waseda et al., "Inhibition of Conversion Process from Fe(OH)₃ to β -FeOOH and α -Fe₂O₃ by the Addition of Silicate Ions," *ISIJ International*, vol. 45, pp. 77–81, 2005.
- [52] F. Xu et al., "Crystallinity control on photocatalysis and photoluminescence of TiO₂-based nanoparticles," *Journal of Alloys and Compounds*, vol. 496, pp. 234-240, 2010.
- [53] K. p. Snehaprava Das, "Superior photocatalytic performance of Co Al LDH in the race of metal incorporated LDH: A comparison study," *Materials Today: Proceedings*, vol. 35, pp. 275-280, 2021.
- [54] W. G. H. Shuai Sun, "The photoluminescence of Co-Al-layered double hydroxide," *Chinese Chemical Letters*, vol. 18, pp. 371–1373, 2007.

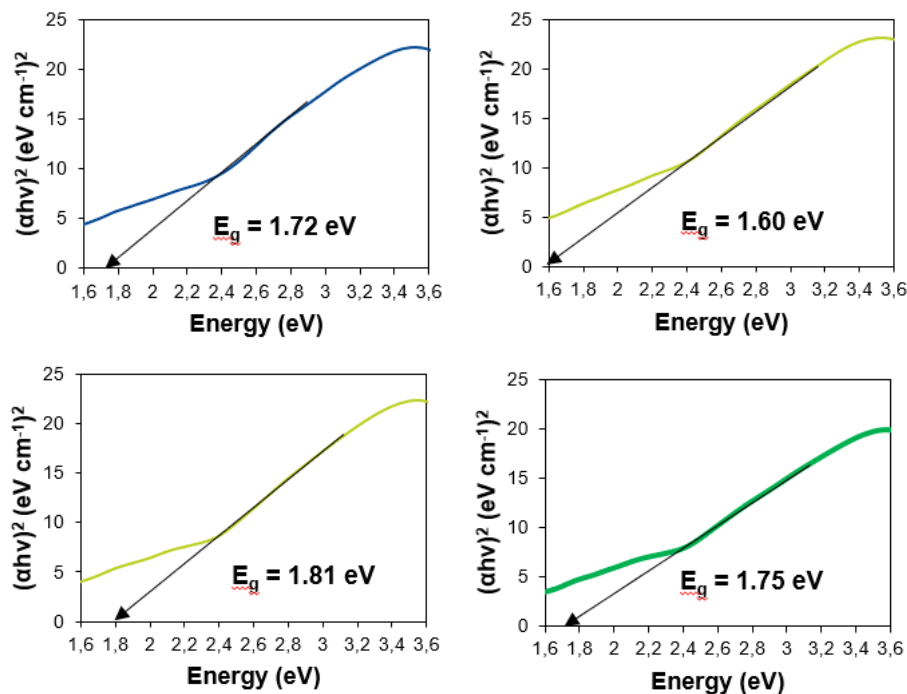
- [55] F. Long et al., "Facile synthesis of few-layer MoS₂ in MgAl-LDH layers for enhanced visible-light photocatalytic activity," *RSC Advances*, vol. 9, no. 24280, 2019.

Appendix A – Tauc plots

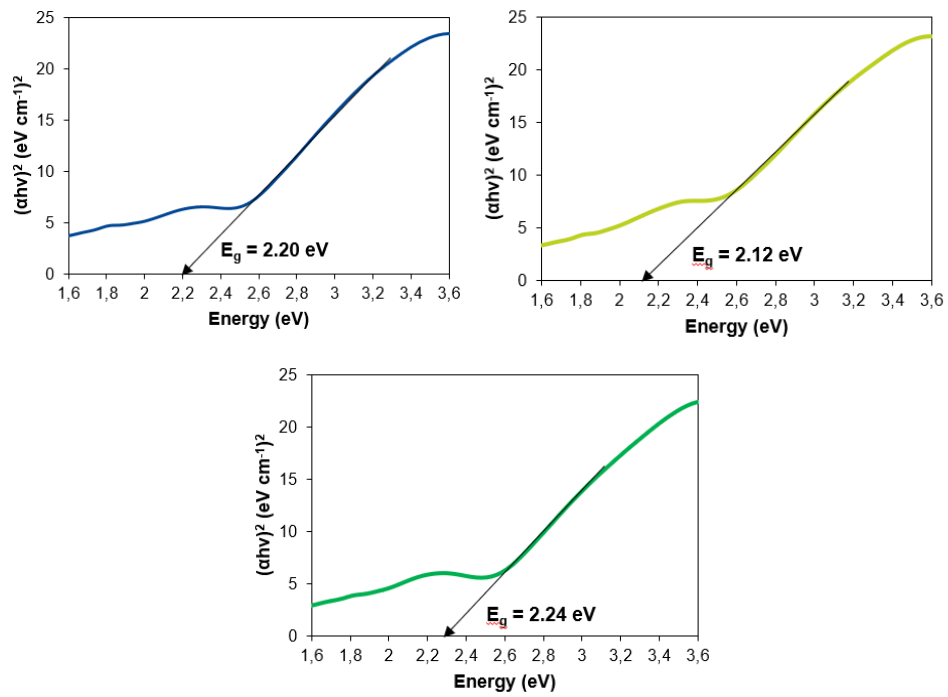
Tauc plot for bangap energy estimation



From top left to bottom right: CuCr-LDH:1-D-40-a, CuCr-LDH:2-D-40-a, CuCr-LDH:2-I-40-a, and CuCr-LDH:3-D-40-a

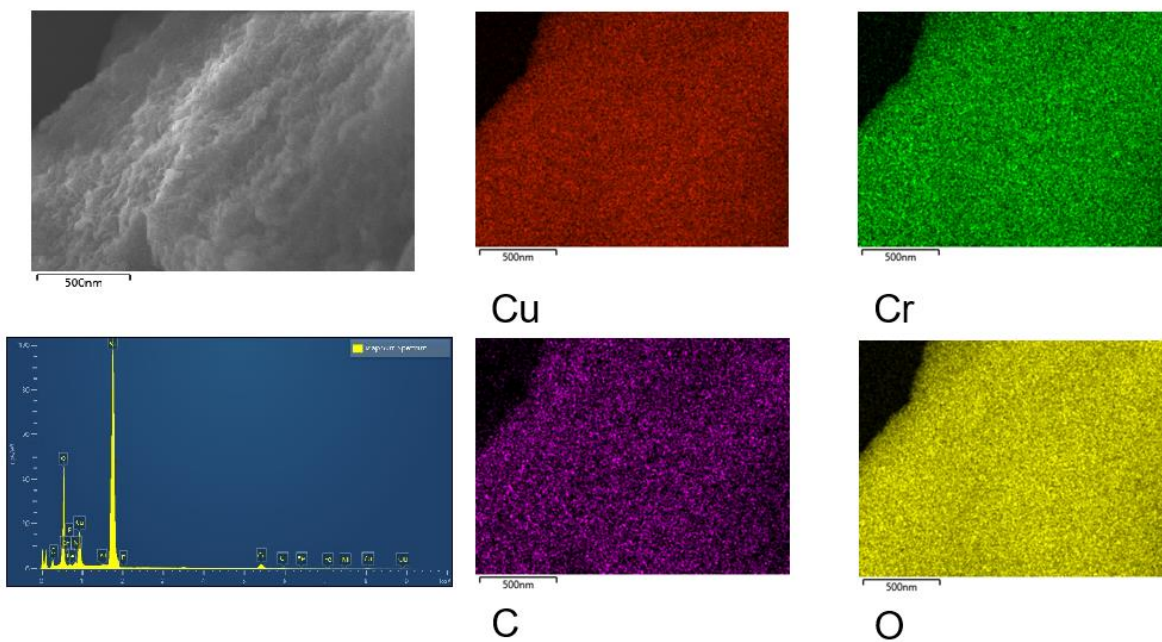


From top left to bottom right: 0,5E-CuCr-LDH:2-D-40-a, 1,0E-CuCr-LDH:2-D-40-a, 2,0E-CuCr-LDH:2-D-40-a, and 3,0E-CuCr-LDH:2-D-40-a

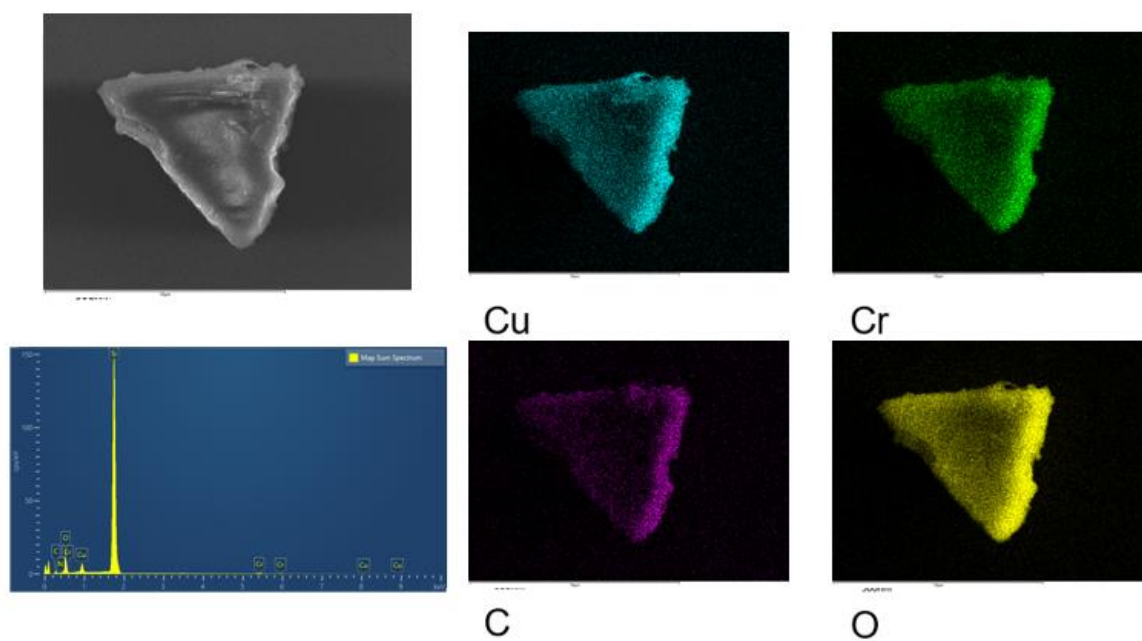


From top left to bottom: CuCr-LDH:2-D-30-a, CoCuCr-LDH:2-D-40-a, and CuNiCr-LDH:2-D-30-a

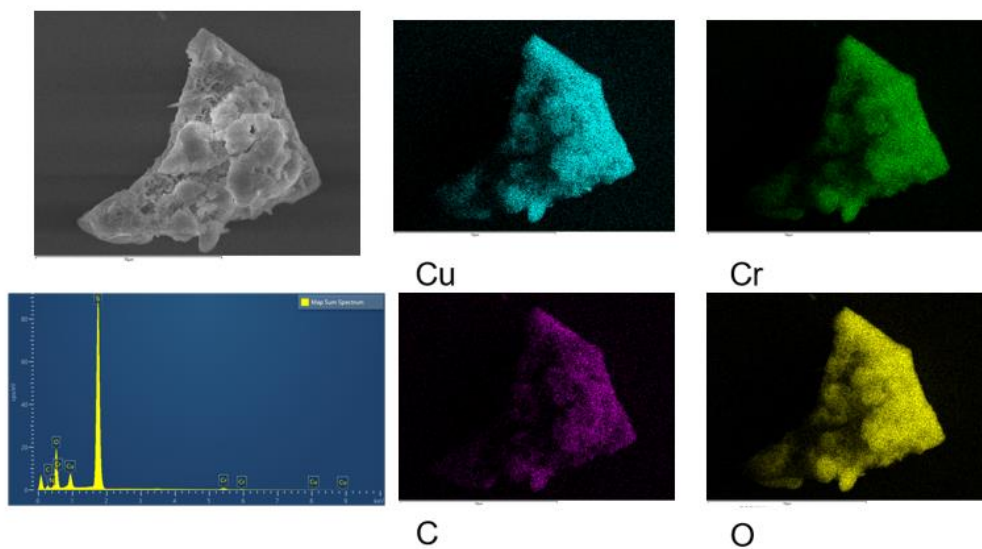
Appendix B - EDX mapping



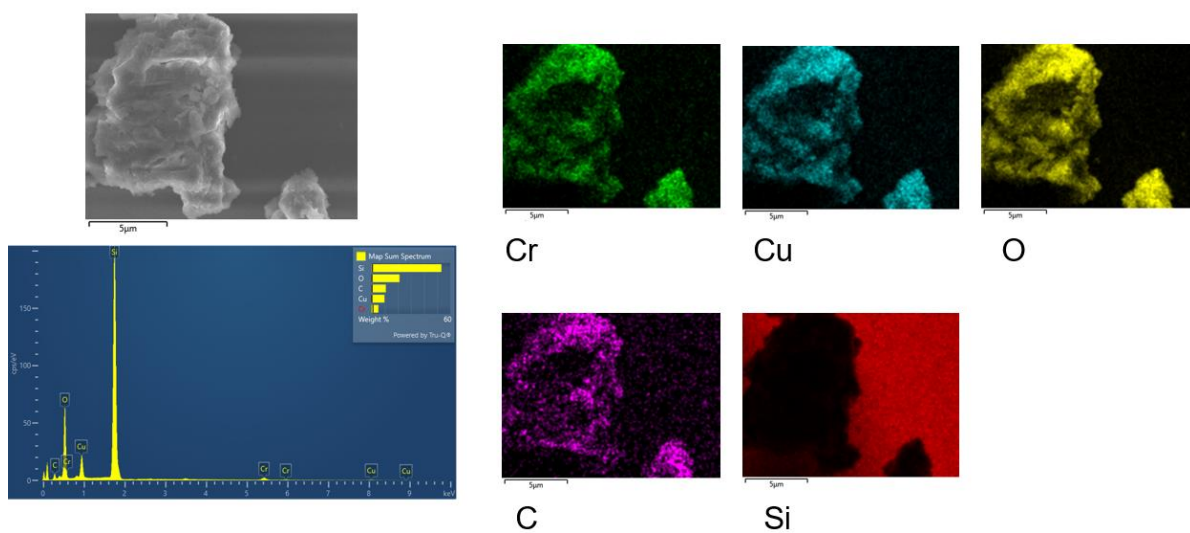
EDX mapping of 0,5E-CuCr-LDH:2-D-40-a



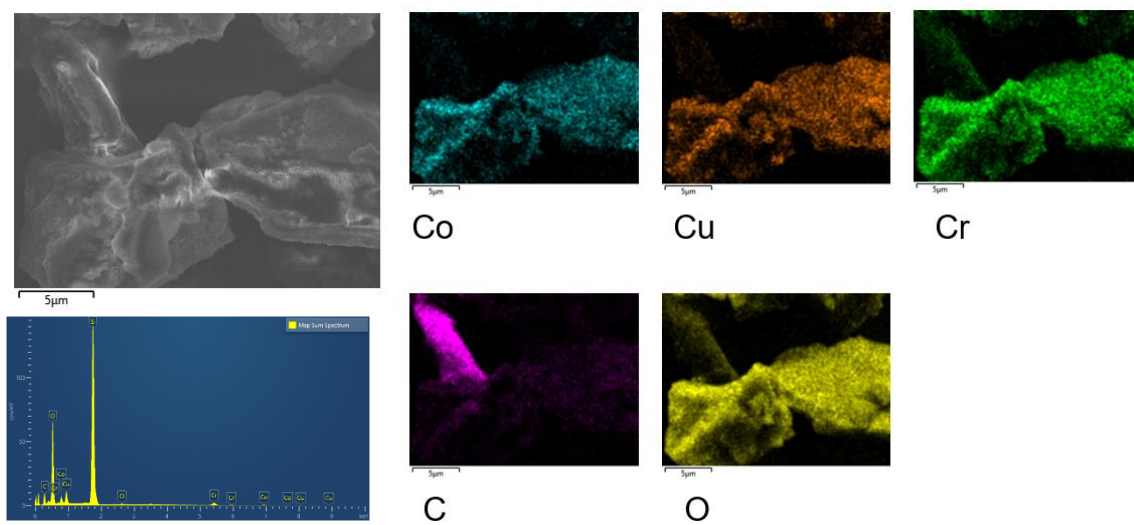
EDX mapping of 1,0E-CuCr-LDH:2-D-40-a



EDX mapping of 2,0E-CuCr-LDH:2-D-40-a

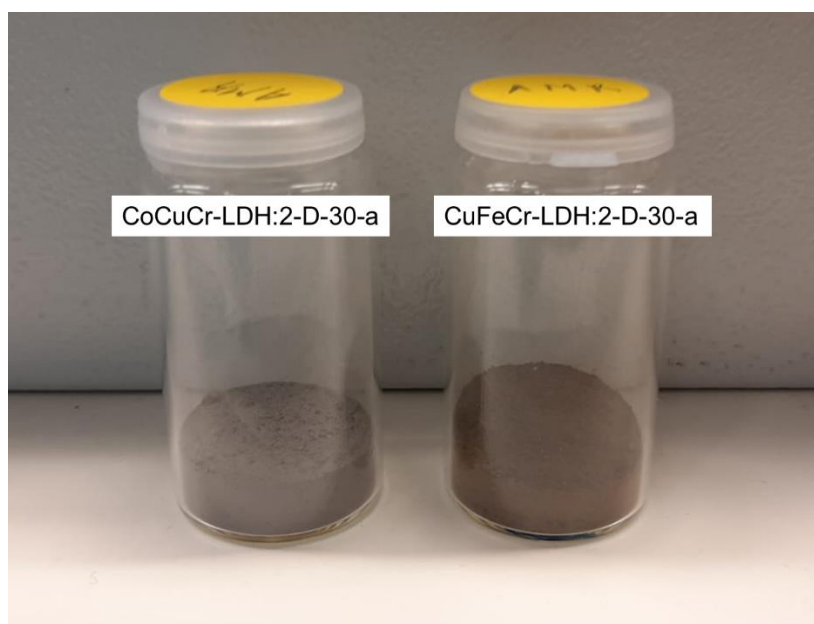
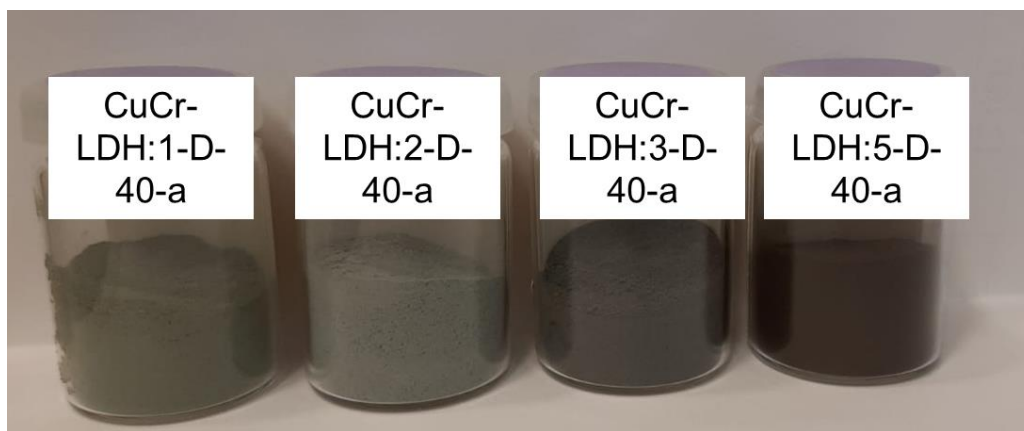


EDX mapping of CuCr-LDH:2-D-30-a



EDX mapping of CoCuCr-LDH:2-D-30-a

Appendix C – Pictures of samples



Appendix D – Risk Assessment



ID	40052	Status	Date
Risk Area	Risikovurdering: Helse, miljø og sikkerhet (HMS)	Created	04.09.2020
Created by	Albert Miró i Rovira	Assessment started	04.09.2020
Responsible	Albert Miró i Rovira	Measures decided	
		Closed	

Risk Assessment:**CAT, Master student, 2020, Albert Miró i Rovira****Valid from-to date:**

9/4/2020 - 9/4/2023

Location:

IKP, Kjemiblokk 5, Gløshaugen Campus

Goal / purpose

This risk assessment contains all activities that I will be performing in different laboratories during my Master Thesis. I would initially start with the synthesis and characterization of CuCr materials, with the aim of using them as photo-catalysts in ammonia synthesis. The risk assessment would be updated at a later stage when I look into other materials.

Background

The CuCr nanoparticles are expected to work as photo-catalysts in the ammonia synthesis. A N₂ reduction to ammonia by solar light represents a green and sustainable ammonia synthesis approach which help reduce the energy consumption compared to the standard Haber-Bosch process. It will also eliminate the emission of CO₂ compared to today's process by avoiding the use of natural gas.

Chemicals that will be used: Copper(II) nitrate hydrate, Chromium(III) nitrate nonahydrate and sodium hydroxide. (this list may be expanded further. If that were the case, new risk analysis must be done and approved before experiments with new chemicals can begin)

Equipment and instruments that will be used: Solar Simulator (ScienceTech SF-300-A), centrifuge, vacuum oven, sonication bath, autoclaves, freeze dryer.

Description and limitations

The risk assessment is limited to the lab work involving risk, which means the synthesis of the particles, the powder characterization by using techniques such as XRD, SEM, EDX, UV-Vis, UV-Vis DRS, etc. and catalytic tests that will be performed in the laboratories of the Catalysis Group, using a photocatalytic set-up and a solar simulator.

The synthesis of CuCr nano-sheets is achieved by a co-precipitation mixing two solutions (A and B). A is an aqueous solution containing Copper(II) nitrate hydrate and Chromium(III) nitrate nonahydrate dissolved in deionized water. Solution B consist of NaOH dissolved in deionized water with a concentration of 3 M. Solution A and B are simultaneously added in a mill (2000rpm). The resulting slurry is then transferred to an autoclave and heated to 120°C for 12h. Afterwards the solid products are collected by centrifugation. Then they are washed with deionized water for several times and finally are dried at 60°C under vacuum for 24h.

Safety measures related to spread of COVID-19 infection:

- Will avoid touching face while working in the lab
- Disinfection before and after with ethanol on all surfaces that I'll be in contact with (door knob – card reader with code panel. This would also apply to laboratory PC screen, keyboard, mouse, desk and the label printing machine.
- Will ensure 2m distance from colleagues
- Usage of nitrile gloves when touching shared lab set-ups and equipment
- Washing hands as often as possible

Prerequisites, assumptions and simplifications



The work assumes that proper training is given prior to the use of laboratories and equipment/instruments, to minimize the probability of user-caused mistakes. Safe storage and handling of samples between labs are crucial. Use of personal protective equipments are mandatory.

Also due to the current COVID pandemic extra measures have been implemented in the labs to avoid propagation of the illness

Attachments

Copper(II) nitrate hydrate MSDS.pdf
Chromium(III) nitrate nonahydrate MSDS.pdf
Sodium Hydroxide MSDS.pdf
K5_228_Solar Simulator_Jibin.doc
Flowsheet of the Photocatalysis setup.png
Chloroform MSDS.pdf
Phenol MSDS.pdf
Sodium nitroprusside MSDS.pdf
SWITCH OFF CONDITIONS.docx
Sodium hypochlorite MSDS.pdf
Iron(III) nitrate nonahydrate_SDS_NO.PDF
Cobalt(II) nitrate hexahydrate SDS_EN.pdf
Cobalt(II) nitrate hexahydrate SDS_NO.pdf
Nickel(II) nitrate hexahydrate SDS_NO.pdf
Nickel(II) nitrate hexahydrate SDS_EN.pdf
Iron(III) nitrate nonahydrate_SDS_EU.PDF

References

[Ingen registreringer]

Summary, result and final evaluation

The summary presents an overview of hazards and incidents, in addition to risk result for each consequence area.

Hazard: Preparation of CuCr-LDH, CuCrFe-LDH, CoCuCr-LDH and CuNiCr-LDH in lab K5-317

Incident: Exposure to Copper(II) nitrate hydrate

Consequence area:	Helse	Risk before measures:	Risiko after measures:	
	Ytre miljø	Risk before measures:	Risiko after measures:	
	Materielle verdier	Risk before measures:	Risiko after measures:	

Incident: Exposure to Sodium Hydroxide

Consequence area:	Helse	Risk before measures:	Risiko after measures:	
	Materielle verdier	Risk before measures:	Risiko after measures:	

Incident: Exposure to Chromium(III) nitrate nonahydrate

Consequence area:	Helse	Risk before measures:	Risiko after measures:	
	Ytre miljø	Risk before measures:	Risiko after measures:	
	Materielle verdier	Risk before measures:	Risiko after measures:	

Incident: Exposure to Iron (III) nitrate nonahydrate

Consequence area:	Helse	Risk before measures:	Risiko after measures:	
	Materielle verdier	Risk before measures:	Risiko after measures:	

Incident: Exposure to Cobalt (II) nitrate hydrate

Consequence area:	Helse	Risk before measures:	Risiko after measures:	
	Ytre miljø	Risk before measures:	Risiko after measures:	
	Materielle verdier	Risk before measures:	Risiko after measures:	

Hazard: Preparation of CuCr-LDH, CuCrFe-LDH, CoCuCr-LDH and CuNiCr-LDH in lab K5-317

Incident: Exposure to Nickel (II) nitrate hydrate

Consequence area:	Helse	Risk before measures:	Risiko after measures:	
	Ytre miljø	Risk before measures:	Risiko after measures:	
	Materielle verdier	Risk before measures:	Risiko after measures:	

Hazard: Working with Solar Simulator (ScienceTech SF-300-A)

Incident: Exposure to UV rays from the solar simulator

Consequence area:	Helse	Risk before measures:	Risiko after measures:	
--------------------------	-------	-----------------------	------------------------	--

Incident: Burns caused by touching the arc lamp envelope

Consequence area:	Helse	Risk before measures:	Risiko after measures:	
--------------------------	-------	-----------------------	------------------------	--

Hazard: Working in the lab during COVID pandemic

Incident: Risk due to touching the face while at work

Consequence area:	Helse	Risk before measures:	Risiko after measures:	
--------------------------	-------	-----------------------	------------------------	--

Incident: Risk due to close contact of colleagues

Consequence area:	Helse	Risk before measures:	Risiko after measures:	
--------------------------	-------	-----------------------	------------------------	--

Incident: Risk due to touching common objects

Consequence area:	Helse	Risk before measures:	Risiko after measures:	
--------------------------	-------	-----------------------	------------------------	--

Incident: Risk of getting infected by the public

Consequence area:	Helse	Risk before measures:	Risiko after measures:	
--------------------------	-------	-----------------------	------------------------	--



Hazard: Use of heating oven (K5-317)

Incident: Accidentally touching a hot surface on the furnace may cause burns

Consequence area: Helse Risk before measures:  Risiko after measures: 

Hazard: Waste disposal in general for the laboratories in K5

Incident: Incorrect waste handling

Consequence area: Helse Risk before measures:  Risiko after measures: 
Ytre miljø Risk before measures:  Risiko after measures: 
Materielle verdier Risk before measures:  Risiko after measures: 

Incident: Disposal of Hg containing wastes

Consequence area: Helse Risk before measures:  Risiko after measures: 
Ytre miljø Risk before measures:  Risiko after measures: 
Materielle verdier Risk before measures:  Risiko after measures: 

Hazard: Detection of ammonium ions using indophenol blue method

Incident: Exposure to phenol

Consequence area: Helse Risk before measures:  Risiko after measures: 
Ytre miljø Risk before measures:  Risiko after measures: 

Incident: Exposure to Sodium nitroprusside

Consequence area: Helse Risk before measures:  Risiko after measures: 

Incident: Exposure to NH₄Cl

Consequence area: Helse Risk before measures:  Risiko after measures: 


**Hazard: Detection of ammonium ions using indophenol blue method****Incident: Exposure to Ethanol**

Consequence area:	Helse	Risk before measures:	 Risiko after measures:	
	Materielle verdier	Risk before measures:	 Risiko after measures:	

Incident: Exposure to UV form the UV-Vis spectrophotometer

Consequence area:	Helse	Risk before measures:	 Risiko after measures:	
--------------------------	-------	-----------------------	--	---

Incident: Exposure to Sodium hypochloride

Consequence area:	Helse	Risk before measures:	 Risiko after measures:	
	Materielle verdier	Risk before measures:	 Risiko after measures:	

Hazard: Catalyst characterization**Incident: High voltages SEM, EDX and EPR**

Consequence area:	Helse	Risk before measures:	 Risiko after measures:	
--------------------------	-------	-----------------------	--	---

Incident: X-ray radiation (XRD)

Consequence area:	Helse	Risk before measures:	 Risiko after measures:	
--------------------------	-------	-----------------------	--	---

Incident: Exposure to powder and nanoparticles from sample preparation for SEM, EDX, EPR and XRD

Consequence area:	Helse	Risk before measures:	 Risiko after measures:	
--------------------------	-------	-----------------------	--	---

Incident: Exposure to UV form the UV-Vis DRS spectrophotometer

Consequence area:	Helse	Risk before measures:	 Risiko after measures:	
--------------------------	-------	-----------------------	--	---



Hazard: Catalyst characterization

Incident: Exposure to strong magnetic fields from EPR

Consequence area: Helse
Risk before measures:  Risiko after measures: 

Hazard: Alkali etching of LDH

Incident: Exposure to Sodium Hydroxide

Consequence area: Helse
Materielle verdier
Risk before measures:  Risiko after measures: 
Risk before measures:  Risiko after measures: 

Final evaluation

Organizational units and people involved

A risk assessment may apply to one or more organizational units, and involve several people. These are listed below.

Organizational units which this risk assessment applies to

- Institutt for kjemisk prosesssteknologi

Participants

Jibin Antony

Magnus Rønning

Estelle Marie M. Vanhaecke

Anne Hoff

Karin Wiggen Dragsten

Gunn Torill Wikdahl

Readers

Jens Norrman

Isabel Maria Pascual Garcia

Gøril Flatberg

Karthikai Selvan Sivasamy

Others involved/stakeholders

[Ingen registreringer]

The following accept criteria have been decided for the risk area Risikovurdering: Helse, miljø og sikkerhet (HMS):

Helse



Materielle verdier



Omdømme



Ytre miljø



Overview of existing relevant measures which have been taken into account

The table below presents existing measures which have been taken into account when assessing the likelihood and consequence of relevant incidents.

Hazard	Incident	Measures taken into account
Preparation of CuCr-LDH, CuCrFe-LDH, CoCuCr-LDH and CuNiCr-LDH in lab K5-317	Exposure to Copper(II) nitrate hydrate	Use of Personal Protective Equipment
	Exposure to Copper(II) nitrate hydrate	Safety Data Sheet
	Exposure to Copper(II) nitrate hydrate	Use fume hood
	Exposure to Sodium Hydroxide	Use of Personal Protective Equipment
	Exposure to Sodium Hydroxide	Safety Data Sheet
	Exposure to Sodium Hydroxide	Use fume hood
	Exposure to Chromium(III) nitrate nonahydrate	Use of Personal Protective Equipment
	Exposure to Chromium(III) nitrate nonahydrate	Safety Data Sheet
	Exposure to Chromium(III) nitrate nonahydrate	Use fume hood
	Exposure to Iron (III) nitrate nonahydrate	Use of Personal Protective Equipment
	Exposure to Iron (III) nitrate nonahydrate	Safety Data Sheet
	Exposure to Iron (III) nitrate nonahydrate	Use fume hood
	Exposure to Cobalt (II) nitrate hydrate	Use of Personal Protective Equipment
	Exposure to Cobalt (II) nitrate hydrate	Safety Data Sheet
Exposure to Cobalt (II) nitrate hydrate	Use fume hood	
Working with Solar Simulator (ScienceTech SF-300-A)	Exposure to UV rays from the solar simulator	Use of Personal Protective Equipment
	Exposure to UV rays from the solar simulator	Apparatus Card
	Burns caused by touching the arc lamp envelope	Use of Personal Protective Equipment
	Burns caused by touching the arc lamp envelope	Apparatus Card
Working in the lab during COVID pandemic	Risk due to touching the face while at work	
	Risk due to close contact of colleagues	
	Risk due to touching common objects	
	Risk of getting infected by the public	
Use of heating oven (K5-317)	Accidentally touching a hot surface on the furnace may cause burns	
Waste disposal in general for the laboratories in K5	Incorrect waste handling	
	Disposal of Hg containing wastes	



Detection of ammonium ions using indophenol blue method	Exposure to phenol	Use of Personal Protective Equipment
	Exposure to phenol	Safety Data Sheet
	Exposure to phenol	Use fume hood
	Exposure to Sodium nitroprusside	Safety Data Sheet
	Exposure to NH ₄ Cl	Use of Personal Protective Equipment
	Exposure to NH ₄ Cl	Safety Data Sheet
	Exposure to NH ₄ Cl	Use fume hood
	Exposure to Ethanol	Use of Personal Protective Equipment
	Exposure to Ethanol	Safety Data Sheet
	Exposure to Ethanol	Use fume hood
	Exposure to UV form the UV-Vis spectrophotometer	Use of Personal Protective Equipment
	Exposure to UV form the UV-Vis spectrophotometer	Apparatus Card
	Exposure to Sodium hypochloride	Use of Personal Protective Equipment
	Exposure to Sodium hypochloride	Safety Data Sheet
	Exposure to Sodium hypochloride	Use fume hood
Catalyst characterization	High voltages SEM, EDX and EPR	Use of Personal Protective Equipment
	High voltages SEM, EDX and EPR	Safety Data Sheet
	High voltages SEM, EDX and EPR	Apparatus Card
	X-ray radiation (XRD)	
	Exposure to powder and nanoparticles from sample preparation for SEM, EDX, EPR and XRD	Use of Personal Protective Equipment
	Exposure to powder and nanoparticles from sample preparation for SEM, EDX, EPR and XRD	Use fume hood
	Exposure to UV form the UV-Vis DRS spectrophotometer	Use of Personal Protective Equipment
	Exposure to UV form the UV-Vis DRS spectrophotometer	Apparatus Card
	Exposure to strong magnetic fields from EPR	Use of Personal Protective Equipment
	Exposure to strong magnetic fields from EPR	Apparatus Card
Alkali etching of LDH	Exposure to Sodium Hydroxide	Use of Personal Protective Equipment
	Exposure to Sodium Hydroxide	Safety Data Sheet
	Exposure to Sodium Hydroxide	Use fume hood

Existing relevant measures with descriptions:**Use of Personal Protective Equipment**

All work will be performed by using personal protective equipments such as labcoat, gloves and glasses at all time. Powders will be handled in fume hoods and filter masks will be used.

Safety Data Sheet

Refer to safety data sheets of the chemicals before handling them. A copy of SDS to be kept in the lab.



Apparatus Card

Has the information about the equipment.
Read before using.

Use of ear plugs

Use ear plugs when using noisy instruments like ultrasonication bath.

Use fume hood

Synthesis of the catalyst would be done in fume hoods.

Instrument training

Proper training on instruments by the instrument owner so that it is used in a safe manner.

Risk analysis with evaluation of likelihood and consequence

This part of the report presents detailed documentation of hazards, incidents and causes which have been evaluated. A summary of hazards and associated incidents is listed at the beginning.

The following hazards and incidents has been evaluated in this risk assessment:

- **Preparation of CuCr-LDH, CuCrFe-LDH, CoCuCr-LDH and CuNiCr-LDH in lab K5-317**
 - Exposure to Copper(II) nitrate hydrate
 - Exposure to Sodium Hydroxide
 - Exposure to Chromium(III) nitrate nonahydrate
 - Exposure to Iron (III) nitrate nonahydrate
 - Exposure to Cobalt (II) nitrate hydrate
 - Exposure to Nickel (II) nitrate hydrate
- **Working with Solar Simulator (ScienceTech SF-300-A)**
 - Exposure to UV rays from the solar simulator
 - Burns caused by touching the arc lamp envelope
- **Working in the lab during COVID pandemic**
 - Risk due to touching the face while at work
 - Risk due to close contact of colleagues
 - Risk due to touching common objects
 - Risk of getting infected by the public
- **Use of heating oven (K5-317)**
 - Accidentally touching a hot surface on the furnace may cause burns
- **Waste disposal in general for the laboratories in K5**
 - Incorrect waste handling
 - Disposal of Hg containing wastes
- **Detection of ammonium ions using indophenol blue method**
 - Exposure to phenol
 - Exposure to Sodium nitroprusside
 - Exposure to NH₄Cl
 - Exposure to Ethanol
 - Exposure to UV from the UV-Vis spectrophotometer
 - Exposure to Sodium hypochloride
- **Catalyst characterization**
 - High voltages SEM, EDX and EPR
 - X-ray radiation (XRD)
 - Exposure to powder and nanoparticles from sample preparation for SEM, EDX, EPR and XRD
 - Exposure to UV from the UV-Vis DRS spectrophotometer
 - Exposure to strong magnetic fields from EPR
- **Alkali etching of LDH**
 - Exposure to Sodium Hydroxide

Detailed view of hazards and incidents:

Hazard: Preparation of CuCr-LDH, CuCrFe-LDH, CoCuCr-LDH and CuNiCr-LDH in lab K5-317**Incident: Exposure to Copper(II) nitrate hydrate**

Likelihood of the incident (common to all consequence areas): **Unlikely (1)**

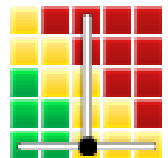
Kommentar:

P210 Keep away from heat, hot surfaces, sparks, open flames and other ignition sources. No smoking.
P273 Avoid release to the environment.
P280 Wear protective gloves.

Consequence area: Helse

Assessed consequence: **Large (3)**

Comment: H302 Harmful if swallowed.
H315 Causes skin irritation.
H318 Causes serious eye damage.

Risk:**Consequence area: Ytre miljø**

Assessed consequence: **Large (3)**

Comment: H410 Very toxic to aquatic life with long lasting effects.
H272 May intensify fire; oxidizer.

Risk:**Consequence area: Materielle verdier**

Assessed consequence: **Large (3)**

Comment: H272 May intensify fire; oxidizer.

Risk:

Incident: Exposure to Sodium Hydroxide

Likelihood of the incident (common to all consequence areas): **Unlikely (1)**

Kommentar:

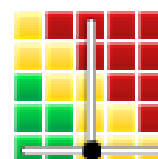
P280 - Wear eye protection, face protection, protective clothing, protective gloves.

Consequence area: Helse

Assessed consequence: **Large (3)**

Comment: H314 Causes severe skin burns and eye damage.
H318 Causes serious eye damage.

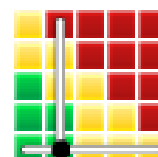
Risk:

**Consequence area: Materielle verdier**

Assessed consequence: **Medium (2)**

Comment: [Ingen registreringer]

Risk:

**Incident: Exposure to Chromium(III) nitrate nonahydrate**

Likelihood of the incident (common to all consequence areas): **Unlikely (1)**

Kommentar:

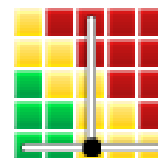
P210 Keep away from heat, hot surfaces, sparks, open flames and other ignition sources. No smoking.
P273 Avoid release to the environment.
P280 - Wear eye protection, face protection, protective clothing, protective gloves.

Consequence area: Helse

Assessed consequence: **Large (3)**

Comment: H315 Causes skin irritation.
H317 May cause an allergic skin reaction.
H319 Causes serious eye irritation.

Risk:



Consequence area: Ytre miljø*Assessed consequence: Large (3)**Comment: H410 Very toxic to aquatic life with long lasting effects.***Risk:****Consequence area: Materielle verdier***Assessed consequence: Medium (2)**Comment: H272 May intensify fire; oxidizer.***Risk:****Incident: Exposure to Iron (III) nitrate nonahydrate**

*Likelihood of the incident (common to all consequence areas): Unlikely (1)**Kommentar:*

Eye/face protection (safety goggles)

Skin protection (Nitrile rubber gloves)

Consequence area: Helse*Assessed consequence: Medium (2)**Comment: Causes severe skin burns and eye damage***Risk:****Consequence area: Materielle verdier***Assessed consequence: Small (1)**Comment: [Ingen registreringer]***Risk:**

Incident: Exposure to Cobalt (II) nitrate hydrate

Likelihood of the incident (common to all consequence areas): **Unlikely (1)**

Kommentar:

P210 Keep away from heat, hot surfaces, sparks, open flames and other ignition sources. No smoking.

P273 Avoid release to the environment.

P280 Wear protective gloves/ protective clothing/ eye protection/ face protection/ hearing protection.

Consequence area: Helse

Assessed consequence: **Very large (4)**

Comment: H302 + H332 Harmful if swallowed or if inhaled.
H317 May cause an allergic skin reaction.
H318 Causes serious eye damage.
H334 May cause allergy or asthma symptoms or breathing difficulties if inhaled.
H341 Suspected of causing genetic defects.
H350 May cause cancer.
H360F May damage fertility.

Risk:**Consequence area: Ytre miljø**

Assessed consequence: **Large (3)**

Comment: H410 Very toxic to aquatic life with long lasting effects.

Risk:**Consequence area: Materielle verdier**

Assessed consequence: **Large (3)**

Comment: H272 May intensify fire; oxidizer.

Risk:

Incident: Exposure to Nickel (II) nitrate hydrate

Likelihood of the incident (common to all consequence areas): **Unlikely (1)**

Kommentar:

P210 Keep away from heat, hot surfaces, sparks, open flames and other ignition sources. No smoking.

P273 Avoid release to the environment.

P280 Wear protective gloves/ protective clothing/ eye protection/ face protection/ hearing protection.

Consequence area: Helse

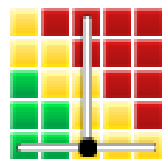
Assessed consequence: **Very large (4)**

Comment: H302 + H332 Harmful if swallowed or if inhaled.
H315 Causes skin irritation.
H317 May cause an allergic skin reaction.
H318 Causes serious eye damage.
H334 May cause allergy or asthma symptoms or breathing difficulties if inhaled.
H341 Suspected of causing genetic defects.
H350 May cause cancer.
H360 May damage fertility or the unborn child.
H372 Causes damage to organs through prolonged or repeated exposure if inhaled.

Risk:**Consequence area: Ytre miljø**

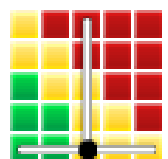
Assessed consequence: **Large (3)**

Comment: H410 Very toxic to aquatic life with long lasting effects.

Risk:**Consequence area: Materielle verdier**

Assessed consequence: **Large (3)**

Comment: H272 May intensify fire; oxidizer.

Risk:

Hazard: Working with Solar Simulator (ScienceTech SF-300-A)

Incident: Exposure to UV rays from the solar simulator

Likelihood of the incident (common to all consequence areas): **Less likely (2)**

Kommentar:

UV protective glasses will be used while working with the instrument. A light-tight photoreactor will be used to prevent UV exposure. Additionally, shields or barriers will be used to enclose the UV source while in operation. The users in the lab will be made aware of the potential hazards with direct exposure. Hazard warning signs will be placed on the instrument to inform about the risk of exposure during use and maintenance.

Consequence area: Helse

Assessed consequence: **Large (3)**

Comment: The acute effect of UVR is redness of the skin (erythema). Chronic effects include accelerated skin aging and skin cancer. UVR is absorbed in the outer layers of the eye – the cornea and conjunctiva. Acute overexposure leads to a painful temporary inflammation, mainly of the cornea (photokeratitis). Chronic exposure might lead to an increased risk of certain types of ocular cataracts.

Risk:**Incident: Burns caused by touching the arc lamp envelope**

Likelihood of the incident (common to all consequence areas): **Unlikely (1)**

Kommentar:

Let the lamp cool at least 15 minutes before opening the lamp compartment door. The manufacturer's manual will be looked for further assistance on safety-related information before using the equipment or during maintenance.

Consequence area: Helse

Assessed consequence: **Medium (2)**

Comment: May cause superficial burns

Risk:

Hazard: Working in the lab during COVID pandemic

Incident: Risk due to touching the face while at work

Likelihood of the incident (common to all consequence areas): **Less likely (2)**

Kommentar:

Will avoid touching face while at work.
Regular washing of hands

Consequence area: Helse

Assessed consequence: **Large (3)**

Comment: [Ingen registreringer]

Risk:**Incident: Risk due to close contact of colleagues**

Likelihood of the incident (common to all consequence areas): **Less likely (2)**

Kommentar:

1 m distance will be maintained at all times. If possible 2 m

Consequence area: Helse

Assessed consequence: **Large (3)**

Comment: [Ingen registreringer]

Risk:

Incident: Risk due to touching common objects

Likelihood of the incident (common to all consequence areas): **Less likely (2)**

Kommentar:

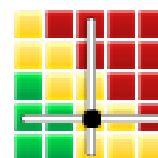
Disinfection before and after with ethanol will be done on all surfaces that I'll be in contact with (door knob – card reader with code panel. This would also apply to laboratory PC screen, keyboard, mouse, desk and the label printing machine.

Consequence area: Helse

Assessed consequence: **Large (3)**

Comment: [Ingen registreringer]

Risk:

**Incident: Risk of getting infected by the public**

Likelihood of the incident (common to all consequence areas): **Less likely (2)**

Kommentar:

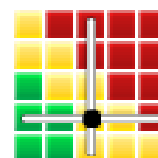
Will avoid usage of public transportation methods

Consequence area: Helse

Assessed consequence: **Large (3)**

Comment: [Ingen registreringer]

Risk:



**Hazard: Use of heating oven (K5-317)**

Incident: Accidentally touching a hot surface on the furnace may cause burns

Likelihood of the incident (common to all consequence areas): **Less likely (2)**

Kommentar:

The autoclave is placed in a closed cabinet, which reduces the likelihood of accidentally touching a hot surface. It has a visible display which displays the temperature in the oven, and heat protective gloves are available. The autoclave will be cooled down to room temperature before handling it.

Consequence area: Helse

Assessed consequence: **Medium (2)**

Comment: Superficial burns

Risk:

Hazard: Waste disposal in general for the laboratories in K5

Incident: Incorrect waste handling

Likelihood of the incident (common to all consequence areas): **Less likely (2)**

Kommentar:

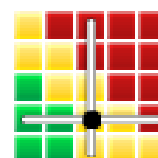
Received HSE course and have proper knowledge on how to dispose of lab waste

Consequence area: Helse

Assessed consequence: **Large (3)**

Comment: Incorrect waste handling would lead to treatability issues of the chemicals after being shipped. This could lead to high risk of contaminated or harmful releases to the environment. Since the dangers associated with NPs are not well known, these need to be considered toxic and hence disposed off in separate container.

Risk:

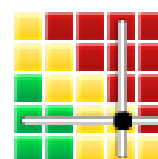


Consequence area: Ytre miljø

Assessed consequence: **Very large (4)**

Comment: Incorrect waste handling would lead to treatability issues of the chemicals after being shipped. This could lead to high risk of contaminated or harmful releases to the environment. Since the dangers associated with NPs are not well known, these need to be considered toxic and hence disposed off in separate container.

Risk:

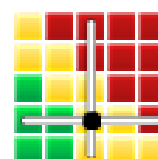


Consequence area: Materielle verdier

Assessed consequence: **Large (3)**

Comment: Incorrect waste handling would lead to treatability issues of the chemicals after being shipped. This could lead to high risk of contaminated or harmful releases to the environment. Since the dangers associated with NPs are not well known, these need to be considered toxic and hence disposed off in separate container.

Risk:



**Incident: Disposal of Hg containing wastes**

Likelihood of the incident (common to all consequence areas): **Less likely (2)**

Kommentar:

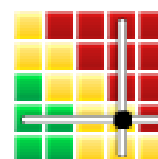
[Ingen registreringer]

Consequence area: Helse

Assessed consequence: **Very large (4)**

Comment: Nessler's reagent could be fatal if swallowed or in contact with skin
Causes severe skin burns and eye damage.
Toxic if inhaled
May cause damage to organs through prolonged or repeated exposure.

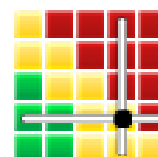
Risk:

**Consequence area: Ytre miljø**

Assessed consequence: **Very large (4)**

Comment: Very toxic to aquatic life with long lasting effects.

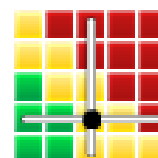
Risk:

**Consequence area: Materielle verdier**

Assessed consequence: **Large (3)**

Comment: May be corrosive to metals

Risk:



Hazard: Detection of ammonium ions using indophenol blue method

Incident: Exposure to phenol

Likelihood of the incident (common to all consequence areas): **Unlikely (1)**

Kommentar:

P260 Do not breathe dust/ fume/ gas/ mist/ vapors/ spray.

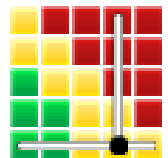
P273 Avoid release to the environment.

P280 Wear protective gloves/ protective clothing/ eye protection/ face protection/ hearing protection.

Consequence area: Helse

Assessed consequence: **Very large (4)**

Comment: H301 + H311 + H331 Toxic if swallowed, in contact with skin or if inhaled.
H314 Causes severe skin burns and eye damage.
H341 Suspected of causing genetic defects.
H373 May cause damage to organs (Nervous system, Kidney, Liver, Skin) through prolonged or repeated exposure.

Risk:**Consequence area: Ytre miljø**

Assessed consequence: **Large (3)**

Comment: H411 Toxic to aquatic life with long lasting effects.

Risk:**Incident: Exposure to Sodium nitroprusside**

Likelihood of the incident (common to all consequence areas): **Unlikely (1)**

Kommentar:

[Ingen registreringer]

Consequence area: Helse

Assessed consequence: **Large (3)**

Comment: H301 Toxic if swallowed.

Risk:

Incident: Exposure to NH4Cl

Likelihood of the incident (common to all consequence areas): **Less likely (2)**

Kommentar:

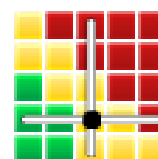
Will avoid release to the environment and dispose the waste in proper waste containers. Wear protective gloves and eye protection.

Consequence area: Helse

Assessed consequence: **Large (3)**

Comment: Harmful if swallowed. Causes serious eye irritation.

Risk:

**Incident: Exposure to Ethanol**

Likelihood of the incident (common to all consequence areas): **Unlikely (1)**

Kommentar:

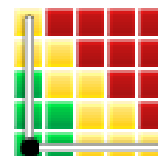
Potential ignition sources are isolated in the lab, little exposure to ignition sources. Using fume hoods remove flammable vapors. Gloves, lab coat and safety goggles are always used.

Consequence area: Helse

Assessed consequence: **Small (1)**

Comment: May cause eye irritation

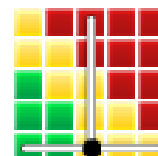
Risk:

**Consequence area: Materielle verdier**

Assessed consequence: **Large (3)**

Comment: Highly flammable liquid and vapour

Risk:



Incident: Exposure to UV form the UV-Vis spectrophotometer

Cause: Unsafe use

Likelihood of the incident (common to all consequence areas): **Unlikely (1)**

Kommentar:

[Ingen registreringer]

Consequence area: Helse

Assessed consequence: **Large (3)**

Comment: The acute effect of UVR is redness of the skin (erythema). Chronic effects include accelerated skin aging and skin cancer. UVR is absorbed in the outer layers of the eye – the cornea and conjunctiva. Acute overexposure leads to a painful temporary inflammation, mainly of the cornea (photokeratitis). Chronic exposure might lead to an increased risk of certain types of ocular cataracts.

Risk:

**Incident: Exposure to Sodium hypochloride**

Likelihood of the incident (common to all consequence areas): **Unlikely (1)**

Kommentar:

P280 Wear protective gloves/ protective clothing/ eye protection/ face protection/ hearing protection.

Consequence area: Helse

Assessed consequence: **Large (3)**

Comment: H314 Causes severe skin burns and eye damage.

Risk:

**Consequence area: Materielle verdier**

Assessed consequence: **Medium (2)**

Comment: H290 May be corrosive to metals.

Risk:



Hazard: Catalyst characterization

Incident: High voltages SEM, EDX and EPR

Likelihood of the incident (common to all consequence areas): **Unlikely (1)**

Kommentar:

[Ingen registreringer]

Consequence area: Helse

Assessed consequence: **Very large (4)**

Comment: [Ingen registreringer]

Risk:



Incident: X-ray radiation (XRD)

Likelihood of the incident (common to all consequence areas): **Unlikely (1)**

Kommentar:

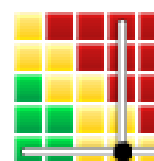
[Ingen registreringer]

Consequence area: Helse

Assessed consequence: **Very large (4)**

Comment: [Ingen registreringer]

Risk:



Incident: Exposure to powder and nanoparticles from sample preparation for SEM, EDX, EPR and XRD

Likelihood of the incident (common to all consequence areas): **Less likely (2)**

Kommentar:

[Ingen registreringer]

Consequence area: Helse

Assessed consequence: **Large (3)**

Comment: [Ingen registreringer]

Risk:

**Incident: Exposure to UV form the UV-Vis DRS spectrophotometer**

Likelihood of the incident (common to all consequence areas): **Unlikely (1)**

Kommentar:

[Ingen registreringer]

Consequence area: Helse

Assessed consequence: **Large (3)**

Comment: The acute effect of UVR is redness of the skin (erythema). Chronic effects include accelerated skin aging and skin cancer. UVR is absorbed in the outer layers of the eye – the cornea and conjunctiva. Acute overexposure leads to a painful temporary inflammation, mainly of the cornea (photokeratitis). Chronic exposure might lead to an increased risk of certain types of ocular cataracts.

Risk:





Incident: Exposure to strong magnetic fields from EPR

Likelihood of the incident (common to all consequence areas): **Unlikely (1)**

Kommentar:

[Ingen registreringer]

Consequence area: Helse

Assessed consequence: **Medium (2)**

Comment: [Ingen registreringer]

Risk:



**Hazard: Alkali etching of LDH**

Incident: Exposure to Sodium Hydroxide

Likelihood of the incident (common to all consequence areas): **Unlikely (1)**

Kommentar:

P280 - Wear eye protection, face protection, protective clothing, protective gloves.

Consequence area: Helse

Assessed consequence: **Large (3)**

Comment: H314 Causes severe skin burns and eye damage.
H318 Causes serious eye damage.

Risk:

**Consequence area: Materielle verdier**

Assessed consequence: **Medium (2)**

Comment: [Ingen registreringer]

Risk:





Overview of risk mitigating measures which have been decided:

Below is an overview of risk mitigating measures, which are intended to contribute towards minimizing the likelihood and/or consequence of incidents:

Overview of risk mitigating measures which have been decided, with description:



Detailed view of assessed risk for each hazard/incident before and after mitigating measures

